AD-A230 964

DOCUMENTATION PAGE

Form Approved
OMB No. 0704-0188

1a. REPORT SECURITY CLASSIFICATION Unclassified	1b. RESTRICTIVE MARKINGS

DTIC
SELECTE
JAN 1 5 1991
S B D

DTIC FILE COPY

2a. SECURITY CLASSIFICATION AUTHORITY	3. DISTRIBUTION / AVAILABILITY OF REPORT
2b. DECLASSIFICATION / DOWNGRADING SCHEDULE	Approved for public release; distribution unlimited

4. PERFORMING ORGANIZATION REPORT NUMBER(S)	5. MONITORING ORGANIZATION REPORT NUMBER(S) ARO 25391.57-PH

6a. NAME OF PERFORMING ORGANIZATION Optical Sciences Center	6b. OFFICE SYMBOL *(If applicable)*	7a. NAME OF MONITORING ORGANIZATION ONRRR

6c. ADDRESS *(City, State, and ZIP Code)* University of Arizona Tucson, Arizona 85721	7b. ADDRESS *(City, State, and ZIP Code)* University of New Mexico Bandelier Hall West Albuquerque, NM 87131

8a. NAME OF FUNDING / SPONSORING ORGANIZATION JSOP (ARO)	8b. OFFICE SYMBOL *(If applicable)*	9. PROCUREMENT INSTRUMENT IDENTIFICATION NUMBER ARO MIP 111-90

8c. ADDRESS *(City, State, and ZIP Code)* Director, Physics Division U.S. Army Research Office Research Triangle Park, NC 27709-2211	10. SOURCE OF FUNDING NUMBERS			
	PROGRAM ELEMENT NO.	PROJECT NO.	TASK NO	WORK UNIT ACCESSION NO.

11. TITLE *(Include Security Classification)*

Research in Optical Sciences

12. PERSONAL AUTHOR(S)
R. R. Shannon

13a. TYPE OF REPORT Final	13b. TIME COVERED FROM 3/11/88 TO 3/10/91	14. DATE OF REPORT *(Year, Month, Day)* 90,12,3	15. PAGE COUNT 117

16. SUPPLEMENTARY NOTATION

17. COSATI CODES			18. SUBJECT TERMS *(Continue on reverse if necessary and identify by block number)*
FIELD	GROUP	SUB-GROUP	Optical Sciences

19. ABSTRACT *(Continue on reverse if necessary and identify by block number)*

This report discusses research progress in the Optical Sciences, including the areas of: scanning tunneling microscopy in the evaluation of HgCdTe material, optical elements for x-ray and uv wavelengths; interaction of a single semiconductor cluster with intense laser beams; coherent and nonlinear effects in semiconductors; nonlinear organics for guided wave devices; nonlinear propagation and wave mixing in sodium vapor; gain/feedback approach to optical instabilities; conical emission; kaleidoscopic spatial instability; nonlinear dynamics and chaos in cavity QED; origin and application of four-wave mixing in semiconductors; theory of the semiconductor laser; nonlinear theory of phase conjugate optics; polishing of diamond films with argon and oxygen ion beams; and chemical vapor deposition of diamond and diamond-like films.

20. DISTRIBUTION / AVAILABILITY OF ABSTRACT ☐ UNCLASSIFIED/UNLIMITED ☐ SAME AS RPT. ☐ DTIC USERS	21. ABSTRACT SECURITY CLASSIFICATION
22a. NAME OF RESPONSIBLE INDIVIDUAL	22b. TELEPHONE *(Include Area Code)*	22c. OFFICE SYMBOL

DD Form 1473, JUN 86 *Previous editions are obsolete.* SECURITY CLASSIFICATION OF THIS PAGE

91 1 14 097

TABLE OF CONTENTS

By_____
Distribution/
Availability Codes

Dist	Avail and/or Special
A-1	

SCANNING TUNNELING MICROSCOPY IN THE EVALUATION OF HgCdTe MATERIAL

E. L. Dereniak, J. D. He and M. A. Voelker

SCIENTIFIC PERSONNEL

E. L. Dereniak
M. A. Voelker
J. D. He
K. Kuhler

OBJECTIVES

The primary goal of this project is to examine the surface characteristics of mercury cadmium telluride (HgCdTe) infrared detectors, through scanning tunneling microscopy, to determine the source of performance-limiting dark current in those detectors. The STM is used as a point-contact probe to measure the resistance of various paths across the surface of the sample devices. Measured resistance values are then correlated with the performance of the detectors. A unique vacuum-compatible, dual-tip STM is to be built that will allow examination of the detector chips at their operating temperature of 77 K. Measurements of the resistnace between the two tips 'll be taken using one of the tips as a signal source and the other tip as a listening piuoe that can be scanned across the surface of the semiconductor chip. The strength of the detected signal, as measured with a lock-in amplifier, will indicate the resistance value associated with a given pair of tip positions. Because STM produces images of the surface under investigation, this process will result in the mapping of low-resistance pathways across the surface of the sample's p-n junction, if such pathways exist. Surface currents across the p-n junction are thought to cause high dark-current levels in HgCdTe photovoltaic detectors.

In addition, development of this dual-tip technique will allow the noncontact measurement of detector resistance, an important measure of detector quality. This should allow the evaluation of an array of detector elements before the array is irreversibly bonded to an expensive CCD readout chip, resulting in higher hybrid device yield (no bad detector arrays will be bonded to good CCDs) and a lower unit cost for the complete array.

Finally, the dual-tip STM developed under this contract should make possible crucial experiments in the infant field of molecular electronics. Largely conceptual to

date, molecular electronics is the construction of electronic circuits using elements (e.g., wires and transistors) consisting of individual molecules--the ultimate in electronic miniaturization. Chemists have synthesized molecules that may act as carriers of electric current (wires), switches (logic gates), optical antennas, and other analogs to today's micron-scale electronic devices. Testing these ideas by investigating the electronic properties of individual molecules will require the use of an "oscilloscope" with nanometer-scale probes that can find and gently touch an individual molecule. The dual-tip STM is such an instrument.

RESEARCH FINDINGS

Because the experimental equipment has not been completed, no data has yet been taken. This portion of the report describes the status of the instrument.

The dual-tip STM consists of four parts: the vacuum chamber, STM scan head (which sits inside the vacuum chamber), STM electronics, a computer, and control software. All elements of this system except the scan head are complete; to complete the instrument, the scan head must be completed, and the integrated system debugged.

The vacuum chamber is a reconditioned system originally used for thin-film deposition. The original bell jar has been removed and replaced with a custom-built cryogenically cooled experiment chamber which holds the STM scan head. This chamber has been successfully pumped to 0.1 microtorr while cooled with liquid nitrogen.

The STM electronics consist of a digital scan-drive section and two analog tip-control sections, one for each tip. Each tip is positioned over the sample surface by means of an analog servo loop in the standard STM fashion. Signals to scan the tips over the surface are generated in the digital drive section, which also produces the TTL signals controlling the collection of the slow-scan video data. In addition, an external lock-in amplifier is included to generate and detect the signal to be injected into the sample. This signal is injected into the sample at tip number one by modulating either that tip's bias voltage or its current setpoint. The injected signal is picked up as current signal at tip two. After filtering and amplification by the lock-in amplifier, the signal is amplitude-multiplexed with the standard STM signal from tip two, and displayed as an overlay on the image produced by that tip. This circuitry is complete and awaits testing and calibration once the scan head is complete.

The computer is an 80286-based IBM-AT clone with auxiliary slow-scan video frame grabber and data input/output boards. These boards communicate with the STM

electronics, controlling the operation of the digital scan drive circuitry, grabbing the data produced, and converting it into standard NTSC video format for display on a dedicated color monitor and for storage on videotape. The computer and software are complete and tested.

The dual-tip scan head is the only unfinished portion of the instrument. It consists of two STM tips and their associated preamps, each mounted on the end of a shaft which can be positioned with nanometer precision by a set of piezoelectric "inchworm" motors. The entire unit is constructed of the vacuum-compatible material Macor machinable glass-ceramic to reduce thermal expansion effects to a minimum. Problems with the customized inchworm motors have resulted in delays, but those problems are not insurmountable. Once they are solved the scan head will be installed in the vacuum chamber and the completed instrument will be debugged and calibrated.

PLANS

After the instrument is complete, experiments will commence, initially on the standard STM substrates graphite and gold. The aim of these experiments will be to demonstrate the feasibility of injecting a signal into a conducting sample and detecting it with another STM tip. This will be accomplished in three steps. First, it will be shown that a single sample can be imaged simultaneously with two independently biased and positioned tips. Next, while both tips are producing images of the surface, one tip will be moved laterally until it encounters the other tip. The effects resulting from the encounter will be noted. Finally, with the two tips brought close to each other in this manner, one tip's bias voltage or current will be modulated, and the other tip will be monitored with the lock-in to see if this injected signal can be detected. The amplitude of the detected signal will be monitored and displayed as an overlay on the image produced by the second tip. A series of these images will be taken as the two tips are moved apart, and as the DC bias voltage of the injection tip is varied. After exploring the surface of gold and graphite in this manner, and after learning how the signal between the two tips varies with changes in such parameters as tip separation, bias voltage and scan rate, and signal frequency and amplitude, these procedures will be repeated for HgCdTe, first at room temperature and then at 77 K.

Finally, this approach will be used to investigate samples of conducting polymer molecules deposited on either gold or graphite. Our aim is to position both tips over a single molecule and determine whether or not an electric current can be passed down

one molecule and detected. Conduction down a molecule will be distinguished from conduction through the substrate by injecting current into molecular quantum states that have energies different from the energies of the surface states of the substrate. That is, it is expected that a molecule lying on the surface of the gold or graphite substrate will display imageable quantum states of the bare substrate. The electronic population of these states will be modulated by the injected signal, and the other tip will search for electrons. As in a bulk conductor, because the conduction and valence states of a conducting molecule are delocalized over the entire length of the molecule, it may be possible to access the same quantum state simultaneously with both STM tips even though the tips are separated spatially by 100 nm or more. Ability to add and to remove electrons simultaneously with two sources (STM tips) from a single spatially extended quantum state (or group of states) is a fascinating and important step in the development of molecular electronic devices.

Success in performing these molecular experiments will depend on the use of STM tips with the smallest possible tip radii, so that the two tips can be brought as close together as possible while both are touching the surface. Tips are available with radii as small as 50 nm, which is less than half the length of polymer molecules already imaged by others using single-tip STMs. Careful attention to tip geometry will be important in these experiments. It will be helpful to image prospective tips before use with a scanning electron microscope, so that only the sharpest available tips can be used. Sample preparation will also be important, so that individual molecules can be isolated on the substrate surface. Previous work by others has shown that samples consisting of individual molecules lying on the surface of the gold or graphite substrate, can be prepared, and imageable with STM.

OPTICAL ELEMENTS FOR X-RAY AND UV WAVELENGTHS

C. M. Falco and J. M. Slaughter

PUBLICATIONS

P. Kearney, J.M. Slaughter, K.D. Powers, and C.M. Falco, "Soft x-ray multilayers produced by sputtering and molecular beam epitaxy (MBE): substrate and interfacial roughness," X-Ray Multilayers for Diffractometers, Monochromators, and Spectrometers, Finn E. Christensen, Editor, Proc. SPIE 984, 188-193 (1988).

Z. Milanovic, M.A. Voelker, M.F. Kelley, K.D. Powers, and C.M. Falco, "Surface roughness healing of substrates for XUV multilayer coatings," X-Ray Multilayers for Diffractometers, Monochromators, and Spectrometers, Finn E. Christensen, Editor, Proc. SPIE 984, 194-201 (1988).

D.W. Schulze, J.M. Slaughter, and C.M. Falco, "Molecular beam epitaxy (MBE) for multilayer fabrication," X-Ray Multilayers for Diffractometers, Monochromators, and Spectrometers, Finn E. Christensen, Editor, Proc. SPIE 984, 75-81 (1988).

F. E. Fernandez, C. Riedel, A. Smith, B. Edwards, B. Lai, F. Cerrina, M.G. Lagally, M.J. Carr, A.D. Romig, Jr., J. Corno, L. Nevot, B. Pardo, J.M. Slaughter, and Charles M. Falco, "Monolithic Fabry-Perot structure for soft x-rays," X-Ray Multilayers for Diffractometers, Monochromators, and Spectrometers, Finn E. Christensen, Editor, Proc. SPIE 984, 256-262 (1988).

A. Smith, C. Riedel, B. Edwards, D. Savage, B. Lai, A. Ray-Chaudhuri, F. Cerrina, M. Lagally, J. Underwood, and C. Falco, "A monochromator based on W/C multilayers of 40 Å layer spacing," X-Ray Multilayers for Diffractometers, Monochromators, and Spectrometers, Finn E. Christensen, Editor, Proc. SPIE 984, 31-38 (1988).

C.M. Falco, F. E. Fernandez, and J.M. Slaughter, "Multilayer optics for soft x-rays" Proceedings of the Materials Research Society, Tokyo, Japan, May 30 - June 3, 1988.

J.M. Slaughter, M.K. Burkland, P.A. Kearney, A.R. Lampis, Z. Milanovic, D.W. Schulze, J.R. Roberts, J. Kerner, E.B. Saloman, and C.M. Falco, "Multilayer mirrors for 182 Å," X-Ray/EUV Optics for Astronomy and Microscopy, Richard B. Hoover, Editor, Proc. SPIE 1160, 235-244 (1989).

J.M. Slaughter, P.A. Kearney, D.W. Schulze, C.M. Falco, C.R. Hills, E.B. Saloman, and R.N. Watts, "Interfaces in Mo/Si multilayers," X-Ray/EUV Optics for Astronomy, Microscopy Polarimetry, and Projection Lithography, Proc. SPIE 1343, International Technical Symposium on Optical & Optoelectronic Applied Science & Engineering, July 8-13, 1990.

P.A. Kearney, J.M. Slaughter, and C.M. Falco, "Selection, growth, and characterization of materials for MBE-produced x-ray optics," X-Ray/EUV Optics for Astronomy, Microscopy Polarimetry, and Projection Lithography, Proc. SPIE 1343, International Technical Symposium on Optical & Optoelectronic Applied Science & Engineering, July 8-13, 1990.

J.M. Slaughter, B.N. Engel, M.H. Wiedmann, P.A. Kearney, and C.M. Falco, "MBE growth of metal-semiconductor interfaces," Proc. of the NATO Advanced Study Institute on the Science and Technology of Nanostructured Magnetic Materials, Crete, Greece, June 25- July 7,
1990.

Abstracts

J.M. Slaughter, B.N. Engel, P.A. Kearney, D.W. Schulze, A. Shapiro, and C.M. Falco, "MBE growth of Mo and $MoSi_2$ on Si," March Meeting of the American Physical Society, St. Louis, MO, March 20-24, 1989.

A. Shapiro, P.A. Kearney, D.W. Schulze, J. M. Slaughter, and C.M. Falco, "Growth mode of MBE-deposited Mo on Si," March Meeting of the American Physical Society, St. Louis, MO, March 20-24, 1989.

C.M. Falco, J. Slaughter, B. Engel, and A. Shapiro, "Considerations for MBE deposition/analysis of metals and silicon," Joint Meeting of the American, Chinese, and Japanese Vacuum Societies, San Jose, CA, March 6-7, 1989.

Z. Milanovic, D.W. Schulze, J.M. Slaughter, and C.M. Falco, "Sputter deposition and characterization of multilayer mirrors for soft x-rays," The 8th Annual Symposium of the Arizona chapter of The American Vacuum Society, Tucson, Arizona, April 6 & 7, 1989.

P.A. Kearney, G. Herman, J.M. Slaughter and C.M. Falco, "Multilayer x-ray optics for wavelengths below 100 angstroms by MBE: materials selection," The 8th Annual Symposium of the Arizona chapter of The American Vacuum Society, Tucson, Arizona, April 6 & 7, 1989.

M.K. Burkland, J.M. Slaughter, and C.M. Falco, "Ex situ characterization of MBE-grown molybdenum silicide thin films, The 8th Annual Symposium of the Arizona chapter of The American Vacuum Society, Tucson, Arizona, April 6 & 7, 1989.

D.W. Schulze, J.M. Slaughter, and C.M. Falco, "Thickness profiles of thin films deposited by molecular beam epitaxy," The 8th Annual Symposium of the Arizona chapter of The American Vacuum Society, Tucson, Arizona, April 6 & 7, 1989.

A. Shapiro, P.A. Kearney, D.W. Schulze, J.M. Slaughter, and C.M. Falco, "MBE-deposited Mo on Si: nucleation and growth," The 8th Annual Symposium of the Arizona chapter of The American Vacuum Society, Tucson, Arizona, April 6 & 7, 1989

J.M. Slaughter, P.A. Kearney, and Charles M. Falco, "Formation of the Mo-Si interface: Mo on Si(111)(7X7)," Bull. American Physical Society 35, 753 (1990).

RESEARCH FINDINGS

We have produced highly reflective x-ray mirrors using our unique molecular beam epitaxy (MBE) capability as well as by the more conventional sputtering technique. MBE has an advantage in that a large variety of sensitive *in situ* surface analysis techniques can be applied to understand the structure and chemistry of samples, as in the growth studies described below. Two MBE machines are used for our x-ray optics work. A characterization routine involving x-ray diffraction (XRD), Rutherford backscattering (RBS), scanning tunneling microscopy (STM), and soft x-ray reflectivity has been applied to several series of mirrors to determine the effects of various process parameters on interface quality.

We have studied problems related to metal/Si multilayer XUV optics, and have initiated work on new materials. We have concentrated on the Mo/Si system, because it has utility in mirrors for the 130 Å to 250 Å wavelength region. Our MBE machines and associated techniques have been described in previous reports and therefore aren't described in detail here. The study of Mo-Si interfaces in multilayers has been completed, and results are reported in the publication "Interfaces in Mo/Si multilayers." The data analysis of our single-interface growth studies for Mo on Si has been completed. Our computer programs for multilayer mirror design have been upgraded significantly, and two new programs have been written to automatically optimize the structure for maximum reflectance. We have completed an extensive search using optical constants, crystal structure, and metallurgical information to find new element pairs which are suited for MBE growth, as well as having high reflectivity at important soft x-ray wavelengths. Studies of the growth of the most promising materials began during the past six-months. An MBE technique for producing high-quality Pd buffer layers on GaAs(110) has been developed and is described in the publication "MBE growth of metal-semiconductor interfaces," along with a technique for producing thin epitaxial $CoSi_2$/Si bilayers on Si(111).

MBE Fabrication

Growth of Si, $CoSi_2$, and $MoSi_2$

Using *in situ* reflection high-energy electron diffraction (RHEED) and low-energy electron diffraction (LEED) we have studied the deposition of buffer layers of Si onto polished, semiconductor-grade Si wafers. We find a dramatic improvement in the

surface roughness and surface crystal structure with the deposition of as little as 10 Å of Si at a substrate temperature of 800°C. The improvement is particularly noticeable in the RHEED pattern, which shows a decrease in background and an improvement in the spot pattern. The final spot pattern is characteristic of a surface that is absolutely flat except for atomic steps separated by several hundred angstroms. To obtain the most perfect substrate surface possible, the deposition of a 100-Å Si buffer layer at 800°C has become our standard substrate pretreatment for all samples.

CoSi$_2$ has a small lattice mismatch with Si, and has been successfully grown epitaxially on Si by workers interested in the electronic properties of CoSi$_2$-Si heterostructures. We have begun to study this silicide as a potential absorbing material in x-ray mirrors with Si as the spacer layer. The theoretical reflectivity is good for the region below 30 Å, which corresponds to the short wavelength end of the "water window" (the region where water exhibits low absorption of x-rays). Such a mirror requires layer thicknesses on the order of 5 Å, with atomically perfect interfaces throughout a multilayer which may have hundreds of layers. Such requirements are beyond conventional thin-film techniques. These requirements may be met, however, using MBE. We have produced ultrathin layers of epitaxial CoSi$_2$ through a "template method" in which an atomic layer of Co is deposited on a near-room-temperature Si substrate, then heated to form a thin silicide layer called the "template." The template can be thickened at high temperature if necessary. We are now attempting to develop a MBE procedure to fabricate the multilayers.

We have also studied MoSi$_2$ as a possible crystalline absorber for use with Si as a spacer. Films of Mo and MoSi$_2$ have been grown on temperature-controlled Si (111)(7X7) and (100)(2X1) surfaces, and characterized through *in situ* RHEED, LEED, AES, XPS and *ex situ* x-ray diffraction (XRD) and RBS. Shifts in the characteristic XPS lines are observed in the films grown at elevated temperatures, indicating the formation of the silicide. XRD confirms that epitaxial films of MoSi$_2$ are formed. The silicide has been produced by codeposition, and by deposition of a thin layer of Mo onto a substrate held at 500 to 650°C; unfortunately, these films are made rough by island formation. The growth of ultrathin MoSi$_2$ layers by the "template" technique results in smooth epitaxial layers, but they also become rough when thickened.

Although epitaxial MoSi$_2$ films have been grown, we find that the roughness of such films is too great for use in XUV optical elements.

Mo/Si Mirrors

Multilayer mirrors with peak reflectivity near 182 Å at 45° angle of incidence were fabricated and characterized through the techniques mentioned above. The mirror's reflectivities at soft x-ray wavelengths was measured at the SURF-II synchrotron by collaborators at the National Institute of Standards and Technology. The multilayer structure, thus the reflectivity, was very sensitive to the substrate temperature T_s. Mirrors deposited at $T_s = 200°C$ exhibited the highest reflectivity (R = 47%) as well as the most perfect multilayer structure. The reflectivity curve for a mirror deposited at $T_s = 200°C$ mirror is shown in Fig. 1. Mirrors deposited at higher or lower temperatures do not perform as well as those deposited at 200°C.
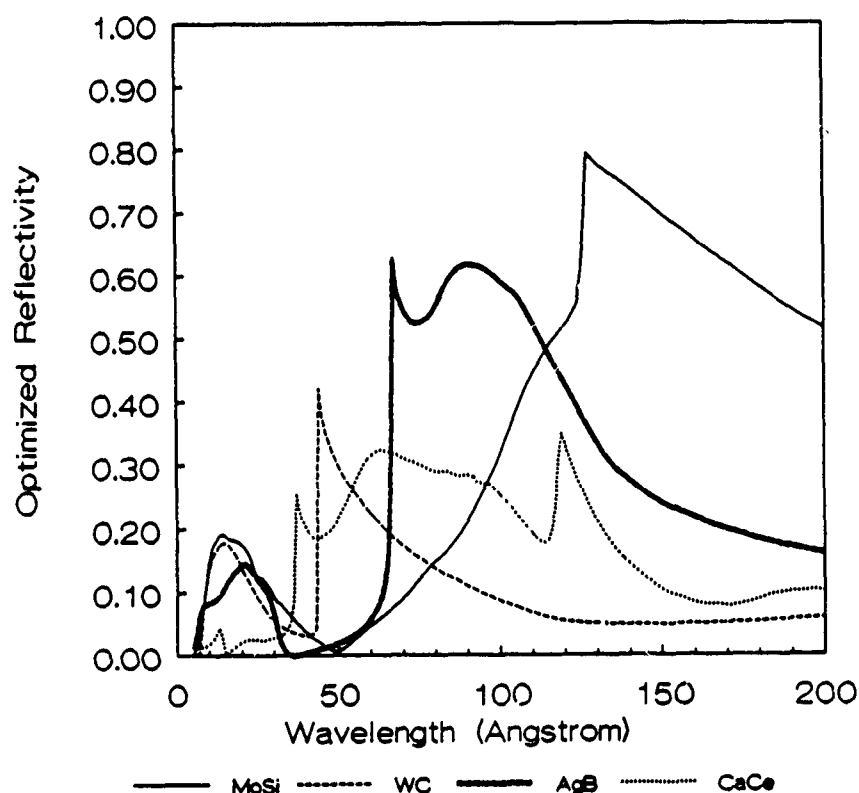

Fig. 1. Reflectivity of an MBE-grown Mo/Si mirror deposited on a 200°C Si substrate. The circles indicate measured data, scaled to 100% S-polarization, and the line is a calculation using σ = 7.5 Å.

TEM micrographs of the multilayers show that a silicide layer forms at the Mo-on-Si interfaces rather than at the Si-on-Mo interfaces. The thickness of the silicide is strongly related to the substrate temperature during deposition. At 300°C the multilayer structure is almost completely destroyed by reaction. The interfacial layers must be

considered when modeling reflectivity data or when designing Mo/Si mirrors. Additional conclusions can be drawn from other characterization techniques. Although heating the substrate during evaporation stimulates the formation of amorphous interfacial silicide layers, it has a positive effect on mirror performance up to 200°C. The benefit may stem from a reduction in the size of the Mo crystallites, which yields to a physically smoother absorber layer. Mirrors with $d_{Mo} \cong 40$ Å performed much better than those with $d_{Mo} \cong 55$ Å Because the XRD shows that the samples with thicker Mo layers have larger Mo crystallites, we infer that these large crystallites lead to higher interface roughness. In addition, the interfacial reaction increases the thickness of the absorber layer, thereby moving the ratio of layer thicknesses away from optimum. These phenomena are important in the design of future mirrors, as they cause the optimum d_{Mo} to be less than that predicted by theoretical calculations. Two of these mirrors have been sent to the Princeton Plasma Physics Laboratory for use in x-ray laser experiments.

The formation of interfacial silicide will degrade the performance of multilayer x-ray mirrors only slightly in the wavelength region for which they are most used, 125 Å to 250 Å The problem is not serious in this region because the interface width is much smaller than the wavelengths of interest. The problem becomes serious, however, if such mirrors are desired for much shorter wavelengths. Even though the theoretical reflectivity of Mo/Si mirrors is reasonably high below 30 Å, formation of the interfacial silicides observed in the present work would make such mirrors useless. A method of inhibiting the reaction, or the use of a different combination of materials, is required for the short-wavelength region.

Selection, Growth, and Characterization of Materials for MBE-Produced X-Ray Optics

MBE is capable of producing a variety of highly pure, epitaxial multilayer materials with well controlled interfaces. However, conditions for MBE growth somewhat restrict the choice of materials. We have initiated a search for new material pairs particularly suited to MBE growth, as well as exhibiting high reflectivity at important soft x-ray wavelengths. Our material-selection procedure considers factors such as chemical reactivity, thermal stability, and lattice match, as well as the maximum theoretical reflectivity. The tightly controlled deposition and the many *in situ* characterization methods of MBE combine to give a great deal of control over the formation of interfaces.

In the 30 Å to 100 Å wavelength region our reflectivity-driven procedure reduces the field of possible choices to 21 elements. When we apply our structurally-driven procedure, the list of viable elemental material pairs becomes even more restricted. Below about 37 Å, few acceptable elemental choices were found. Structural constraints eliminate most of the elements that can achieve adequate performance, without requiring a large number of layers. It may be that compound films, or films with a large number of layers, will be required to produce high-performance periodic multilayer mirrors for wavelengths below 37 Å For wavelengths above 37 Å, the three elemental systems with the most premise for future study are Ca/Ce, Au/B, and Ag/B. The calculated reflectivities of these systems are shown in Fig. 2. In particular, the boron-based systems theoretically can achieve very high reflectivities (>50%) in the 67 Å to 110 Å region. Thus, if superlattices of Ag/B can be produced, the system should outperform both Mo/Si and W/C in the 67 Å to 110 Å wavelength region.
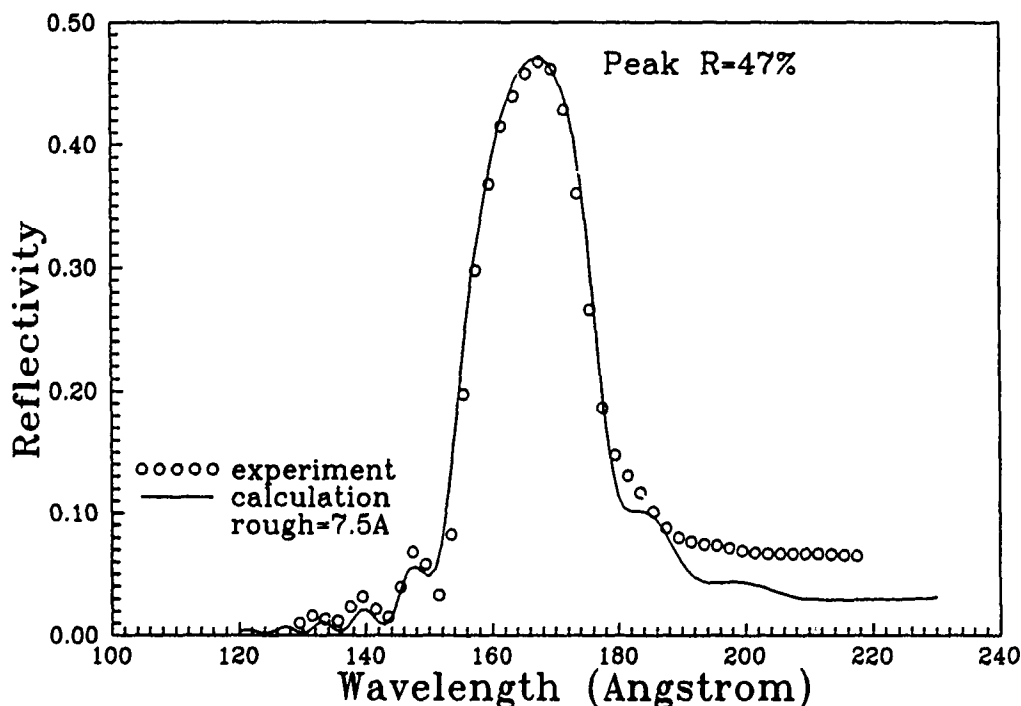

Fig. 2. Optimized 500-layer reflectivity for periodic mirrors made of Mo/Se, Ag/B, W/C, and Ca/Ce. Au/B is similar to Ag/B.

Sputtered Mirrors

During the past three years we have produced a variety of mirrors for use in specific experiments. In every case, the mirrors were designed, fabricated, and characterized in our laboratory, then delivered for use by a collaborator. Many of these projects were described in detail in earlier reports. W/Si cavity mirrors for 206 Å have been used by collaborators at the University of Paris-Sud and Ecole Polytechnique. This wavelength corresponds to a recently discovered aluminum soft x-ray lasing line, which can be pumped with very low power. Mo/Si mirrors for 182 Å were sent to NIST for reflectivity measurements at the SURF-II beamline, and then to Princeton Plasma Physics Laboratory for use in soft x-ray holography experiments by Szymon Suckewer and Charles Skinner. A Mo/Si mirror for 129 Å was sent to Professor Lagally at the Wisconsin synchrotron for use in experiments to study the optical constants near the Si L-edge. A Si/Mo Fabry-Perot mirror has been fabricated and studied at the Wisconsin synchrotron.

INTERACTION OF A SINGLE SEMICONDUCTOR CLUSTER WITH INTENSE LASER BEAMS

D. Sarid, S. Howells and M. Gallagher

SCIENTIFIC PERSONNEL

D. Sarid
S. Howells
M. Gallagher

RESEARCH FINDINGS

During the past period, we have used scanning tunneling microscopy (STM) in conjunction with optical sources to probe the surfaces of quantum confined structures. The system that we have developed can measure the change in conductance of a sample as a function of light incident onto a sample. This allows us to probe local effects that the light has upon these quantum confined structures[1]. We also have the ability to plot the I-V characteristics at any point on the surface as a function of illuminating intensity and wavelength.

The system was developed by reconfiguring a state-of-the-art air scanning tunneling microscope (Nanoscope II) so that it alternately measures the tunneling current first in the presence and then in the absence of light. This is accomplished by using feedback to precisely position the tip above the sample so that a specified tunneling current flows between the biased tip and the sample. The feedback is then suspending momentarily as a diode laser is turned on. With the feedback off and the laser diode switched on, the current is then measured again and the change in tunneling current is calculated. This process is repeated at several kilohertz while the tip is scanned across the sample to obtain a map of the surface displaying the differential conductance, dI/d(intensity).

We have also been using the STM in a more conventional way to probe sizes and shapes of these quantum confined structures. The STM has proven to be an ideal instrument to easily measure the thicknesses of quantum wells as shown below. Figures 1 and 2 are STM images of three InGaAs quantum wells each seven nanometers thick sandwiched between InP barriers. Because we are working under ambient conditions, we must use samples that do not oxidize before the experiments are completed. For this reason, we have been using InGaAs/InP structures. This type of quantum well affords us approximately three hours of imaging before excessive oxidation prevents imaging.
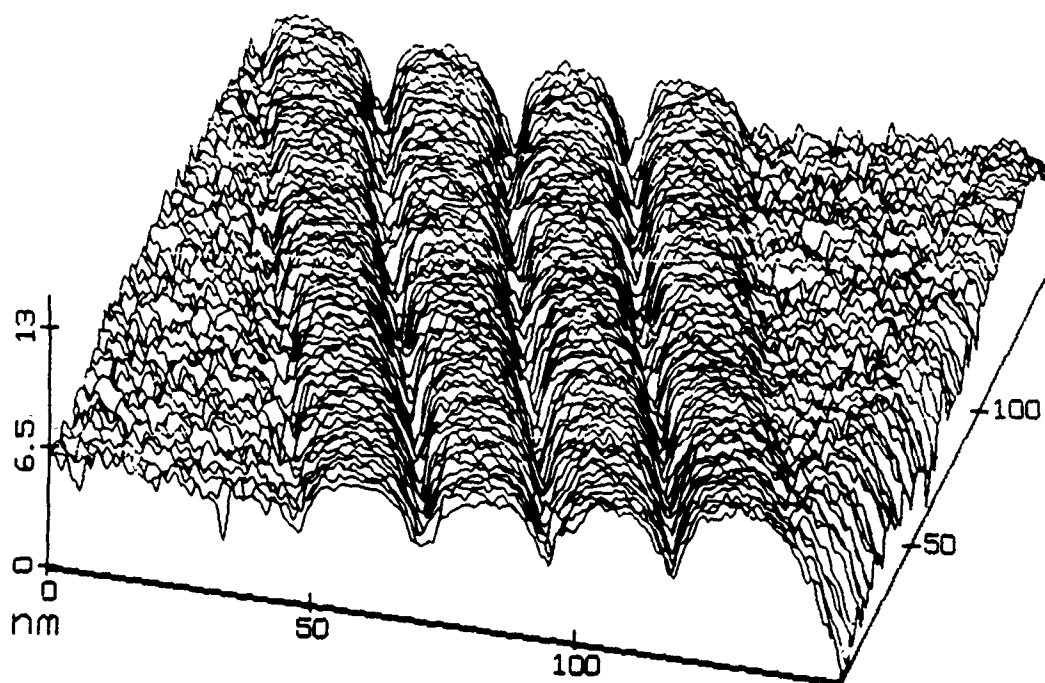
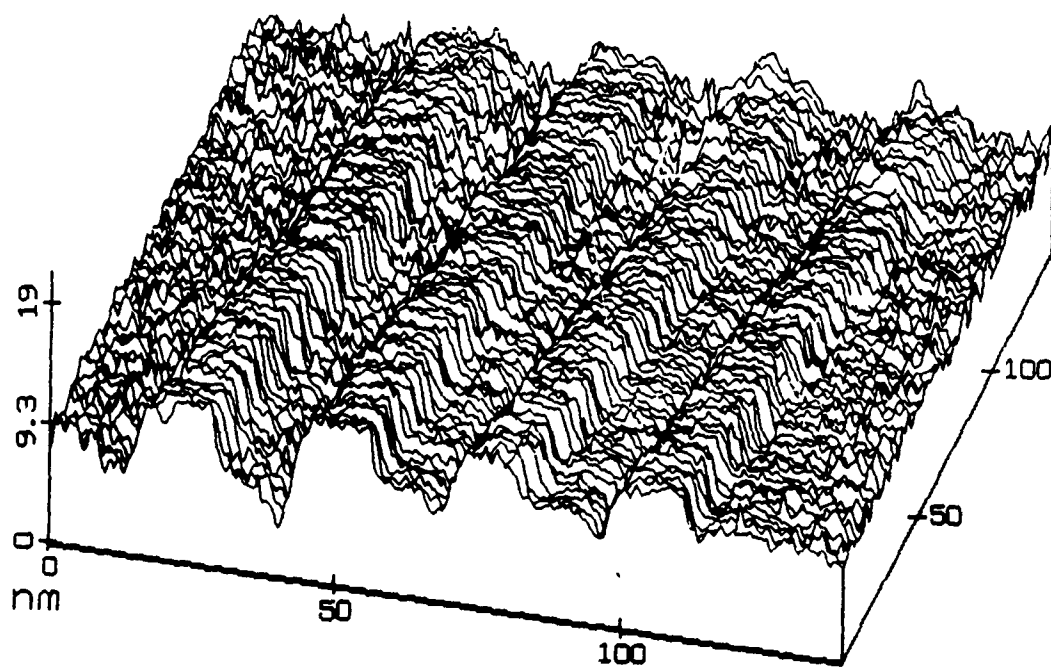*Fig. 1. STM image of three InGaAs quantum wells between InP barriers*

Fig. 2. Another image of the quantum wells, showing a slightly different width. This is most likely attributable to tip effects.

Because of the limitations of operating the STM in air, we have been working on extending the current experiments to UHV. In order to accomplish this, we are using a UHV STM (McAllister Technical Services) and modifying it so that the quantum wells can be easily positioned beneath the tip. By going to UHV, we will be able to image a much wider range of materials, especially GaAs, over extended periods of time.

A second area in which we are proceeding is that of nanostructure characterization of semiconductor clusters. Working in collaboration with H. Gibbs' group, we are using the STM to quantify the size and shape of dry etched quantum dots, as shown in Figs. 3 and 4. The STM has a distinct advantage over standard techniques used to measure quantum dots by being easy to use and by providing height measurements. It also has the flexibility to be able to measure large areas (Fig. 3) as well as individual clusters (Fig. 4). One area in which conventional STM tips are not particularly well suited is the measurement of surfaces with sharp edges. The edge appears rounded, because of the convolution of the tip with the edge. This effect manifests itself by giving the quantum dots the appearance of sloping sides, which is unexpected with the etching technique. In order to reduce this effect, we plan on using tips with much sharper apexes. Using these tips will produce images that more closely reflect the true shape of the quantum dots.

REFERENCES

1. R. H. Hamers and K. Markert, Phys. Rev. Lett. 64(9), 1051 (1990).

2. T. Kato, F. Osaka and I. Tanaka, J. J. Appl. Phys. 28(6), 1050 (1989).

3. T. Iwabuchi, C. Chuang, G. Khitrova, M. E. Warren, A. Chavez-Pirson, H. M. Gibbs, D. Sarid, and M. Gallagher, Proc. SPIE, March 1990.
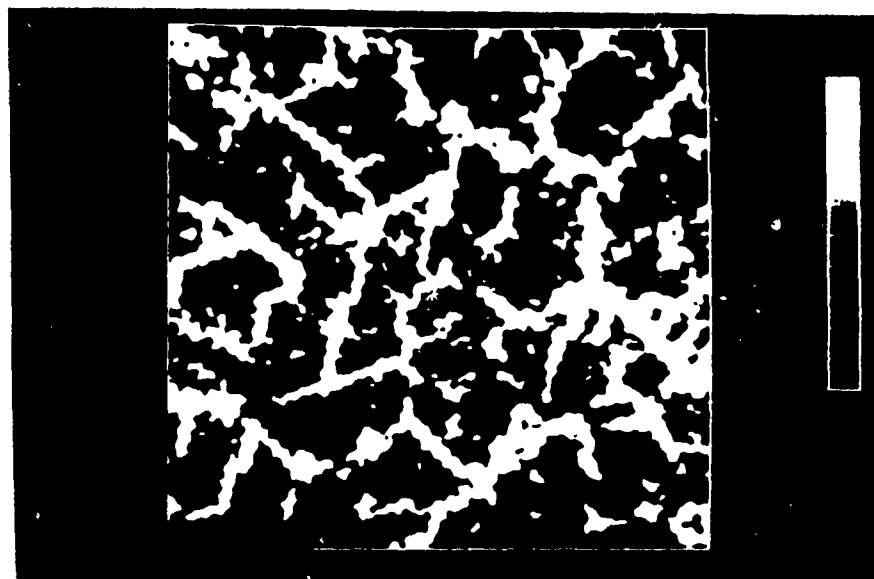
Sarid

Fig. 3.   Large scale image of hexagonally packed quantum dots.
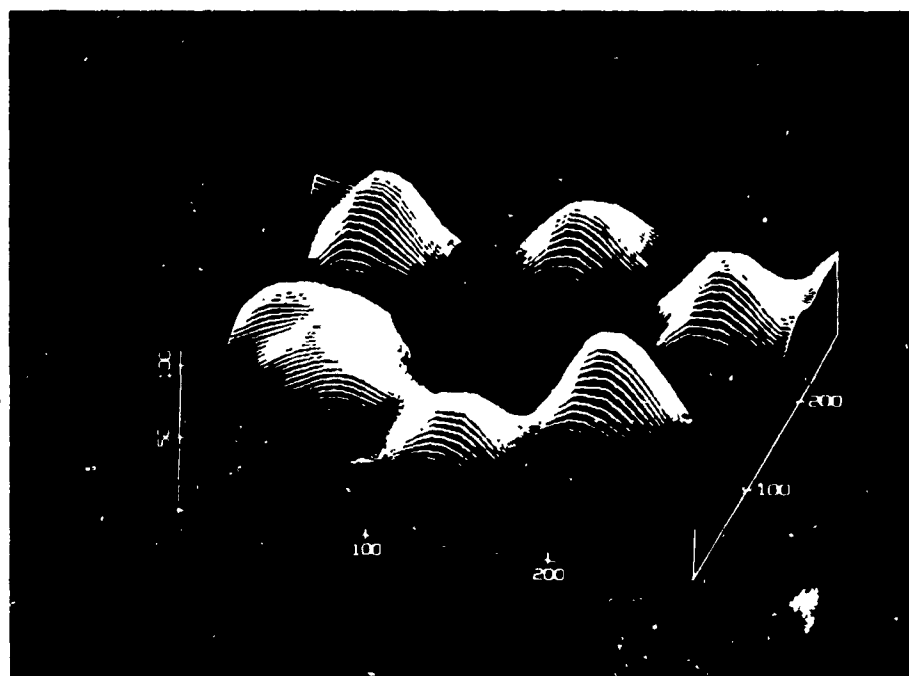

Fig. 4.   A close-up view of a single ring of quantum dots.

COHERENT AND NONLINEAR EFFECTS IN SEMICONDUCTORS

N. Peyghambarian

PUBLICATIONS

1. Y.Z. Hu, S.W. Koch, M. Lindberg, and N. Peyghambarian, "Theoretical and experimental results on Coulomb effects in semiconductor quantum dots," Phys. Stat. Sol. (b) 159, 249 (1990).

2. R.A. Morgan, S.H. Park, S.W. Koch, and N. Peyghambarian, "Experimental studies of the nonlinear optical properties of CdSe quantum confined microcrystallites," Semicond. Sci. Technol. 5, 544 (1990).

3. N. Peyghambarian and S.W. Koch "Semiconductor Nonlinear Materials," in *Nonlinear Photonics*, H.M. Gibbs, G. Khitrova and N. Peyghambarian, eds., (Springer-Verlag, Berlin, 1990).

4. V. Esch, B. Fluegel, G. Khitrova, H.M. Gibbs, Xu Jiajin, K. Kang, S.W. Koch, L.C. Liu, S.H. Risbud, and N. Peyghambarian, "State-filling, Coulomb, and trapping effects in the optical nonlinearities of CdTe quantum dots in glass," Phys. Rev. B 42, 7450 (1990).

5. N. Peyghambarian, S.W. Koch, H.M. Gibbs, and H. Haug, "Nonlinear optical materials and devices," in *Nonlinear Optics and Optical Computing*, S. Martellucci and A.N. Chester, eds., (Plenum Pres, New York, 1990).

6. N. Peyghambarian, B. Fluegel, M. Lindberg, S.W. Koch, D. Hulin, A. Migus, M. Joffre, and A. Antonetti, "Femtisocond spectral hole burning in CdSe quantum dots," accepted for publication in IEEE Journ. of Q. Elect., Nov. 1989.

7. N. Peyghambarian, S.H. Park, R.A. Morgan, B. Fluegel, Y.Z. Hu, M. Lindberg, S.W. Koch, D. Hulin, A. Migus, J. Etchepare, M. Joffre, G. Grillon, A. Antonetti, D.W. Hall, and N.F. Borrelli, "Optical nonlinearities and femtosecond dynamics of quantum confined CdSe microcrystallites," in *Optical Switching in Low-Dimensional Systems*, H. Haug and L. Banyai. eds., (Academic Press, 1989).

8. V.S. Williams, G.R. Olbright, S.W. Koch, B.D. Fluegel, and N. Peyghambarian, "Optical nonlinearities and ultrafast carrier dynamics in semiconductor doped glasses," J. Mod. Opt. 35, Dec. 1988 (invited review article).

9. N. Peyghambarian and H.M. Gibbs, "Semiconductor optical nonlinearities and applications to optical devices and bistability," in *Optical Nonlinearities and Instabilities in Semiconductors*, H. Haug, ed., (Academic Press, New York, 1988).

10. N. Peyghambarian and S.W. Koch, "Femtosecond and coherent effects in bulk CdSe and CdS_xSe_{1-x} doped glasses," Revue Phys. Appl. 22, 1711 (1987).

11. G.R. Olbright, N. Peyghambarian, S.W. Koch, and L. Banyai, "Optical nonlinearities of glasses doped with semiconductor microcrystallites," Opt. Lett. 12, 413 (1987).

12. R. Jin, J.P. Sokoloff, P.A. Harten, C.L. Chuang, S.G. Lee, M. Warren, H.M. Gibbs, N. Peyghambarian, J.N. Polky, and G..\. Pubanz, "Subpicosecond all-optical modulation using the optical Stark effect in a nonlinear directional coupler," Appl. Phys., Lett. 56, 993 (1990).

13. N. Peyghambarian, S.W. Koch, M. Lindberg, B. Fluegel, and M. Joffre, "Dynamic Stark effect of excitons and continuum states in CdS," Phys. Rev. Lett. 62, 1185 (1989).

14. S.W. Koch, N. Peyghambarian, M. Lindberg, and B.D. Fluegel, "Femtosecond dynamics of semiconductor nonlinearities: theory and experiments," in *Optical Switching in Low-Dimensional Systems*, H. Haug and L. Banyai, eds., (Academic Press, 1989).

15. J.P. Sokoloff, M. Joffre, B. Fluegel, D. Hulin, M. Lindberg, S.W. Koch, A. Migus, A. Antonetti, and N. Peyghambarian, "Transient oscillations in the vicinity of excitons and in the band of semiconductors," Phys. Rev. B38, 7615 (1988).

16. N. Peyghambarian, B. Fluegel, S.W. Koch, J. Sokoloff, M. Lindberg, M. Joffre, D. Hulin, A. Migus, and A. Antonetti, "Femtosecond transient and dynamic Stark effect in semiconductors," in *Ultrafast Phenomena VI*, T. Yajima and C. B. Harris, eds., (Springer-Verlag, Berlin, 1988).

17. B. Fluegel, N. Peyghambarian, G. Olbright, M. Lindberg, S.W. Koch, M. Joffre, D. Hulin, A. Migus, and A. Antonetti, "Femtosecond studies of coherent transients in semiconductors," Phys. Rev. Lett. 59, 2588 (1987).

18. V. Williams, Z.Z. Ho, N. Peyghambarian, W.M. Gibbons, R.P. Grasso, M.K. O'Brien, P.J. Shannon, and S.T. Sun, "Picosecond all-optical logic gate in a nonlinear organic etalon," Appl. Phys. Lett., Dec. 3, 1990.

19. S.W. Koch, N. Peyghambarian, and H.M. Gibbs, "Band-edge nonlinearities in direct-gap semiconductors and their application to optical bistability and optical computing," J. Appl. Phys. 63, R1 (1988) (invited review article).

20. R. Jin, C. Hanson, M. Warren, D. Richardson, H.M. Gibbs, N. Peyghambarian, G. Khitrova, and S.W. Koch, "Room-temperature single-wavelength optical latching circuits using GaAs bistable devices as logic gates," Appl. Phys. B 45, 1 (1988).

21. N. Peyghambarian, S.H. Park, S.W. Park, A. Jeffery, J.E. Potts, and H. Cheng, "Room-temperature excitonic optical nonlinearities of molecular beam epitaxially grown ZnSe thin films," Appl. Phys. Lett. 52, 182 (1988).

22. S.H. Park, J.F. Morhange, A.D. Jeffery, R.A. Morgan, A. Chavez-Pirson, H.M. Gibbs, S.W. Koch, N. Peyghambarian, M. Derstine, A.C. Gossard, J.H. English, and W. Weigmann, "Measurements of room-temperature band-gap-resonant optical nonlinearities of GaAs/AlGaAs multiple quantum wells and bulk GaAs," Appl. Phys. Lett. 52, 1201 (1988).

Conference Papers and Talks

23. N. Peyghambarian, "Femtosecond excitonic dynamics in quantum microstructures," International Conference on Solid State Devices and Materials, Aug. 22-24, 1990, Sendai, Japan.

24. Y.Z. Hu, M. Lindberg, S.W. Koch, and N. Peyghambarian, "Coulomb effects in semiconductor quantum dots," proceedings of SPIE Conference, vol. 1216, ed. N. Peyghambarian, Jan. 16-17, 1990, Los Angeles, CA.

25. N. Peyghambarian and S.W. Koch, "Optical Nonlinearities of Semiconductor Quantum Dots Probed by femtosecond Laser Pulses," USA-USSR binational symposium on *The Physics of Optical Phenomena and their Uses as Probes nof Matter*, Jan. 22-26, 1990, Irvine, California.

26. B. Fluegel, M. Lindberg, S.W. Koch, N. Peyghambarian, D. Huiin, A. Migus, M. Joffre, and A. Antonetti, "Femtosecond hole burning and nonlinear dynamics of quantum confined semiconductor-doped glasses," proceedings of SPIE Conference, vol. 1216, ed. N. Peyghambarian, Jan. 16-17, Los Angeles, CA.

27. J.P. Sokoloff, S.G. Lee, R. Jin, P. Harten, R. Binder, S.W. Koch, H.M. Gibbs, and N. Peyghambarian, "Femtosecond recovery of exciton bleaching in the optical Stark effect," submitted to the International Quantum Electronics Conference, Anaheim, CA, May 23-27, 1990.

28. C. Chuang, R. Jin, M.E. Warren, H.M. Gibbs, J.P. Sokoloff, P.A. Harten, N. Peyghambarian, J.N. Polky, and G.A. Pubanz, "Fabrication and performance of GaAs-MQW nonlinear directional couplers," Proc. SPIE 1216, ed. N. Peyghambarian, Jan. 16-17, 1990, Los Angeles, CA.

29. J.P. Sokoloff, P.A. Harten, R. Jin, C.L. Chuang, M. Warren, H.M. Gibbs, S.G. Lee, and N. Peyghambarian, "Subpicosecond all-optical modulation using the optical Stark effect in a nonlinear directional coupler," Proc. SPIE 1148, 13 (1989).

30. S.H. Park, B.D. Fluegel, R. Morgan, M. Joffre, J. Sokoloff, S.W. Koch, N. Peyghambarian, J.E. Potts, and H. Cheng, "Steady-state and time-resolved excitonic optical nonlinearities in MBE-grown ZnSe," in *Optical Bistability IV*, W. Firth, N. Peyghambarian, and A. Tallet, eds., (Edition d' Physique, Paris, 1988), page C2-185.

DEGREES OBTAINED BY GRADUATE STUDENTS WORKING ON THIS PROJECT

S. H. Park, PhD, 1988
R. A. Morgan, PhD, 1988
B. McGinnis, PhD, 1989

SCIENTIFIC PERSONNEL

N. Peyghambarian	B. McGinnis
Z.Z. Ho	S.H. Park
S.G. Lee	R.A. Morgan

RESEARCH FINDINGS

Objectives

The goals of this project have been two-fold: the study of the coherent effects in semiconductors; and the investigation of the dynamics of optical nonlinearities in quantum dots. Both of these projects have been very productive and stirred a substantial interest in the scientific community, resulting in several invited and contributed papers in major international conferences and scientific journals.

Progress

1. Optical Nonlinearities of Semiconductor Quantum Dots[1-11]

Three-dimensional quantum confinement effects in semiconductor microcrystallites occur when the particle size approaches the exciton Bohr radius. This confinement gives rise to interesting new effects that have attracted considerable attention recently. The novel optical properties of semiconductor microcrystallites make them potentially attractive for applications in fast opto-electronic devices. In particular, quasi-two-dimensional structures of GaAs-AlGaAs quantum wells where quantum confinement effects occur in one dimension have been studied extensively. A number of laboratories attempted to fabricate quasi-zero-dimensional structures using various techniques including colloidal suspension of semiconductor particles, electron beam lithography, and semiconductor microcrystallites in glass matrices.

Recently, glasses with small CdS, CdSe, and CdTe semiconductor microcrystallite sizes and rather uniform size distributions were grown both at Corning Glass Works and at the University of Arizona. These experimental glasses clearly exhibit quantum confinement effects. The crystallite size can be carefully controlled by varying the time and the temperature of heat treatment. The larger the heat treatment temperature and time, the larger the microcrystallite size.

The CdSe samples used in our initial experiments were grown under three different heat temperatures; 600°C, 650°C, and 700°C. The average crystallite diameters of these samples were measured to be 26 Å, 38 Å, and 61 Å, respectively, using small angle x-ray diffraction measurements. This is consistent with the fact that the average particle size increases with increasing heat treatment temperature.

We made several measurements on these quantum microstructures. Pump-probe spectroscopic techniques with nanosecond and femtosecond pulses were used to investigate

the size quantization effects. Nonlinear properties of the transitions between quantum confined electron and hole states were investigated for low temperatures and at room temperature. Femtosecond four-wave mixing and differential transmission spectroscopic techniques also were employed to study the excited state dynamics and relaxation times of the quantum dots. The homogeneous and inhomogeneous contributions to the lowest electronic transitions were measured by femtosecond spectral hole burning at various temperatures, as shown in Fig. 1. In this figure, the differential transmission spectrum (DTS) is plotted for a zero time delay between the pump and probe pulses. A positive (negative) DTS peak corresponds to bleaching (induced absorption) of the transition. The inhomogeneous linewidth is due to size and shape distribution of the crystallites. The spectral hole was accompanied by an induced absorption feature on the high-energy side. The spectral position of the burned hole depended on the excitation wavelength. For excitation on the low energy side of the lowest quantum confined transition, a slight shift of the hole towards the line center was observed. The hole width increased with pump intensity and the magnitude of the induced transparency saturated at our highest excitation level. The results were explained consistently by bleaching of one-pair states and induced absorption caused by the photo-excited two electron-hole pair states. We concluded that the presence of one electron in the excited state prevents further absorption of photons at the pair-transition energy and accounts for the major portion of the bleaching of the transition.

The optical nonlinearities of the CdSe dots as a function of microcrystallite size were investigated using a single beam saturation experiment for the three quantum confined samples. A simple absorption saturation model was used to analyze the data. The results indicated that the saturation intensity was larger for smaller semiconductor sizes (see Fig. 2). Therefore, the index change per unit of intensity, $\Delta n/I$ which is proportional to $(\alpha-\alpha_B)/I_s$ is larger for larger sizes. Here, Δn is the index change, α is the absorption at the peak of the transition, α_B is the background absorption, and I_s is the saturation intensity.

We also extended our quantum dot research to include CdS and CdTe quantum dots. These samples that were fabricated by Liu and Risbud, formerly at the Material Sciences Department of the University of Arizona, were investigagted in collaboration with Koch, Khitrova, and Gibbs. They exhibited distinct quantum confined transitins. We conducted nanosecond and femtosecond pump-probe experiments to investigate the optical properties of these samples. Figure 3 shows the linear absorption spectrum of a CdTe sample.
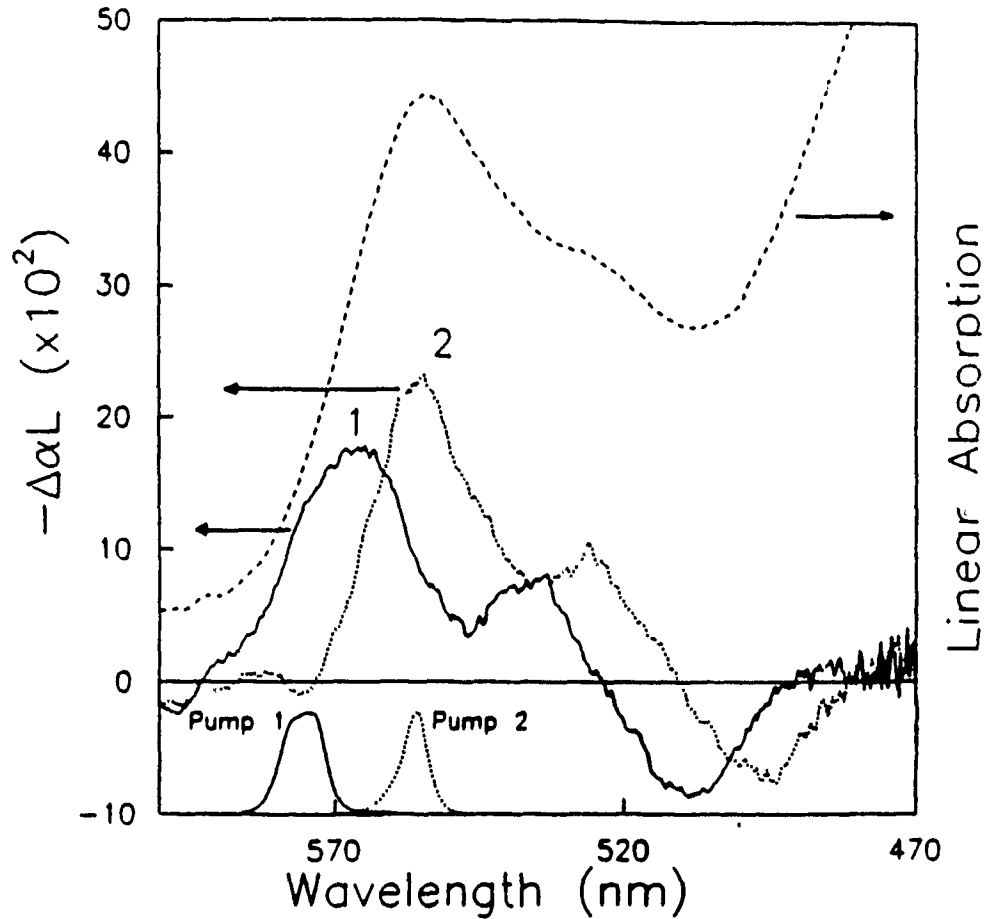
Fig. 1. The differential transmission of the 26-Å-radius sample for two pump wavelengths inside the A-transition at 10 K. The energetic positions of the pumps are indicated and the linear absorption spectrum is plotted. The linear absorption coefficient at the peak of the lowest quantum confined transition, A, is αℓ ~ 2.0.

The lowest quantum-confined transition (1s-1s) was clearly observed at a wavelength of ≅ 620 nm. The excitation by 100 fs laser pulses inside the lowest energy transition at λ = 620 nm leads to a nonlinear spectrum shown in Fig. 4. A positive DTS appears around the pump frequency and a negative DTS on the high-energy side of the positive DTS peak just like the CdSe case. Again, the positive DTS peak is attributed to the bleaching of the lowest quantum confined transition and the negative DTS peak is due to an induced absorption caused by two-pair transitions. The Coulomb interaction between the excited electron-hole pairs and the population mechanisms (state filling) are responsible for the observed behavior. The Coulomb interaction lowers the symmetry of the system, allowing the two-pair resonances to occur. We concluded that
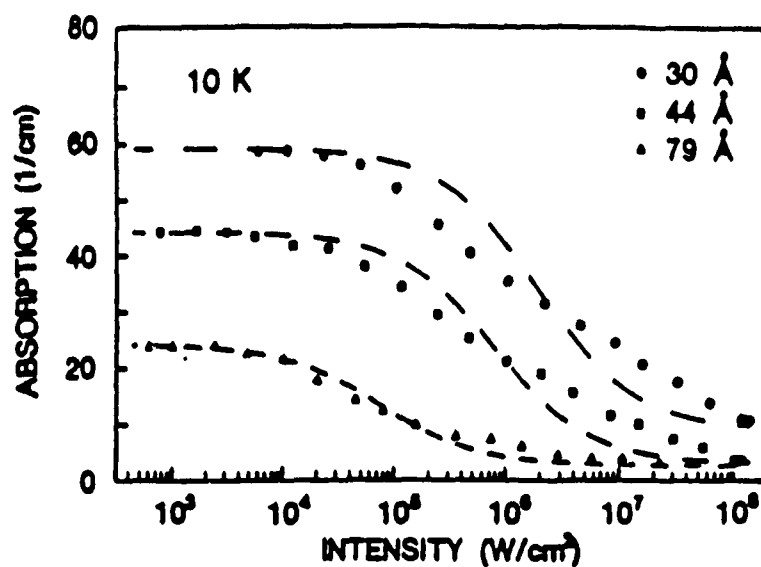
Fig. 2. Absorption at the peak of the first electronic transition versus intensity for the three quantum confined samples at 10 K.
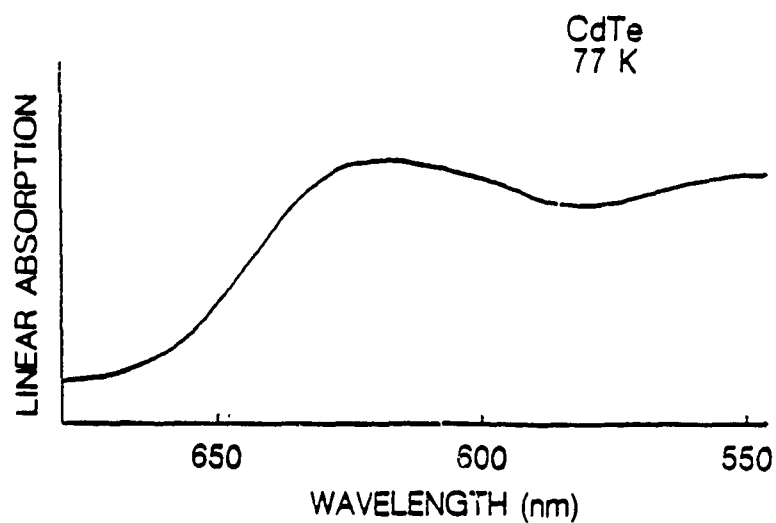

Fig. 3. The linear absorption spectrum of a CdTe quantum dot glass at 77 k.

Coulomb effects are important even in quantum dots. These interpretations were confirmed by calculations done by Koch et al. Figure 5 shows the DTS observed in CdS quantum dots in glass with nanosecond pumping. Similar features were also observed in CdS quantum dots.
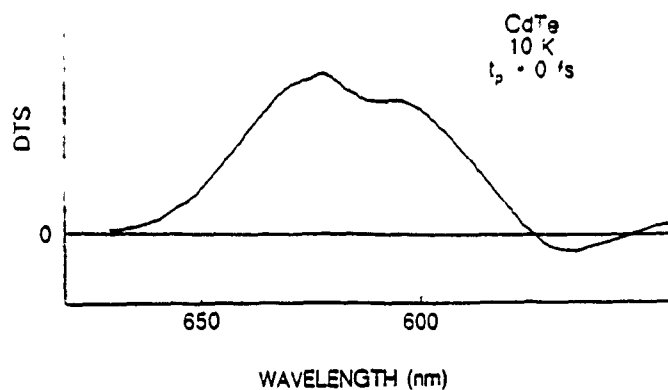
Fig. 4. The differential transmission spectrum of the CdTe quantum dot whose linear absorption is shown in Fig. 2.   The DTS resulted from pumping at 620 nm with ≅ 100 fs laser pulses.
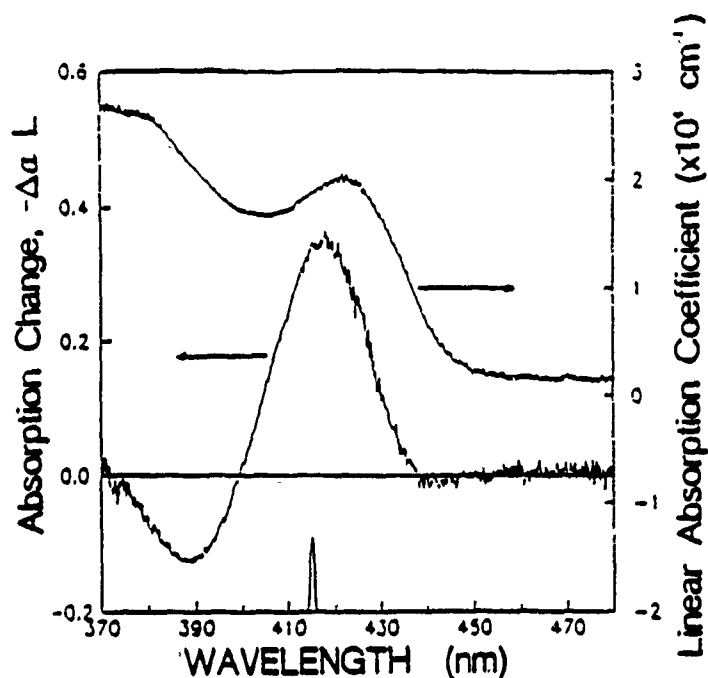

Fig. 5. The top curve is the linear absorption spectrum of a sample of CdS quantum dots in glass.   The bottom trace shows the energetic position of the pump pulse.   The intermediate trace is the change in the linear absorption spectrum as a result of excitation by the pump pulse.   L is the thickness of the sample.

2. Coherent Effects in Semiconductors[12-17]

Coherent light-matter interactions have been studied extensively in atomic spectroscopy. These interactions are readily observable in atomic systems as a result of the relatively long dephasing times. In semiconductors, on the other hand, the coherent coupling of the exciting light to the electron-hole transitions disappears very rapidly because of the various interaction processes of the electronic excitations. Until now only a few coherent processes in semiconductors have been observed experimentally. The anisotropic state filling in Ge, and phase coherence and orientational relaxation of excitons in GaAs, as well as the study of coherent coupling effects in pump-probe spectroscopy in dyes, have been investigated using picosecond pulses. In the femtosecond time domain, carrier orientational relaxation and band-to-band spectral hole burning, as well as the exciton optical Stark effect, have been reported.

We made the first observation of oscillatory structures in the probe transmission spectra around the exciton[17] when the semiconductor was excited spectrally below the exciton resonance and the probe pulse preceded the pump pulse. For the case of resonant interband excitation, similar oscillations also were observed around the central frequency of the pump pulse. We referred loosely to this class of effects as "coherent transients," including all the nonstationary features observed in semiconductors on time scales short enough that thermalization to quasi-equilibrium due to carrier-carrier or carrier-phonon scattering had not yet occured.

Several semiconductors including CdS, CdSe, GaAs, and $GaAs-Al_xGa_{1-x}As$ multiple-quantum wells were studied using femtosecond pump-probe spectroscopy to show that the observed coherent effects were quite general and did not depend on the specific semiconductor. A semiclassical theory was developed by S.W. Koch's group, which qualitatively explained all of the experimentally observed features. Figure 6 shows the measured and calculated spectra for CdS at 150 K.

We also made the first observation of the optical Stark effect of electron-hole continuum states in addition to the bound-exciton states under femtosecond excitation conditions[13] chosen to minimize the generation of real carriers (see Fig. 7). The experimental results agreed well with calculations using the generalized semiconductor Bloch equations.

We studied the influence of the generated real carriers by monitoring the DTS for positive time delays, after the pump pulse has left the sample. In Fig. 8 we show the DTS around the C exciton in CdS for $t_p \cong 0$ and +200 fs. Clearly, at 200 fs the
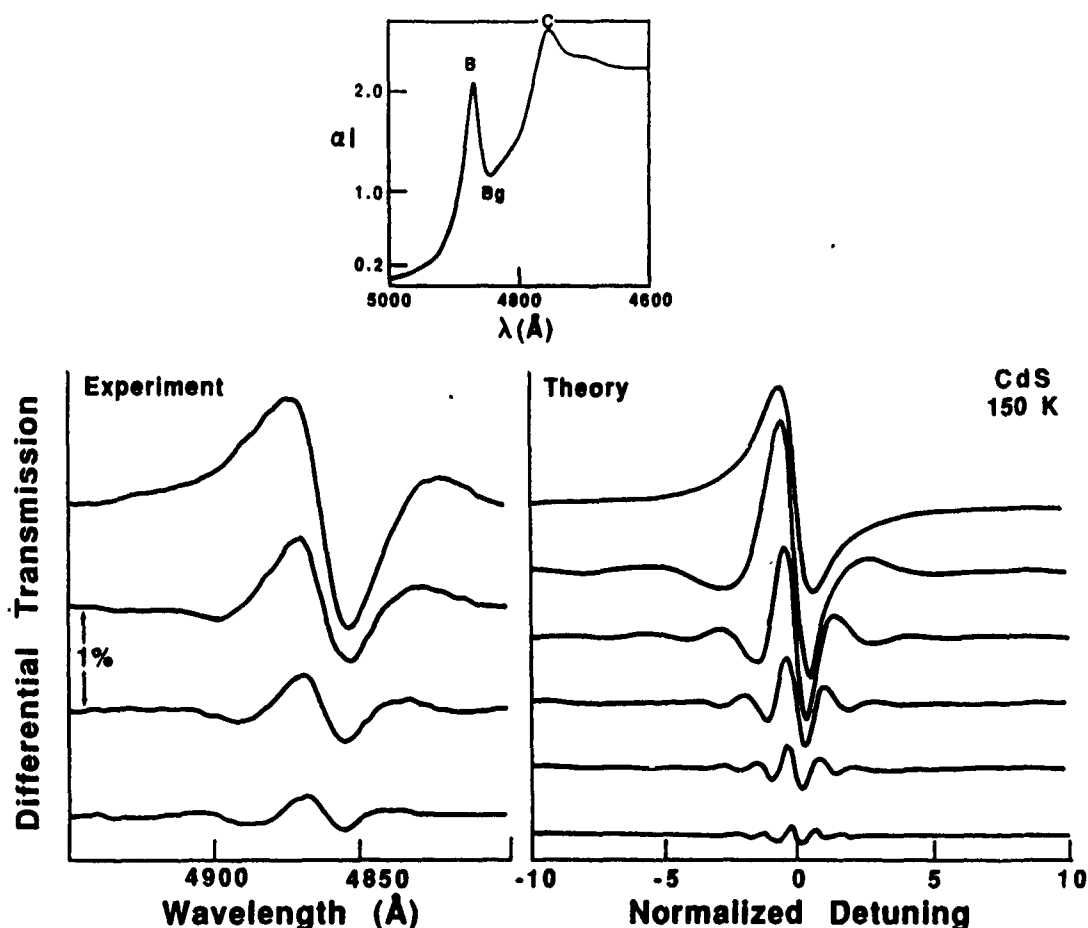
Fig. 6. a) The measured oscillatory behavior of DTS for negative time delays. The spectra are 50 fs apart. b) The calculated DTS for negative time delays. Inset: The linear absorption spectrum of CdS at 150 K for E_p 11 C.

dispersive features have recovered completely and only a small longer-lived effect due to real carriers remains. However, these long-lived real excitations observed at later time delays do not contribute to the spectra at zero or negative time delays with the same strength. For two-photon absorption the carrier concentration follows the integral of the square of the pump pulse, which reaches its maximum value after the pump pulse. At t = 0, when the electric field of the pump pulse is maximum, the carriers reach, at most, half of their maximum value.

In summary, the goals that we set for this project were reached.

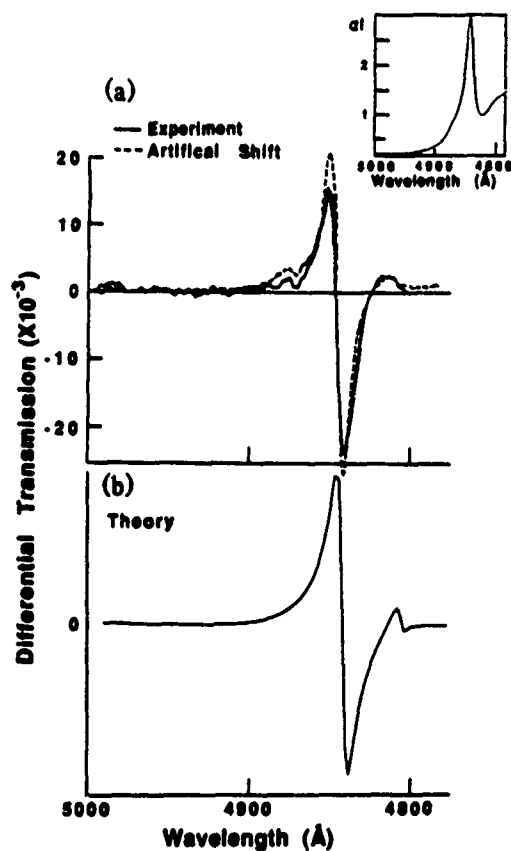Fig. 7. a) The measured DTS in the vicinity of the B exciton (full line) and its comparison with a pure shift of the absorption spectrum (dashed line) (see the text for description). b) The calculated DTS in the vicinity of the B exciton for $t_p = -25$ fs and a pump pulse duration of 60 fs.
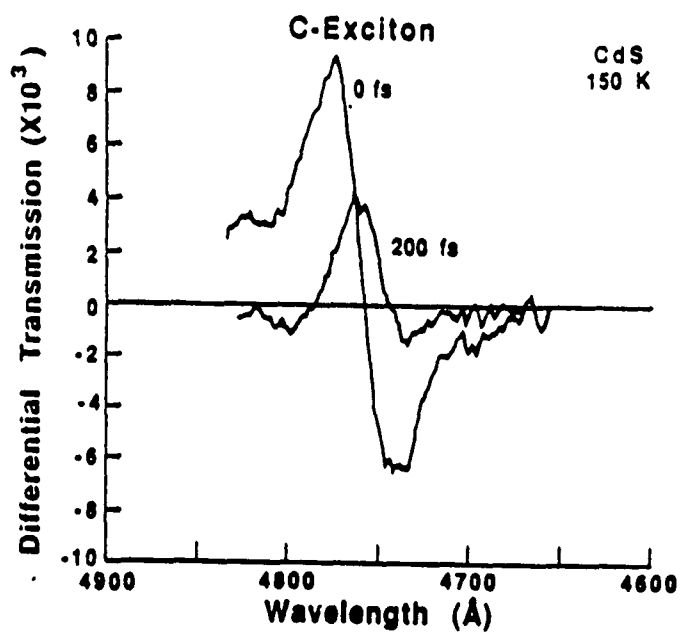
Fig. 8. The measured DTS in the vicinity of the C-exciton in CdS at 150 K for the time delays of 0 fs and 200 fs.

NONLINEAR ORGANICS FOR GUIDED WAVE DEVICES

Ray Zanoni and George I. Stegeman

PUBLICATIONS

Included in the publications list (marked *) are the results of previously supported work on nonlinear grating phenomena in InSb waveguides.

1. G.I. Stegeman, R. Zanoni, and C.T. Seaton, "Nonlinear organic materials in integrated optics structures," Materials Research Society Symp. Proc. 109, 53-64 (1988).

2. G.I. Stegeman, R. Zanoni, N. Finlayson, E.M. Wright, and C.T. Seaton, "Third order nonlinear integrated optics," review for J. of Lightwave Technology 6, 953-970 (1988).

3. G.I. Stegeman, E.M. Wright, N. Finlayson, R. Zanoni, C.T. Seaton, L. Thylen, S. Wabnitz, S. Trillo, and Y. Silberberg, "Nonlinear all-optical guided wave devices: operating characteristics and material trade-offs," Proceedings of SPIE Conference on Electrooptics 864, 24-34 (1987).

4. R. Burzynski, P. Banhu, P. Prasad, R. Zanoni, and G.I. Stegeman, "Nonlinear grating coupler measurements of thermal and electronic nonlinearities in a nonlinear polymer film," Appl. Phys. Lett. 53, 2011-2013 (1988).

5. G.I. Stegeman, R. Zanoni, K. Rochford, and C.T. Seaton, "All-optical guided wave devices," pp. 257-576 in Proceedings of NATO Workshop on *Nonlinear Optics in Polymers*, Nice, 1988.

6. G.I. Stegeman, R. Zanoni, E.M. Wright, N. Finlayson, K. Rochford, J. Ehrlich, and C.T. Seaton, "Review of nonlinear integrated optics devices," pp. 369-381 in *Organic Materials for Nonlinear Optics*, R.A. Hann and D. Bloor, eds. (Royal Soc. Chem., London, 1989).

7. K.B. Rochford, R. Zanoni, and G.I. Stegeman, "Irreversible photo-induced bleaching in polydiacetylene thin films," Appl. Phys. Lett. 55, 1161-1163 (1989).

8. G.I. Stegeman and R.H. Stolen, "Waveguides and fibers for nonlinear optics," J. Opt. Soc. Am. B 6, 652-662 (1989).

9. K. DeLong, K. Rochford, and G.I. Stegeman, "Effect of two photon absorption on all-optical guided wave switching," Appl. Phys. Lett. 55, 1823-1825 (1989).

10. G.I. Stegeman, "Overview of nonlinear integrated optics," book chapter in Proceedings of Erice Summer School on "Nonlinear Waves in Solid State Physics," A.D. Boardman and T. Twardowski, eds. (in press).

11. G. Assanto, J.P. Sabini, N. Finlayson, G.I. Stegeman, S. Trillo, and S. Wabnitz, "Saturation of nonlinearities and waveguide device implications," Symposium on Nonlinear Optics, Proc. SPIE (in press).

12. G. Assanto, Q. Gong, R. Zanoni, G.I. Stegeman, R. Burzynski, and P.N. Prasad, "Efficient grating coupling and optical characterization of poly-4BCMU waveguides," Proc. SPIE (in press).

13. K.B. Rochford, R. Zanoni, Q. Gong, W.E. Torruellas, and G.I. Stegeman, "Waveguide channels and gratings in polydiacetylene films using photo-induced bleaching," Proc. SPIE 1147, 279-225 (1989).

14. G. Assanto, M.B. Marques, and G.I. Stegeman, "Grating coupling of light pulses into third-order nonlinear waveguides," J. Opt. Soc. Am. (in press).

15. W.E. Torruellas, R. Zanoni, M.B. Marques, G.I. Stegeman, G.R. Mohlmann, E.W.P. Erdhuisen, and W.G.H. Horsthuis, "Measurement of third order nonlinearities of side chain substituted polymers," Chem. Phys. Lett. (in press).

16. Q. Gong, G. Assanto, R. Zanoni, G.I. Stegeman, R. Burzynski, and P.N. Prasad, "Efficient grating coupling to poly-4BCMU optical waveguides," Appl. Optics (in press).

17. K.B. Rochford, R. Zanoni, G.I. Stegeman, W. Krug, E. Miao, and M.W. Beranek, "Measurement of nonlinear refractive index and transmission in polydiacetylene 4BCMU waveguides at 1.319 μm," Appl. Phys. Lett., (in press).

18. W.E. Torruellas, D. Neher, R. Zanoni, G.I. Stegeman, F. Kajzar, and M. Leclerc, "Dispersion measurements of the third order nonlinear susceptibility of polythiophene thin films," Chem. Phys. Lett. (in press).

19.[*] J. Ehrlich, G. Assanto, and G.I. Stegeman, "Butterfly bistability in grating coupled thin film waveguide," Opt. Commun. 75, 441-446 (1990).

20.[*] J. Ehrlich, G. Assanto, and G.I. Stegeman, "All-optical tuning of waveguide nonlinear distributed feedback gratings," Appl. Phys. Lett. 56, 602-604 (1990).

21.[*] G. Assanto, J.E. Ehrlich, and G.I. Stegeman, "Feedback enhanced bistability in grating coupling into InSb waveguides," Opt. Lett. 15, 411-413 (1990).

22.[*] J.E. Ehrlich, G. Assanto, and G.I. Stegeman, "Nonlinear guided-wave grating phenomena," Proc. SPIE 1280 (in press).

23.[*] J.E. Ehrlich, G. Assanto, T.H. Chiu and G.I. Stegeman, "Guided-wave bistability in indium antimonide thin films," J. Quant. Electron. (in press).

24.[*] G. Assanto and G.I. Stegeman, "Optical bistability in nonlocally nonlinear periodic structures," Appl. Phys. Lett. 56, 2285-2287 (1990).

Theses

1.   "Nonlinear grating structures in InSb waveguides," J.E. Ehrlich, Optical Sciences Center, University of Arizona (1989).

2.   "Optical cubic susceptibility disperson of some transparent thin films," W. Torruellas, Optical Sciences Center, University of Arizona (1990).

3. "Linear and nonlinear optical properties of polydiacetylene waveguides," K. Rochford, Optical Sciences Center, University of Arizona (1990).

SCIENTIFIC PERSONNEL

G.I. Stegeman   K. Rochford
R. Zanoni   D. Kim
W. Torruellas   Q. Gong
G. Assanto   J.E. Ehrlich

RESEARCH FINDINGS

The detailed results of this research program will be discussed in a number of separate sections. First we will describe the new instrumentation developed, third harmonic generation (THG), and a new pulse amplitude modulation Mach–Zehnder interferometer. Since many of the measurements were made on poly-4BCMU films, these will be discussed in the succeeding section including nonlinear characterization, waveguide fabrication and characterization, and photobleaching. Next, nonlinear measurements on other interesting materials will be presented. Miscellaneous experiments will be discussed in Section 4. Major findings are summarized in the conclusions.

1. New Measurement Techniques

A THG apparatus was developed to cover the spectral range $0.95 \rightarrow 1.9$ μm. The laser was an injection seeded GCR-4 Spectra Physics Nd:YAG laser. By using combinations of a doubler, a dye laser, wave mixing and Raman cells we almost continuously covered the desired wavelength range.

The samples were either spin-coated, cast, or evaporated onto fused silica substrates. First, reference THG fringes were taken for a specific spot on the sample, and the film-sample experiments were performed on exactly the same location. This allowed us to obtain both the amplitude and phase of $\chi^{(3)}$ at each wavelength studied. The film thicknesses were measured with a profilometer, and the uncertainty in this measurement was the major source of uncertainty in the $\chi^{(3)}$ values. All experiments were done in vacuum, eliminating the air contribution. Data acquisition and analysis was automated, based on a PC, which proved to be reliable. It allowed us to make the first measurements of the real and imaginary components of $\chi^{(3)}$ over broad spectral ranges.

A new pulse-modulated Mach-Zehnder interferometer was built for operation at 1.3 μm. In essence, we can measure the fringe shift between radiation transmitted through a reference arm and a beam transmitted through a channel waveguide. The power in the waveguide arm is varied between a low and high power value, and the fringe difference is used to evaluate the index change in the waveguide. The key is to electronically keep track of the fringe shifts for the high and low power beams for a pulse train from a mode-locked Nd:YAG operating at 1.31 μm with 60 ps pulses. When a single pulse is used for the high power pulse, the nonlinearity responsible for the fringe shift is electronic in nature. On the other hand, when a sufficiently large grouping of high power pulses is used, a thermal nonlinearity can be measured. In this case, the fringe shift is proportional to the number of pulses in the packet, in contrast to the electronic nonlinearity case where the fringe shift is independent of the number of pulses $\lambda/300$.

2. Poly-4BCMU Films and Waveguides

To the best of our knowledge, no "ideal" nonlinear organic material has been identified yet for device applications. Therefore, our strategy has been to work with currently available materials, which may not be ideal, but with which device geometries and concepts can be tested. Poly-4BCMU essentially is a long conjugated chain and, therefore, is expected to exhibit large nonlinearities due to π-electron delocalization along the chain. We were fortunate to obtain high quality poly-4BCMU from the Dupont Research Laboratories. This material was obtained in monomer form and was polymerized at the Radiation Measurements Facility, College of Engineering and Applied Sciences, Arizona State University by exposing the monomer to 50 Mrad millicuries of energy in a nuclear reactor. 4BCMU is a soluble polymer that can be dissolved in solvents such as chloroform and cyclopentanone. Work has been completed on methods of preparing the material to minimize transmission loss through the material.

2.1 Film Preparation and Characterization

Films have been prepared by both spin coating and solution casting. Film preparation is critical for fabricating low-loss waveguides out of 4BCMU films. For example, spincoating 4BCMU dissolved in chloroform leads to high loss waveguides because microcrystallites form in the film. On the other hand, films fabricated using cyclopentanone as the solvent lead to low loss waveguides. Spin coated films are birefringent (n_{TE} = 1.53 and n_{TM} = 1.57).

It is surprising, perhaps, that the refractive index of organic materials is known to an accuracy of 1% at best. This is probably a reflection of the fact that these materials

only recently have 'een projected for *optical* applications. We have used standard integrated optical distributed couplers, in this case gratings, to measure refractive indices accurately. We have developed very efficient grating couplers specifically designed for nonlinear polymeric materials.

The coupling gratings were ion-milled into the fused silica at the film–substrate interface following procedures developed previously in our laboratory. Both square and blazed gratings (for very high coupling efficiencies) were made. Poly-4BCMU films of two different molecular weights, 300,000 g/mole and 410,000 g/mole were used. To obtain uniform homogeneous films of controlled thicknesses, we used spin coating to spread poly-4BCMU onto fused-silica substrates. We measured coupling efficiencies as large as 45% for TE polarization in a 0.65-μm-thick film The efficiencies in TM polarization were much lower, since the blazed grating had been designed specifically to optimize the in-coupling of s-polarized light.

The refractive indices for TE and TM guided modes and the film thickness were obtained by measuring the coupling angles and "inverting" the planar waveguide equation for the three-layer geometry. The birefringence ($\Delta n = n_{TE}-n_{TM}$) of the low-molecular-weight samples was smaller than that of the higher-molecular-weight material. For the low-molecular-weight samples: $n_{TE} = 1.568$ and $n_{TM} = 1.535$ at $\lambda = 632.8$ nm, while at $\lambda = 1.064$ μm the values were slightly lower: $n_{TE} = 1.529$ and $n_{TM} = 1.502$. The polymer fraction of the higher molecular weight (410,000 g/mole), however, displayed much larger birefringence: $n_{TE} = 1.68$ and $n_{TM} = 1.58$ at $\lambda = 632.8$ nm. These results exhibit the large birefingence that occurs because the long molecular chains lie preferentially in the plane of the surface due to the spinning process. Furthermore, with changes in molecular weight, the large changes in refractive index show the importance of having narrow-molecular-weight distributions. Strong scattering can occur due to inclusions of different molecular weight.

The waveguide losses were estimated by measuring the total waveguide throughput after propagation over a given distance using two grating couplers. The estimated losses were larger than 5 dB/cm for a 0.65-μm-thick film, with propagation over distances $\geq$ 1 cm at $\lambda = 1.064$ μm. Lower losses were measured by detecting the out-of-plane scattered light over a fixed distance along the waveguide, using a fiber bundle and a photomultiplier tube.

We also have succeeded in making channel waveguides of poly-4BCMU in which the light is tightly confined. This is achieved by using very highly polarizable ions in the ion exchange, in this case Cs. First, 3 μm wide channel waveguides were fabricated

by Cs ion exchange into special potassium-rich Schott BGG21 glass. Then they were overcoated by thick films of poly-4BCMU. The exchange parameters, exhange time and temperature, were adjusted until > 90% of the guided power was concentrated in the poly-4BCMU film. Waveguide loses of $\cong$ 2 cm^{-1} were measured.

2.2 Nonlinear Characterization

Third harmonic generation has emerged as a powerful technique for measuring the non-resonant nonlinearity of polymers, identifying the position and strength of the two-photon absorption bands, and for identifying the physics of the nonlinearity. We have used this technique to study poly-4BCMU; however, our measurements included measuring the magnitude of the nonlinearity and separating this measurement into an amplitude and a phase. This allows a new degree of freedom in fitting to models. To improve fitting of the data, we also measured the dispersion in the two photon absorption spectrum.

Both the magnitude and phase of the THG signal were measured in the range 0.93 μm to 1.9 μm and are shown in Fig. 1. The main peak is the usual 3ω resonance associated with the first allowed excited state. Structure on the high energy (low wavelength) side is due to contributions from a pair of two photon states, forbidden in linear absorption.

We also performed two-photon absorption measurements over a limited wavelength range. The results verify the existence of a pair of two-photon states. The dominant one occurs at higher energies than the state allowed in single photon absorption, which is responsible for the absorption spectrum. The second-two photon peak is weak and its location is not well identified.

We also measured the nonlinear parameters at 1.31 μm directly with the hybrid Mach-Zehnder interferometer. Using a strip-loaded channel waveguide obtained from Boeing, we measured $n_2 = 5 \times 10^{-14}$ cm^2/W for the electronic nonlinearity, and a thermal nonlinearity of -9×10^{-17} cm^2/W for a single 60 picosecond pulse. The two-photon absorption coefficient β was less than 0.2 cm/GW. For these values, the two-photon figure of merit ($2\beta\lambda/n_2$) was less than 1. To maintain good switching properties in a device values on the order of, and less than, unity are desirable. The small value of n_2 at this wavelength is probably due to a zero crossing of n_2 near 1.3 μm. We speculate that for λ > 1.31 μm, n_2 will be larger and the photon figure of merit will be less than unity.
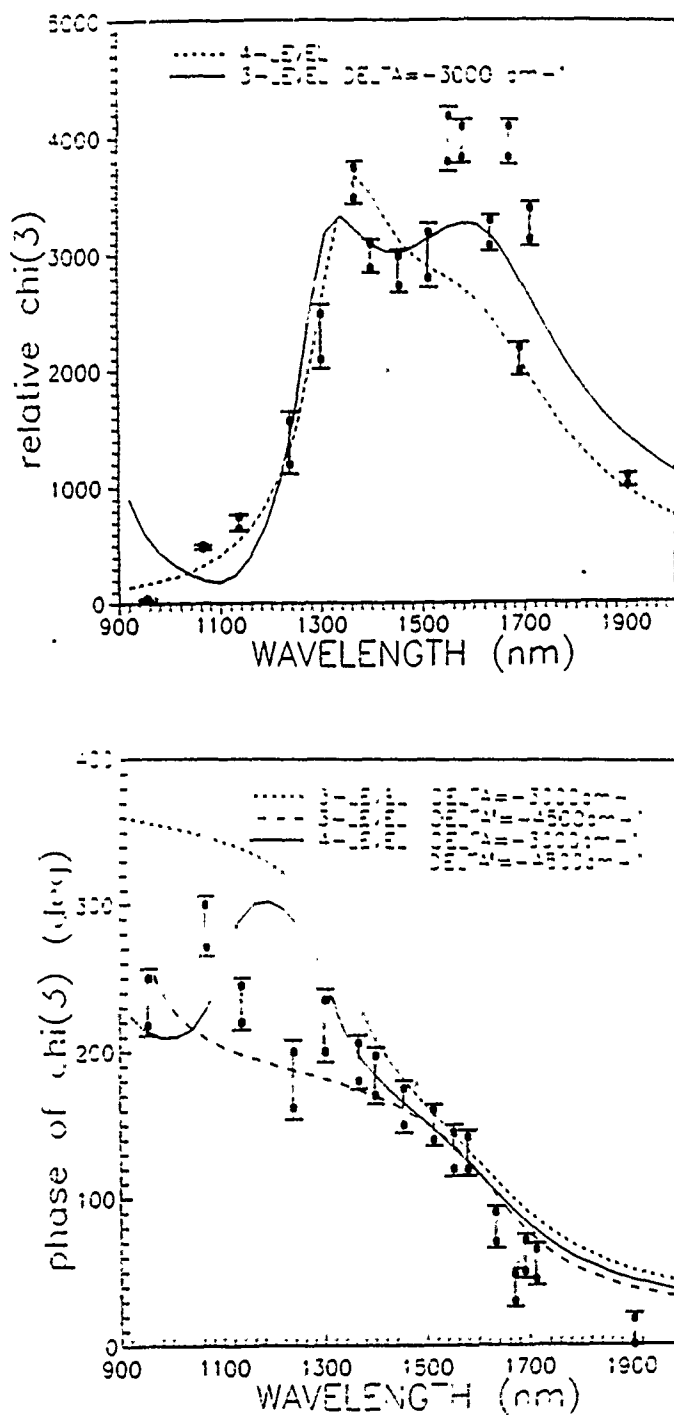
Fig. 1. *Experimentally determined magnitude (top) and phase (bottom) of* $\chi^{(3)}$ *(3ω) of poly-4BCMU relative to fused silica. The dashed line represents the best fit to a three-level model (1 two-photon state) and the solid line to the best fit to a four level model (2 two-photon states).*

Our overall assessment is that poly-4BCMU is not an optimum candidate for applications; however, it is a useful material for trying out new ideas.

2.3 Photobleaching

While establishing damage threshholds for poly-4BCMU, we observed changes in the transmission of the films with time as shown in Fig. 2. This occurred when 4BCMU was irradiated by light tuned to the absorption band of the material. This is accompanied by a change in the refractive index, and therefore, has the potential for writing gratings in waveguide and etalon structures.

Fig. 2. Absorbance of poly-4BCMU spin-coated film for various exposures of a 420 mW argon laser (514 nm) in a 400 μm FWHM beam. No exposure (top), 120 s (dashed), and 1000 s (bottom).

The basic *optics* results can be summarized as follows. For ≅1 μm films, the transmission on normal incidence changes by more than an order of magnitude. The total (cumulative) energy for 50% transmission change was 1.8 KJ/cm^2 at λ = 514 nm, and only 160 J/cm^2 at λ = 442 nm. For the low (high) molecular weight material, the maximum index change was -0.03 (-0.08), measured far from the absorption band (λ =

1060 nm). These values were obtained from grating coupling during the irradiation process. Our Kramers-Kronig modeling indicates that these values represent the far-from-resonance changes and should be independent of wavelength. There were no measureable increases in propagation losses in bleached versus unbleached regions. We also found that we could induce index changes by two photon effects (with $\lambda = 1060$ nm).

We investigated the physical mechanism for the changes using a number of techniques. Although infrared absorption and Raman scattering were measured before and after photobleaching, the two key measurements were the change in the absorption spectrum with irradiation and the change in the average molecular weight as determined by gel permeation chromotography (GPC). The absorption peak associated with the conjugated bonds was essentially reduced with increasing irradiation (and not shifted). The GPC, shown in Fig. 3, also showed that the average molecular weight (conjugation length) was dramatically reduced on irradiation. In addition, the saturated index was the same for both high and low molecular weights samples. Finally, no photobleaching occurred in vacuum.
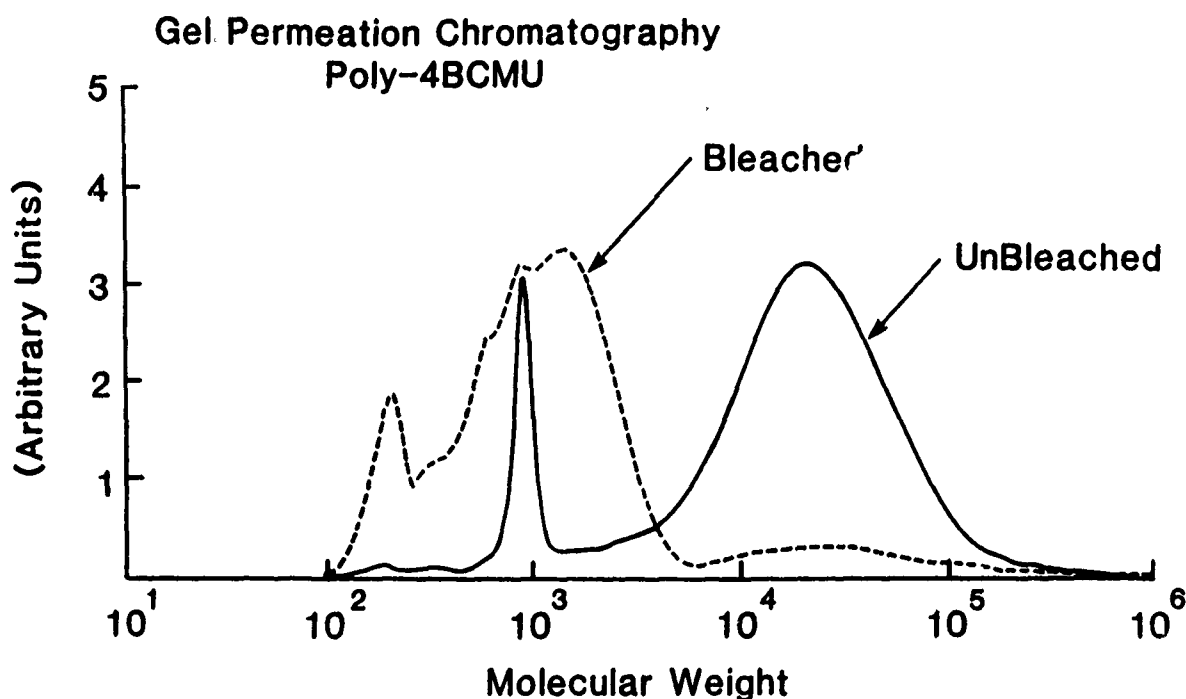

Fig. 3. Gel permeation chromatography of poly-4BCMU before and after photobleaching. Note the large reduction in the average molecular weight.

All of these results indicate photo-oxidation of the backbone chain of the molecules. That is, the conjugation, which is responsible for the nonlinearity, is reduced. This was verified by THG measurements on the film before and after bleaching. The nonlinearity was reduced by more than three orders of magnitude on irradiation to saturation.

In summary, the photobleaching occurs due to photo-oxidation of the poly-4BCMU backbone chain. It is accompanied by a reduction in the absorption peak associated with the conjugation and a reduction in the refractive index. The process can be stoppe ˙ ʰy removing oxygen, that is, by working in vacuum or by encapsulation.

.   .ːrns in the refractive index clearly can be written using photobleaching. Where   ιe material is bleached, refractive index is reduced. We used this feature to write gratings and channel waveguides. Because the writing of gratings is crucial to making distributed feedback structures, we concentrated on the grating aspect of the problem.

The growth of diffraction gratings produced by interfering two argon ion laser beams was monitored using a probe He-Ne beam. We found that we could easily write high definition diffraction gratings. By modulating the write beams, we identified two processes during the writing process, one due to thermal effects and the other due to the permanent photobleaching. The shortest wavelength gratings written were 0.6 μm and, based on our understanding of the process, 0.1 μm should be possible.

We made a grating coupler using the photobleaching process. A $\lambda = 855$ nm beam was coupled into a waveguide with $\cong 8\%$ efficiency. We could have optimized this value, but had no reason for doing so.

We made 10 μm wide channel waveguides by photobleaching. That is, we illuminated a poly-4BCMU film through a mask that had multiple stripes. Thus, the channel waveguides are nonlinear, and the surrounding regions are linear.

In conclusion, photo-induced refractive index changes can be induced. This effect is quite useful because refractive index changes on the order of 0.03 allow integrated optical structures to be formed directly by proper exposure of poly-4BCMU. Finally, the feasibility of channel and grating structures has been demonstrated. Encapsulating the exposed material after removing residual oxygen in the film stabilizes the integrated optical structures from further bleaching.

Recently we have found that two-photon absorption also can be used for permanent photobleaching. We did not quantify this process.

3. Nonlinearity in Other Polymers

We studied the nonlinear properties of a number of interesting materials, both by THG and nonlinear grating coupling.

A nonlinear grating coupler experiment on polimic acid was performed in collaboration with Paras Prasad's group at SUNY Buffalo. Waveguides with high efficiency grating couplers overlaid with a polymic acid film for guiding were fabricated. Because the film is nonlinear, the angle at which the optimum coupling into the waveguide occurs changes with incident (and guided wave) power. The power-dependent coupling efficiencies as a function of incident angle were measured with nanosecond, picosecond and femtosecond pulses. It can easily be shown, based on typical absorption coefficients, thermal conductivities and rate of change in index with temperature, that the thermal nonlinearity dominates experiments with nanosecond pulses. However, picosecond pulses usually sample only the electronic nonlinearity. Therefore detailed analysis of multiple experiments allowed us for the first time to identify both the thermal and electronic contributions to the nonlinearity. In fact, it is our opinion that all previous waveguiding experiments with nonlinear organics utilized thermal nonlinearities. In principle, this coupling phenomenon can be used for all-optical switching.

Detailed spectral scans of $\chi^{(3)}$ showed a peak strongly shifted to the long wavelength side of the linear absorption. In addition, there was structure within the peak. Both of these results were unexpected and still remain to be interpreted. An example of the spectrum for DANS is shown in Fig. 4.

Two polythiophenes have been studied to locate the two-photon state. These materials are good approximation to long linear chains. Detailed THG of polythiophene films showed evidence for a two-photon state shifted away from the linear absorption peak, as predicted theoretically.

Also, pthalocyanine has been measured by THG at 1.9 μm. In contrast to previous observations at $\lambda = 1.06$ μm, it shows no significant nonlinearity at 1.9 μm: $\chi^{(3)}$ is less than 10^{-13} esu making it of little interest for nonlinear waveguide applications.

4. Miscellaneous Experiments

We have performed an all-optical switching experiment using the thermal nonlinearity of organic materials. A distributed feedback grating was fabricated into a glass substrate that subsequently was overcoated with a polystyrene film to make a waveguide. The grating had a periodicity of $\cong 0.2$ μm. Larger periodicity gratings also
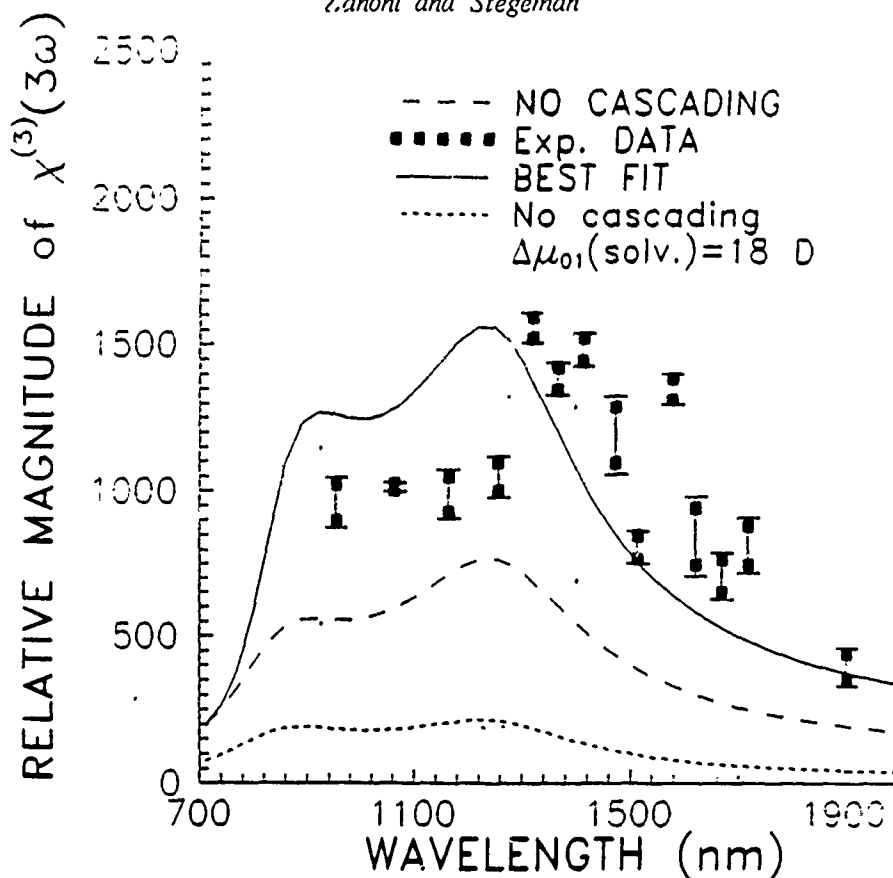
$$\text{RELATIVE MAGNITUDE of } \chi^{(3)}(3\omega)$$

Fig. 4. The experimentally determined dispersion of $\chi^{(3)}$ (3ω) for a DANS side-chain substituted polymer. The key result is that traditional models for third harmonic generation do not explain the data satisfactorally. However, there is evidence that cascading of second order nonlinearities is important.

were fabricated for coupling the light into and out of the waveguide. Using a cw dye laser tuneable around 0.62 microns, the response of the waveguide grating was measured for the TE_0 mode. A maximum grating transmissivity of less than 0.1% was found at the Bragg condition. When the grating region was illuminated from above with a pulsed CO_2 laser, the center wavelength of the grating response function was tuned due to thermal effects (Fig. 5). Thus it was possible to optically modulate the grating transmission with an on-off ratio in excess of 20 dB. The key to this demonstration is that we are able to design and fabricate multiple high quality gratings on a substrate to the tolerances needed for high efficiency all-optical switching. We would ultimately like to use the electronic nonlinearity of organic materials to produce this modulation.

The photobleaching investigation was extended to other organic materials, and comparable refractive index changes were found. For example, we have studied Methyl Red doped into polystyrene films. These guest-host systems show refractive index changes of -0.03 measured at $\lambda = 1.064 \mu m$ when photobleached in the visible. In fact,
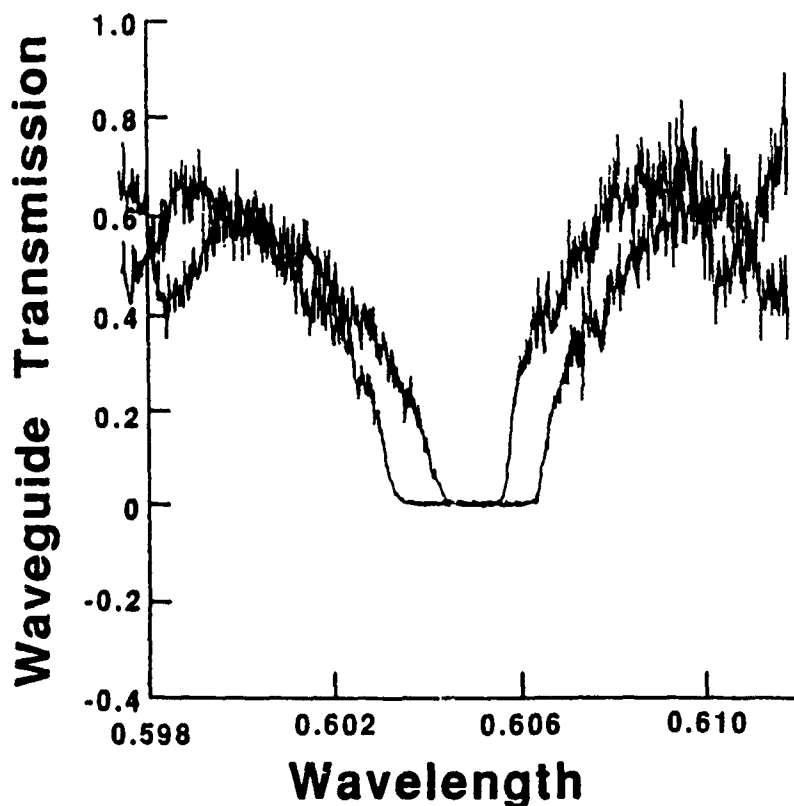
Fig. 5.   Transmission of a waveguide distributed feedback grating structure made in polystyrene as a function of probe wavelength. When the grating is illuminated with a CO_2 laser, the response shifts to lower wavelengths.

every nonlinear ($\chi^{(2)}$ and $\chi^{(3)}$) organic material that we have examined, including phtalocyanines, DANS etc. have shown permanent photobleaching in the presence of oxygen.   Encapsulation appears to inhibit the photobleaching process; therefore, guided-wave structures can be stabilized by encapsulation.

CONCLUSIONS

1. Third harmonic generation was used to study poly-4BCMU, DANS-based side chain polymers and polythiophenes.   Two photon states were identified.

2. The DANS based polymers exhibited a 2.5 power law dependence on the chain length, probably indicative that the nonlinearity arises due to cascading of second order nonlinearities.

3. A pulse-modulated Mach-Zehnder interferometer was constructed and used to measure the nonlinearity in poly-4BCMU channel waveguides at 1.3 μm.

4. The physics of photobleaching in poly-4BCMU was identified, and the effect was used to pattern channels and gratings in waveguide structures.

5. Tightly confined channel waveguides in poly-4BCMU were fabricated, and preliminary results on DFB gratings were obtained.

NONLINEAR PROPAGATION AND WAVE MIXING IN SODIUM VAPOR: GAIN/FEEDBACK APPROACH TO OPTICAL INSTABILITIES; CONICAL EMISSION; KALEIDOSCOPIC SPATIAL INSTABILITY

G. Khitrova and H. M. Gibbs

PUBLICATIONS

1. G. Khitrova, J. F. Valley, and H. M. Gibbs, "Gain/feedback approach to optical instabilities in sodium vapor," talk ThC4, IQEC'88.

2. G. Khitrova, J. F. Valley, and H. M. Gibbs, "Gain/feedback approach to optical instabilities in sodium vapor," Phys. Rev. Lett. 60, 1126-1129 (1988).

3. J. F. Valley, G. Khitrova, and H. M. Gibbs, "Gain/feedback approach to optical instabilities in sodium vapor," Optical Bistability IV, Aussois, France, March 23-25, 1988. Also G. Khitrova, J. F. Valley, and H M. Gibbs, J. Physique 49, C2-483-486 (1988).

4. J. F. Valley, G. Khitrova, and H. M. Gibbs, "Observation of raman-gain lasing and four-wave mixing in sodium vapor," postdeadline paper, CLEO/88, Anaheim, CA, April 25-29, 1988.

5. G. Khitrova, J. F. Valley, and H. M. Gibbs, "Gain/feedback approach to optical instabilities in sodium vapor," International Conference on Nonlinear Optics, Cong, County Mayo, Ireland, May 3-6, 1988.

6. H. M. Gibbs, "Lasing and conical emission in sodium vapor," International Conference on Nonlinear Optics, Cong, County Mayo, Ireland, May 3-6, 1988. Invited talk.

7. G. Guisfredi, J. F. Valley, R. Pon, G. Khitrova, and H. M. Gibbs, "Optical instabilities in sodium vapor," J. Opt. Soc. Am. B 5, 1181-1192 (1988).

8. J. F. Valley, H. M. Gibbs, and G. Khitrova, "Lasing and conical emission in sodium vapor," Proceedings of NLO-88.

9. G. Guisfredi, J. F. Valley, R. Pon, G. Khitrova, and H. M. Gibbs, "Transverse delayed-feedback instabilities in Na vapor," Latin-American Meeting, 1988.

10. G. Khitrova, "Two-beam coupling in local and nonlocal media," International Conference on Laser Applications in Spectroscopy and Nonlinear Optics, Jan. 4-9, 1989, Madras, India. Invited talk.

11. G. Khitrova, "Lasing, instabilities, and transverse effects in Sodium vapor," International Conference on Laser Applications in Spectroscopy and Nonlinear Optics, Jan. 4-9, 1989, Madras, India. Invited talk.

12. J. Valley, Ph.D. dissertation, "Nonlinear Optics in Sodium Vapor and Comparison with Doppler-Broadened Two-Level-Atom Theory," Optical Sciences Center, University of Arizona, 1989.

13. J. F. Valley, G. Khitrova, H. M. Gibbs, J. W. Grantham, and Xu Jiajin, "CW conical emission: a first comparison and agreement between theory and experiment," 1989 Annual Meeting of the Optical Society of America, Orlando, FL, Postdeadline talk PD-11.

14. G. Khitrova, J. F. Valley, H. M. Gibbs, J. W. Grantham, and Xu Jiajin, "CW conical emission: first comparison and agreement between theory and experiment," Topical Meeting on Nonlinear Dynamics in Optical Systems, Afton, OK, June 4-8, 1990.

15. J. F. Valley, G. Khitrova, H. M. Gibbs, J. W. Grantham, and Xu Jiajin, "CW conical emission: first comparison and agreement between theory and experiment," Phys. Rev. Lett. **64**, 2362 (1990).

16. J. W. Grantham, H. M. Gibbs, G. Khitrova, J. F. Valley, and Xu Jiajin, "Kaleidoscopic spatial instability," submitted to Phys. Rev. Lett.

SCIENTIFIC PERSONNEL

G. Khitrova   J. Grantham
H. M. Gibbs   Xu Jiajin
J. Valley

RESEARCH FINDINGS

Progress

1. Gain/Feedback Approach to Optical Instabilities

Silberberg and Bar-Joseph[1-4] have analyzed the onset of an optical instability as the simultaneous occurrence of sufficient gain and feedback to permit lasing at a new frequency.[5] The instability observed on the transmitted light then is merely the beat between the pump field and the newly generated lasing. We have used this gain/feedback approach in sodium vapor[4] using the Rayleigh gain to generate sideband lasing displaced from the driving laser field by 8 to 14 MHz. Raman-gain lasing also is seen, but it is displaced by the on-resonance Rabi frequency, typically 4 GHz or less here, rather than by the effective Rabi frequency, which is larger because of the detuning. *The new observations are Rayleigh-gain lasing with no external mirrors with use of counterpropagating pump beams,*[1-4] *Rayleigh-gain lasing without a foreign gas,*[6] *and Raman-gain lasing in a ring cavity.*

1.1 Pump/Probe Gain/Absorption Curve

The pump-probe or two-beam-coupling gain curve for a stationary Na atom already has been derived[7,8] and verified.[9] Here we adopt the nomenclature of Haroche and Hartman[7] and refer to the dispersion-shaped resonance at the laser frequency ν_L as "Rayleigh" (called $1/T_1$ in Ref. 4) and the gain peak at $\nu_L - \nu_{RE}$ as "Raman" (sometimes called Rabi[4] or three-photon[10] gain). Here the effective Rabi frequency is $\nu_{RE} = (|\delta\nu_L|^2 + \nu_R^2)^{1/2}$, where ν_R is the on-resonance Rabi frequency, $\delta\nu_L = \nu_L - \nu_0$, and ν_0 is the two-level-atom frequency. For moving atoms, one must integrate this curve over the velocity distribution; this has been expressed as easily calculable sums of plasma dispersion functions.[11-13] Figure 1 compares the detuned stationary-atom curve in Fig. 1(a) with the Doppler-broadened curve in Fig. 1(b) showing the ac Stark shift of the absorption peak and the shift and broadening of the Raman gain. The peak of the Raman gain occurs at a frequency ν given by $\nu \cong \nu_L \pm \nu_{RE}$ for a stationary atom, where $\pm$ is given by $\delta\nu L/|\delta\nu_L|$. For moving atoms and when the Doppler broadening is roughly equal to $\delta\nu_L$, as in Fig. 1(b), the Raman gain is much broader and its peak shifts to almost $\nu_L - \nu_R$. In contrast, the Rayleigh gain is Dopper free and hardly affected. Lasing will be described on the basis of these two gain mechanisms with use of two different feedback confirmations.

1.2 Experimental Apparatus

The experimental apparatus consists of a cw ring dye laser and sodium cell. The $\cong$ 900-mW single-mode output power of the dye laser is diffracted from an acousto-optic Bragg cell so that any feedback is shifted by 80 MHz and has no effect on the dye-laser frequency. The beam then is spatially filtered, collimated, and focused by a 30-cm or 45-cm focal-length lens into the sodium with a maximum of 700 mW reaching the Na. For most of the measurements, the Na cell was a flow cell with a 9-mm length of the Na; the argon pressure was usually $\le$ 0.3 Torr. A 10-cm evacuated quartz cell was used to show Rayleigh-gain lasing at zero pressure. Beat frequencies up to 300 MHz could be observed with a photodiode and a Hewlett-Packard model 8568B spectrum analyzer. A Fabry-Perot interferometer (flat mirrors with R $\cong$ 0.98) was used to study lasing at frequencies differing from ν_L by more than 100 MHz. The detuning $\delta\nu_L$ is measured with Lamb-dip spectroscopy, and zero is defined as the center of the strongest (here the nearest) hyperfine transition.
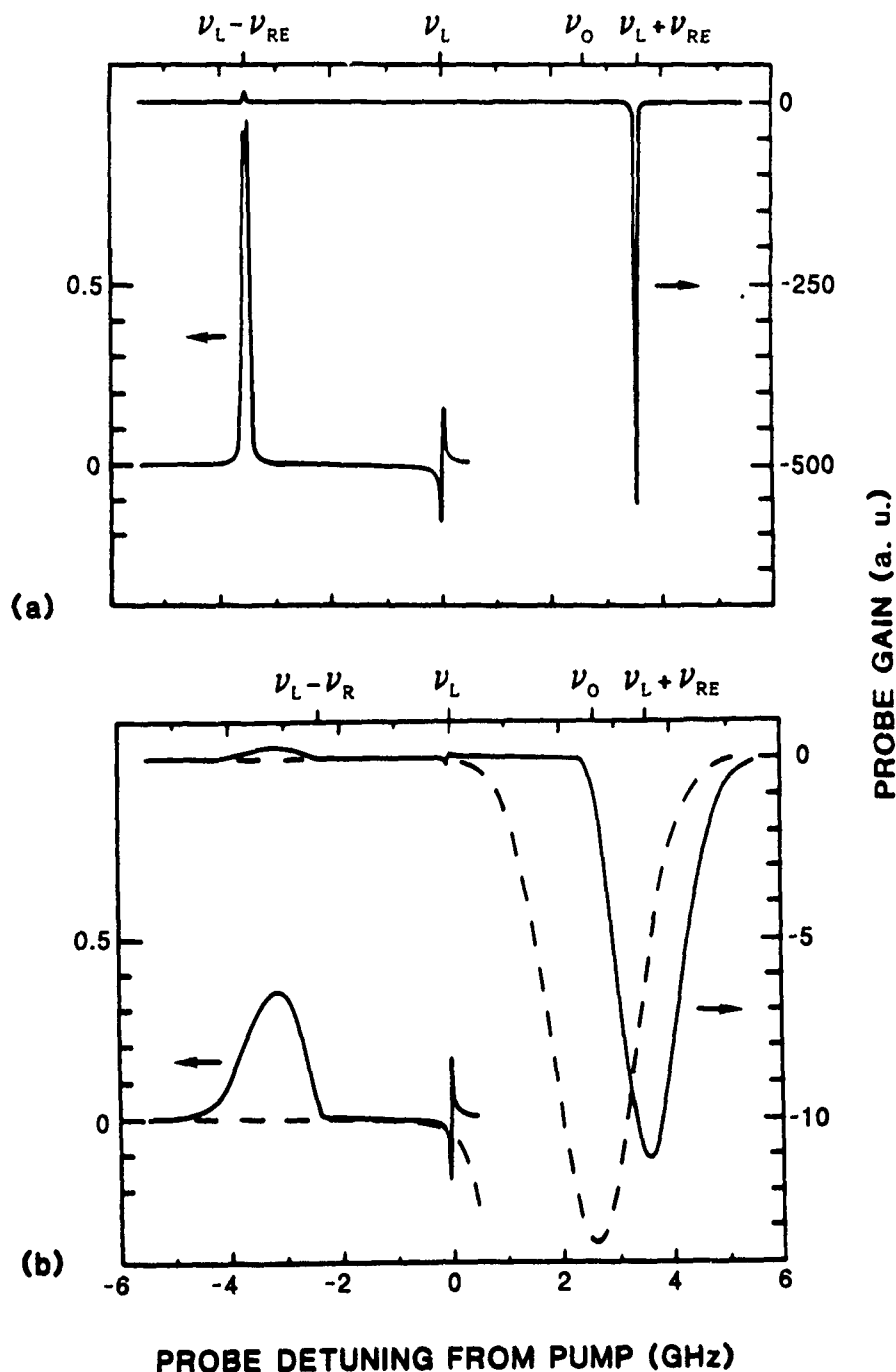
Fig. 1. Calculations (Ref. 11) of (a) the stationary-atom and (b) the Doppler-broadened probe-gain profiles for an intense pump at ν_L detuned by ν_L - ν_0 = -2.6 GHz (defocusing side) from the low-field line center ν_0. The Rabi frequency is ν_R = 2.4 GHz and the argon pressure 0.3 Torr. The abbreviation "a.u." stands for "arbitrary units." (a) The well-known ac-Stark-shifted absorption at ν_L + ν_{RE}. The 500× enlargement at the left shows Raman gain (peak value 14) at ν_L - ν_{RE} and Rayleigh gain peaked at about $(2\pi T_1)^{-1}$ to the right of ν_L. (b) For a Doppler width of 2 GHz one sees that the high-intensity absorption (solid curve) is shifted from the low-intensity absorption (dashed curve).

1.3 Counterpropagating-Beams Instabilities

For the counterpropagating-beams case, 300-mW beams were focused by two 30-cm focal-length antireflection-coated lenses; see Fig. 2 inset. Two new observations with counterpropagating-beams distributed feedback (DFB) were made: an optical instability by means of Rayleigh-gain lasing with no external cavity, and Rayleigh-gain lasing with zero foreign-gas pressure. The observation of mirrorless self-oscillation (i.e., lasing) is shown in Fig. 2. The zero-order DFB modes of our short samples are broad and essentially flat over the Rayleigh-gain region, which peaks at about 10 MHz from ν_L; consequently, lasing occurs at the peak of the gain curve. The lengths L here, 0.9 cm for the flow cell and 10 cm for the quartz cell, are both short compared with the long lengths proposed in Ref. 4, where the next-higher-order DFB mode at $c/2L$ is made to coincide with the Rayleigh-gain curve. Mirrorless lasing was reported previously in the pulsed regime in semiconductor crystals; because the processes were frequency degenerate, a small angle was required between the counterpropagating pumps in order to distinguish the lasing.[14] Here, the $\cong$ 10-MHz frequency shift facilitates detection by the heterodyne technique even for exact counterpropagation. Note that the generation mechanism for Rayleigh-gain lasing at $\nu_L + f$ is a two-beam coupling, but nearly degenerate four-wave mixing results in $\nu_L - f$ in the counterpropagating-beams case.

The second DFB observation, namely Rayleigh-gain lasing without foreign gas, was performed in the evacuated 10-cm Na cell. It emphasizes that a closed system (i.e., no collisions and no decay to an external reservoir) with large detuning can exhibit Rayleigh gain. In terms of a perturbation-expansion susceptibility, Rayleigh gain occurs in fifth order with no foreign gas and in third order with foreign-gas pressure.[6,11,12] Thus the zero-pressure Rayleigh-gain lasing requires more pump power than with pressure. This may explain why Grandclement, Grynberg, and Pinard[15] observed Rayleigh lasing only with pressure using Na in a ring cavity.[16]

1.4 Raman-Gain Lasing in a Ring Cavity

For the ring-cavity experiments, three highly reflecting flat mirrors and two 30-cm focal-length antireflection-coated lenses were used to form a ring cavity for the lasing with $L = 98$ cm; see Fig. 3 inset. The input was focused by a 45-cm lens, resulting in a 112-μm waist w [$I = I_0 \exp(-2r^2/w^2)$] in the Na. Since the pump beam passes through the Na in only one direction, there are no counterpropagating beams. Lasing occurs in only one direction in the cavity, namely in the forward direction with respect to the pump, because of the Doppler effect. In the case of a probe beam propagating in a
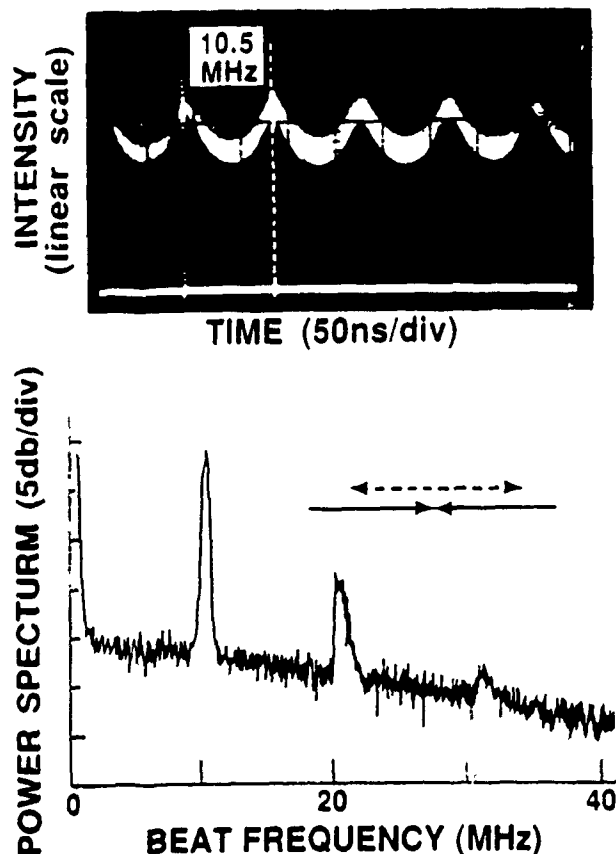
Fig. 2.   Time dependence and power spectrum of one of the counterpropagating pump beams after passing through the sodium vapor for $\delta v_L \cong -2.6$ GHz (defocusing side). The f = 10.5 MHz beat frequency arises mostly from lasing at the peak at $v_L + f$ of the Rayleigh gain and from emission at $v_L - f$; the 21-MHz peak is the beat between $v_L - f$ and $v_L + f$.   Inset: Geometry of the counterpropagating pumps (solid arrows) and Rayleigh lasing (dashed arrows).

direction opposite to the pump beam, the averaging over the velocity distribution reduces the gain strongly.   For $\gamma v_L = -4.1$ GHz, the Raman-gain lasing at v begins at $v_L - v =$ 4 GHz, just slightly larger than the $v_R \cong 3.7$ GHz calculated from the 680-mW input power, the 112-μm waist, and the dipole moment[9] of Na.   This 4-GHz shift of the Raman lasing from v_L is much less than the 5.7 GHz would be if the atoms were stationary.   Because of the broadened gain curve, several longitudinal modes of the ring cavity may be above the Raman lasing threshold, as shown in Fig. 3(a) for $\delta v_L = -2.6$ GHz.   The mode spacings range from 240 to 270 MHz, different from $c/L = 306$ MH because of dispersion.   Comparison with the calculated plane-wave gain curve is made in Fig. 3(b), where $v_R = 2.4$ GHz gives a better fit because of absorption and defocusing.   The lasing has a waist of only 67 μm in the sodium and makes an angle of

about 0.9° relative to the pump beam, so that it uses the gain in the uniform portion of the pump beam. This justifies the use of the plane-wave gain curve. Rayleigh-gain lasing in the ring cavity also was seen, as already reported by Grandclement, Grynberg, and Pinard.[15]
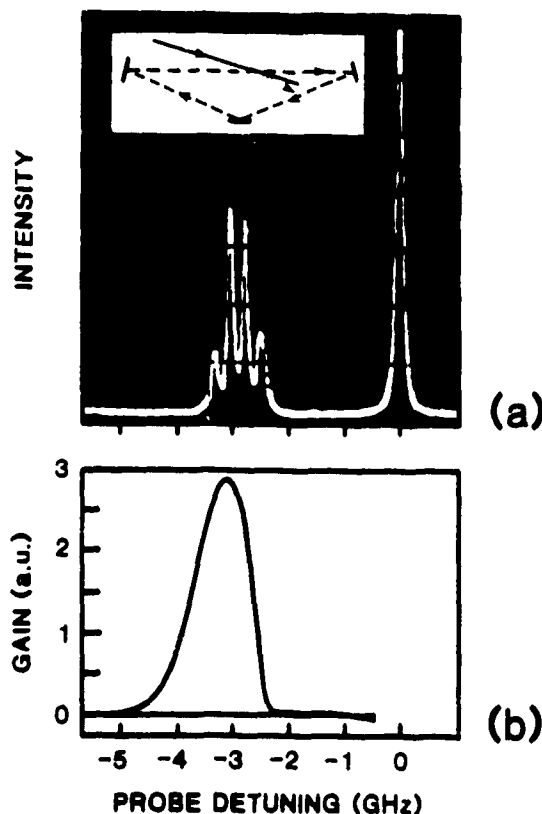

(a)

(b)

PROBE DETUNING (GHz)

Fig. 3. Raman-gain lasing in Na in a ring cavity (see inset) for $\delta v_L \cong -2.6$ GHz (defocusing side). (a) Fabry-Perot spectrum showing laser light (injected external to the ring cavity) at $v - v_L = 0$ and lasing of four Raman-gain ring-cavity modes for $v - v_L \cong -3$ GHz. (b) Raman-gain calculated curve from Fig. 1(b). (Note that the arbitrary units ["a.u."] here are 8 times those of Fig. 1(b)).

1.5 Discussion

It is interesting to note that two-beam coupling is common in photorefractive crystals. In fact, Rayleigh-gain lasing has been seen with use of a bismuth silicon oxide (BSO) photorefractive crystal in a ring cavity; the peak is shifted by only about 30 Hz.[17] The nonlocal photorefractive effect (diffusion limit) gives one $\pi/2$ phase shift, and the grating reflection for the Bragg condition gives another $\pi/2$ phase shift; together they add to the π phase shift needed for optimum transfer. Here there is no transfer for $v = v_L$ because the detuned two-level-medium polarization is local and in phase with the

stationary light grating; but, for a probe detuned by about 10 MHz, the light grating moves, causing the Na polarization to lag behind just enough to make the scattered beam in phase with the probe, as needed for the most efficient transfer.

Note that the ring-cavity lasing observed here is unidirectional, so that counterpropagation[18] instabilities do not occur. Both the ring-cavity and counterpropagating-beams lasings observed here have the same linear polarization as the pump(s), and so the polarization instability of Gaeta et al. and Kaplan and Law[19] did not occur. In fact, they use a nonlinear-medium description that does not apply to sodium vapor, as pointed out by Ducloy and Bloch.[20]

A signal field oscillating at $\nu_3 = \nu_L + f$ may interact with the strong field at ν_L to generate, by forward four-wave mixing, a field at $\nu_4 = 2\nu_L - \nu_3 = \nu_L - f$, or vice versa.[10,21,22] If the signal wave travels at an angle θ relative to the pump wave, then the generated wave will travel in the direction dictated by phase matching (roughly $-\theta$ for $\theta = 0.9°$).[21] Consequently, the ring-cavity emission does not include the complements of the Rayleigh and Raman lasings; however, those emissions are seen outside the cavity at the phase-matched angle. In the case of counterpropagating-beams, emissions are seen at both $\nu_L \pm f$ because the beams are essentially collinear (see Fig. 2) and both backward and forward four-wave mixing can contribute.

1.6 Summary

The gain/feedback approach is a stimulating alternative to direct probe-absorption measurements. Even more importantly, it is a powerful tool for studying the onset of optical instabilities. One can even manipulate the frequencies of the instabilities by controlling the interplay between the gain and feedback frequency profiles.

2. Cw Conical Emission: First Comparison and Agreement Between Theory and Experiment

2.1 Introduction

Since first observed by Grischkowsky,[23] conical emission has had a complicated and controversial history.[24,25] The phenomenon has been given many theoretical explanations but, until recently, no detailed comparison has been made between experimental observations and theoretical computations. An understanding of conical emission that occurs in one-pass propagation is essential to advances in the study of spatio-temporal instabilities in atomic vapors. We show excellent agreement between experimental observations and computations based on the complicated interaction of several well-known effects. Inclusion of many details was essential to achieve good agreement. These

details may have technical implications wherever intense beams must be tuned close to resonances, e.g., in isotope separation in which the generation of new frequencies in new directions may be important.

2.2 Experimental Apparatus

Our experiment employs a cw ring dye laser tuned to the high-frequency side of the D_2 resonance of sodium. The $\cong$ 850 mW single-mode output power of the dye laser is spatially filtered, collimated, and focused by a 30-cm-focal-length lens onto the cell entrance with a waist $w_0 \cong 75$ μm and with a maximum of 600 mW reaching the sodium in a 10-cm evacuated quartz cell; see Fig. 4(h). The laser beam is vertically, linearly polarized and travels horizontally. A Fabry-Perot interferometer (flat mirrors with R $\cong$ 0.98, finesse $\approx$ 100, usually $\cong$ 28-GHz free spectral range) was used to study the frequency spectrum of the output beam after recollimating the beam and isolating the cell from the Fabry-Perot with a polarizer/waveplate combination and neutral density filter. The detuning $\Delta\nu$ of the laser frequency from the atomic resonance is measured with Lamb-dip spectroscopy with zero defined as the midpoint between the two hyperfine transitions.

2.3 Theory

Our theoretical model is as follows. A strong cw pump beam $E_1(\omega_1)$, with Gaussian transverse profile, is focused onto the input of a sodium cell and is quasi-trapped during its propagation through the cell.[26,27] New frequencies, $E_3(\omega_3)$ with $\omega_3 > \omega_1$, are generated by a Raman gain[7,9,12,13,28,29] that amplifies resonance fluorescence.[30] Additional frequencies, $E_4(\omega_4)$ with $\omega_4 = 2\omega_1 - \omega_3 < \omega_1$, are generated by propagational four-wave mixing.[28] With $E_i(x,y,z,\omega_i) = A_i(x,y,z,\omega_i)e^{i(k_i z - \omega_i t)}$, self-trapping of $A_1(x,y,z)$ is described in the paraxial and slowly varying envelope approximations by

$$\nabla_T^2 A_1 + 2ik_1 \frac{\partial A_1}{\partial z} = -\alpha_1 A_1. \tag{1}$$

The equations for the interaction between weak fields A_3 and A_4 and for copropagational four-wave mixing are

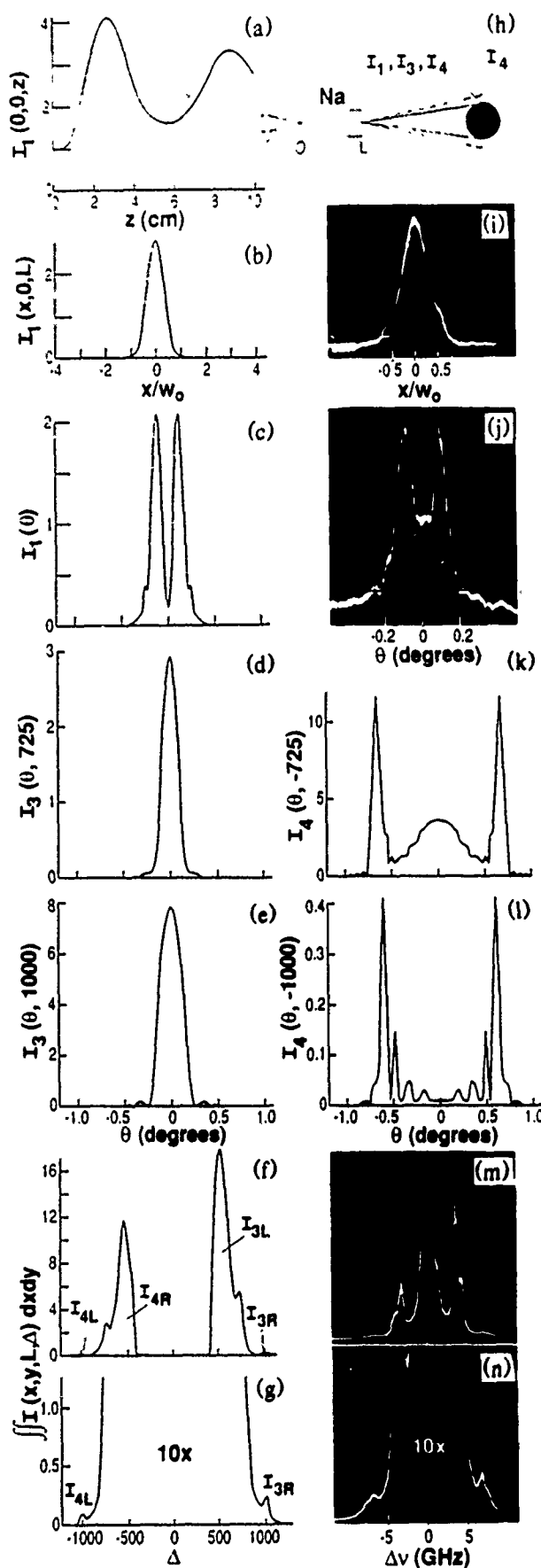$$\nabla_T^2 A_3 + 2ik_3 \frac{\partial A_3}{\partial z} = -\alpha_3 A_3 + \kappa_3 A_4^* + \beta_3 \tag{2}$$

Fig. 4. Physics of cw conical emission, computed and observed. Computations: on-resonance absorption α_0 = 2300 cm^{-1} (before Doppler broadening[29]); frequencies in units of $(2\pi T_1)^{-1}$ are pump detuning of +430 from the low-power atomic resonance and Rabi frequency (maximum value at the entrance of the cell) 2X = 680; T_2 = $2T_1$; input electric field waist w_0 = 72 μm; single resonance with Doppler broadening of ku = 105. Experiment: pump detuning, +3.4 GHz; pump power P = 470 mW; $w_0 \cong$ 76 μm; $^2S_{1/2}$ - $^2P_{3/2}$ D_2 transition with 1.8-GHz ground-state hyperfine transition. Computed pump-beam (a) on-axis intensity, (b) near-field profile (cell-exit waist is 3.75 w_0 in absence of sodium), and (c) far-field profile. Computed far-field profiles at probe detunings Δ from the pump of (d) 725 and (e) 1000. (f) and (g) Computed spectrum of new frequencies generated by Raman-gain amplification of resonance fluorescence along with four-wave mixing. (h) Schematic of setup. Observed pump beam profiles: (i) near-field (cell-exit waist is 3.6 w_0 in absence of sodium); (j) far-field. Computed far-field profiles at (k) Δ = -725; (l) Δ = -1000. (m) and (n) Observed spectrum with (n) magnified 10x.

$$\nabla_T^2 A_4 + 2ik_4 \frac{\partial A_4}{\partial z} = -\alpha_4 A_4 + \kappa_4 A_3^* + \beta_4 \tag{3}$$

where $k_i = 2\pi\omega_i/c$, $\nabla_T^2 = \partial^2/\partial x^2 + \partial^2/\partial y^2$, $\alpha_i(x,y,z)$ and $\kappa_i(x,y,z)$ are functions of $A_1(x,y,z)$ and ω_i and have been integrated over the Doppler velocity distribution.[12,31] The α_i include both absorption/gain and refraction leading to self-trapping of A_1 and transverse evolution of A_3 and A_4. The κ_i describe the four-wave mixing that couples $A_3(\omega_3)$ and $A_4(\omega_4 = 2\omega_1 - \omega_3)$ as they propagate together through the cell. The transverse dependence (through $A_1[x,y,z]$) of the resonance fluorescence β_i from moving atoms is calculated for each frequency and each x,y,z using plasma dispersion functions.[32] Its phase is chosen arbitrarily between 0 and 2π by a random-number generator at each x,y,z. Equations (1)-(3) are computed on a CRAY using fast-Fourier-transform techniques,[33] with the spectrum of Fig. 4(f) requiring $\cong$ 2 CPU hours.

2.4 Results of Numerical Computations

The computed quasi self-trapping of A_1 is depicted in Fig. 4(a,b and c), and the good agreement with the experimental cell-exit and far-field profiles (Fig. 4[i and j]) indicate correct A_1 modeling (first done here with the inclusion of the longitudinal motion of the atoms). One finds that good conical emission occurs even though A_1 is only quasi-trapped,[27] i.e., its diameter alternately contracts and expands as it propagates. Correct modeling of A_1 is essential since its magnitude determines the strengths of α_i and κ_i, and its phase determines the direction of energy transfer between A_3 and A_4 at each x,y,z. One finds both from the measurements and the computations that $A_3(\omega_3)$ never goes into a cone regardless of ω_3; this property is shown in Fig. 4(d and e) for two particular frequencies. In contrast, $A_4(\omega_4)$ forms a well-defined cone at particular values of ω_4 as computed in Fig. 4(k and l) and photographed in Fig. 5(c). The computed spectrum of the new fields is shown in Fig. 4(f and g) and the experimental spectrum in Fig. 4(m and n). Fig. 5(a) shows I_{4L} and I_{3R} spectral peaks; blocking the cone (Fig. 5[b]) largely eliminates I_{4L} while hardly affecting I_{3R}. Reducing the power (Fig. 6) gives a distinctly different far-field profile, but the cone is still present and the spectrum is similar as well.

2.5 Physics of Conical Emission

From the excellent qualitative agreement[34] between computations and experimental observations one understands the *physics of cw conical emission* as follows: self-trapping of A_1, probe generation by resonance fluorescence, Raman-gain amplification of this
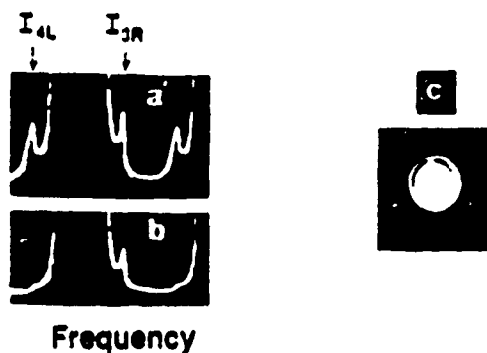
Fig. 5. I_{4L} and I_{3R} spectra with the cone (a) unblocked and (b) blocked, showing that almost all of I_{4L} goes into the cone. (c) Photograph of cone with the $\cong$ 100× more intense center overexposed.

probe producing $A_3(\omega_3)$, four-wave mixing between $A_1(\omega_1)$ and $A_3(\omega_3)$ generating $A_4(\omega_4$ = $2\omega_1 - \omega_3)$ and transfering energy back and forth between A_3 and A_4, division of A_4 into A_{4L} and A_{4R} by optical-Stark-shifted absorption, division of A_3 into A_{3L} and A_{3R} by four-wave-mixing coupling, and formation of the cone from A_{4L} (and sometimes from the low-energy shoulder of A_{4R}) by propagation through the spatially dependent index of refraction Im $\alpha_4(x,y,z)$ prepared by $A_1(x,y,z)$. The physics of pulsed conical emission is, no doubt, the same except that additional frequency-generation mechanisms may c. tribute.

2.6 Cone Angle: Not Determined by Plane-Wave Phase Matching

Some of the cone frequencies also appear in the center of the far-field profile, as computed in Fig. 4(k) and observed in the laboratory by examining the spatial profile of the light through the Fabry-Perot interferometer. Figure 6 reveals the excellent qualitative agreement achieved for an input power of 410 mW, which is slightly lower than the 470-mW input power corresponding to Fig. 4. Fig. 7(a and b) further illustrates that certain frequencies can occur in the cone and in the center, ruling out phase matching as the determinant of the cone angle, unlike many other cones, e.g., two-wavelength conical emission.[35] In addition, the fact that A_1 may be focusing and diffracting as it propagates (see Fig. 4[a]), implies that $\vec{K}_1$ depends on x, y, and z. Unlike plane-wave treatments, phase matching does not need to be imposed externally because the interference between the fields is taken care of automatically in Eqs. (2) and (3), and the transverse degrees of freedom allow phase matching to occur naturally. If

one calculates the plane-wave spectrum (without ∇_T^2), one must arbitrarily impose nearly zero phase mismatch to obtain a similar spectrum.[31]

2.7 Another Example

Reducing the input power to 360 mW changes $I_1(\theta)$ to a single spike on a low pedestal and the frequency spectrum is similar to Fig. 6(b and c) with reduced shoulders on I_{4R} and I_{3L}. In the 160 to 180 mW range, both the computations and data show a cone from I_{4L} with sharp boundaries that expand as the power is reduced; the spectrum shows no I_{3R} peak and I_{4L} is much weaker than for Figs. 4 and 6.

Fig. 6. Physics of conical emission, as in Fig. 4 except 2X = 580 and P = 410 mW. Computed (a) pump-beam far-field profile and (b) and (c) spectrum. Observed (d) far-field profile (peak here is 1.6x larger than the peaks in Fig. 4[j]) and (e) and (f) spectrum with (f) magnified 20x.

Fig. 7.   Computed I_4 far-field profiles (same conditions as Fig. 6) showing that the ratio of cone power to core power increases with Δ = (a) -625, (b) -650, (c) -700, and (d) -900.   This qualitative behavior is observed experimentally.

2.8 Relation to Previous Work

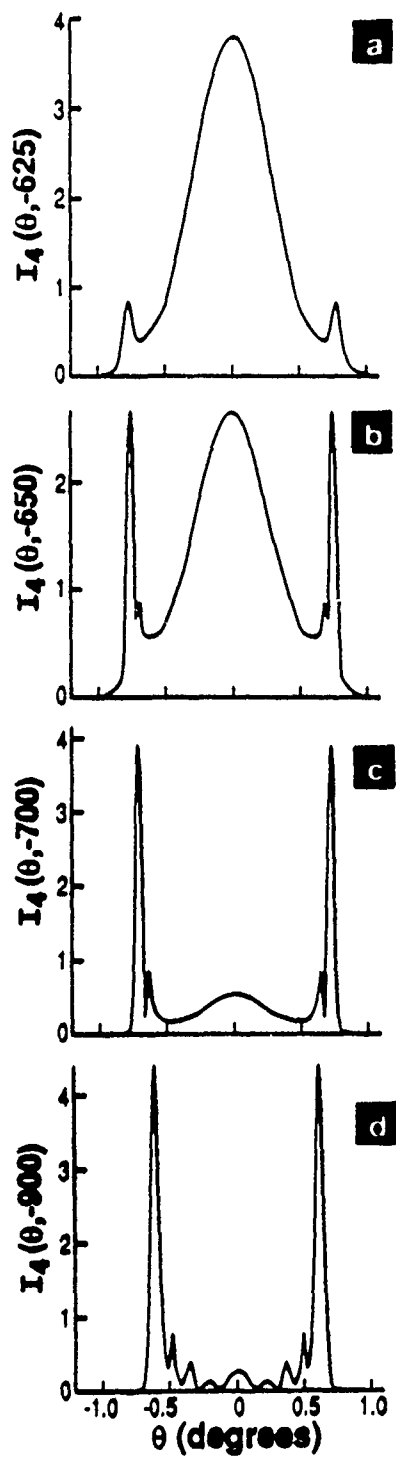We now discuss our work in relation to previous work. Tam[36] observed a very similar cw conical emission arising from amplification of other laser modes. Boyd and Harter[23] computed the copropagation of A_3 and A_4; they did not, however, compute the self-trapping of A_1 or include Doppler broadening, but most importantly, they did not compute the formation of the cone (i.e., they did not include ∇_T^2). Chauchard and Meyer describe but do not compute the refraction due to $A_1(x,y,z)$.[37] Gruneisen et al.[13] have measured and computed probe gain/absorption including Doppler broadening and the Raman gain essential to cw conical emission, but because they use a small angle between A_1 and their probe, A_p, the four-wave mixing at $2\omega_1 - \omega_p$ is emitted at the complementary angle[31] and, therefore, they did not study the Doppler-broadened copropagation of A_3 and A_4. Shevy and Rosenbluh[25] have taken the best spectra of pulsed conical emission, observing the division of A_4 into A_{4L} and A_{4R} and cones from both; but they attribute the cones to two different mechanisms. At high powers, we sometimes simultaneously see a cone from A_{4L} and a larger cone from the left shoulder of A_{4R}; we compute that both have the same origin and that A_{4R} has a larger cone angle than A_{4L} (compare Fig. 7[b and d]). When the optical-Stark shift is small, any A_{4R} that escapes the filament is absorbed by unshifted sodium atoms and only A_{4L} forms a cone. Crenshaw and Cantrell[24] have computed (with ∇_T^2) the propagation of a pulse under self-induced transparency conditions, but the 140 CPU hours required for one run prevented computations for parameters of previous pulsed conical emission experiments. Cw conical emission studied here, even though necessitating the inclusion of Doppler broadening, avoids the formidable time-dependent problem of pulsed conical emission. Our approach is that of pump/probe spectroscopy or instability analyses in which the new fields, A_3 and A_4, are kept weak so that they do not affect A_1 or cause nonlinear effects themselves. Even with cw powers, we have been able to violate this assumption, generating new frequencies at $2\omega_4 - \omega_1$, etc., but that unessential complication was avoided by keeping the sodium density sufficiently low.

2.9 Summary

We have shown that cw conical emission is a spatio-temporal instability in which the cone is formed by pump-induced radially dependent refraction of new frequencies close to the Stark-shifted resonance. Previous treatments have speculated about the physics of cone generations, but we have the first computations in excellent agreement with extensive measurements of the frequency spectra and spatial profiles.

3. Kaleidoscopic Spatial Instability

3.1 Introduction

Recently there has been increased emphasis on spatial instabilities, mostly in cavities.[38,39]   Here we present a spatial instability, with transverse feedback but free from longitudinal feedback, in which a beam propagating in one direction in a self-focusing medium breaks up into more and more filaments as the input power is increased. *These cell-exit (near-field) patterns are stable,* even though they may jitter a little, and *are highly reproducible, showing that they are seeded by phase variations across the input profile and not by random fluctuations.*[40]   In fact, our first numerical simulations used a perfect Gaussian input profile with random fluctuations (small-scale self-focusing approach); those output patterns exhibited at most two or three filaments and fluctuated from run to run in disagreement with experiment. Then we discovered that by adding to our computations the small inherent departures from ideality of our experimental input profile, we were able to reproduce the experimental patterns and bifurcation routes. Consequently, even larger *aberrations were intentionally introduced that were easier to quantify and that enhanced the complexity of the patterns* (as many as eleven spots). Excellent agreement is shown below between numerical simulations and experiments for pattern bifurcations as a function of intensity or detuning with a simple input aberration or shift of the input beam waist. The input aberration or curvature introduces some wave-vector selectivity, just as cavity modes introduce frequency selectivity for temporal instabilities.   The instability of this phenomenon is emphasized by the slowness (on the order of one second) with which the reproducible pattern is regained after the beam is momentarily interrupted.   Often the output pattern searches, going through patterns less complex and sometimes even more complex than the steady-state pattern.

3.2 Experimental Apparatus

The ≈ 800 mW single-mode output power of a dye laser is collimated and brought to a waist at the cell entrance with a maximum of 500 mW reaching the sodium in a 10-cm-long evacuated quartz cell.   The laser beam is vertically linearly polarized and always travels horizontally. The cell-exit profile is imaged onto a CCD camera, recorded on video tape, and then digitized into a 256×256 array of intensity values.   A Fabry-Perot interferometer (flat mirrors with R ≈ 0.98, finesse of 100, 7.5 GHz free spectral range) was used to study the frequency spectrum of the output beam after recollimating the beam. The detuning $\Delta\nu$ of the laser frequency to the high-frequency side of the D_2

resonance of sodium is measured with Lamb-dip spectroscopy, with zero defined as the midpoint between the two hyperfine transitions. Since any type of inhomogeneity or aberration in the input beam can cause beam filamentation,[41] great care was taken to spatially filter the beam, to carefully clean and align the input optics, and to choose a spot on the cell window with minimal aberration.

3.3 Input-Beam Astigmatism

The first intentionally introduced aberration was *astigmatism induced by using two cylindrical lenses* of focal length 21 cm. The y waist was at the input cell window, while the position of the x waist (in the absence of sodium) was varied inside the sodium cell. Figure 8 shows a bifurcation route, with the x waist 3 cm inside the sodium cell, in excellent agreement with our computer simulations.

The propagation and pattern formation of the input laser beam E_l is computed in the paraxial and slowly varying envelope approximations:

$$\nabla^2_T A_l + 2ik_l \frac{\partial A_l}{\partial z} = -\alpha_l A_l \ . \tag{1}$$

where $E_l(x,y,z,\omega_l) = A_l(x,y,z,\omega_l) \exp[i(k_l z - \omega_l t)]$, $k_l = 2\pi\omega_l/c$, $\nabla^2_T = \partial^2/(\partial x^2) + \partial^2/(\partial y^2)$. The coefficient $\alpha_l(x,y,z)$ is a function[42] of A_l and ω_l and has been integrated over the Doppler velocity distribution; it includes both nonlinear absorption/gain and refraction, leading to the pattern formation. Equation (1) is solved on a CRAY computer using fast-Fourier-transform techniques[27,33,43] with each cell propagation taking approximately 3 CPU minutes. To model the intentionally introduced astigmatism, a phase term was added to the input wavefront at the cell entrance such that the slowly varying input field envelope has the following form:

$$A_l(x,y,0,\omega_l) = A'_l(0,\omega_l) \exp \frac{-ik_l}{2} \left[\frac{x^2}{q_h} + \frac{y^2}{q_v} \right] \tag{4}$$

where $q_v = R_v + i\pi w_o^2/\lambda$, $q_h = R_h + i\pi w_o^2/\lambda$, λ is the input wavelength, and $R_v(R_h)$ is the vertical (horizontal) radius of curvature at the cell entrance window. Here, with $R_v = \infty$ and $R_h = -3.08$ cm, the phase difference between $x = 0$ and $x = w_o = 52 \ \mu$m is $\cong \lambda/13$.

This astigmatic bifurcation sequence is more complicated as one gets closer to resonance and increases the astigmatism (increases the separation between the two orthogonal foci) for a given sodium density. In this case, the bifurcation sequence can
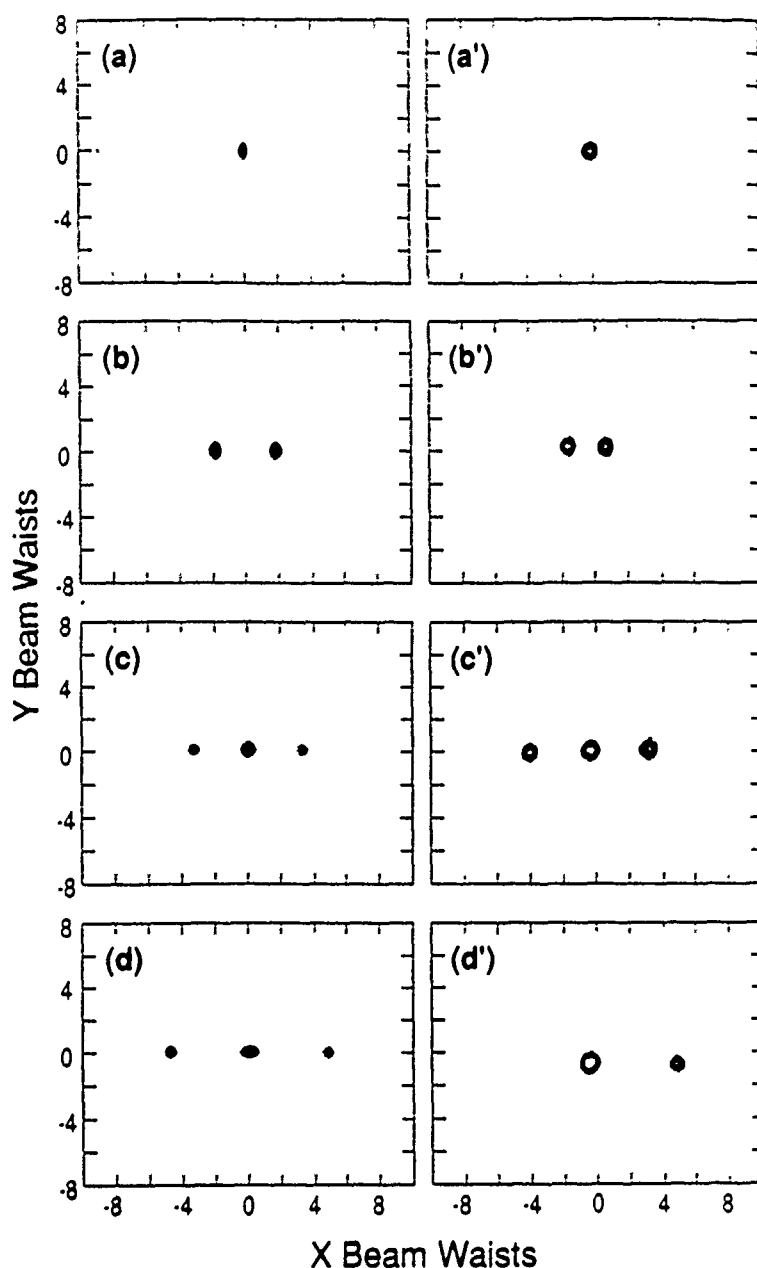
Fig. 8.   Cell-exit profiles for a power bifurcation sequence with astigmatism applied to the input laser beam.   Computational patterns (a-d):   on-resonance absorption α_o = 24000 cm⁻¹ (before Doppler broadening [Ref. 12]); frequencies in units of $1/(2\pi T_1)$ = 10 MHz are pump detuning of Δ = +430 from the low-power atomic resonance and Rabi frequency (maximum value at the entrance of the cell) 2x ranging from 400 (a) to 770 (d); T_2 = $2T_1$; single resonance with Doppler broadening of ku = 105.   Corresponding experimental patterns (a' - d'):   pump detuning δv = +3.4 GHz; unsaturated transmission T = 0.36 at +3.4 GHz; input laser power P ranging from 130 mW (a') to 480 mW (d'); $^2S_{1/2}$ - $^2P_{3/2}$ D_2 transition with 1.8 GHz ground-state hyperfine transition; contour threshold, 34 W/cm² and contour interval, 11.3 W/cm².

be 1 spot → 3 spots → 2 spots → 3 spots and more complicated. In general, as the laser pump power is increased, the number of spots and their spatial separation increases, but both the computer simulations and the experiment show that the filaments can spatially contract and decrease in number for certain ranges of increasing power (usually for 10 mW - 20 mW increments) before beginning to spatially expand again and increase in number. This power periodicity in the spatial patterns may arise from the oscillations in beam diameter accompanying quasi-trapping of the pump beam.[27]

Figure 9 shows the bifurcation sequence as the laser pump detuning is increased from -0.7 to 7 GHz. The x waist is 8 cm inside the sodium cell (R_h = -8.01) and the laser power is 200 mW. When the detuning is larger than 4 GHz, the bifurcation process begins what we call "the kaleidoscope sequence" where the patterns become quite complicated, perhaps approaching spatial chaos. The computational patterns show good qualitative agreement with the experimental patterns.[44]

3.4 Input-Beam Convergence

The other perturbation was an *input-beam convergence* (phase $\sim r^2$), introduced onto the wavefront by changing the collimation of the light reaching the 30-cm focusing lens. Figure 10(a'-d') shows the experimental bifurcation sequence. Since the input-beam curvature is circularly symmetric, we attribute the slightly non-circular symmetry of the data to a small amount of aberration persisting through the spatial filter. Comparing our experimental spatial patterns with known optical spot diagrams[45] formed by ray tracing a uniform grid of rays through an optical system suffering from various degrees of the Seidel aberrations, we concluded that the primary residual aberrations were astigmatism and coma. These aberrations are modeled by two asymmetric phase terms and a focus phase term:

$$A_1(x,y,0,\omega_1) = A'_1(0,\omega_1)\exp -\left[\left[\frac{1}{w^2} + \frac{i\pi}{\lambda R}\right]r^2 + 2\pi\left[\frac{W_{22}y^2}{w^2} + \frac{W_{13}r^2y}{w^3}\right]\right] \tag{5}$$

where w is the beam radius at the cell entrance, λ is the input field wavelength, R is the radius of curvature at the cell entrance, W_{22} is the astigmatic coefficient, W_{13} is the comatic coefficient, and $r^2 = x^2+y^2$. $W_{22} = 5\times10^{-4}$ and $W_{13} = 5\times10^{-5}$ were used in Fig. 10(a-d) to match the data of Fig. 10(a'-d'). The phase difference between r = 0 and r = w is $\cong \lambda/7$ for the focus term, while it is only $\lambda/2000$ for astigmatism and $\lambda/20000$ for coma (making it almost impossible to measure them directly).

Fig. 9.   Cell-exit profiles for a pump detuning bifurcation sequence with astigmatism applied to the input laser beam.   Computational patterns (a-d): α_0 = 24000 cm^{-1}; 2X = 540; Δ ranging from +190 (a) to +1500 (d); T_2 = $2T_1$; ku = 105.   Corresponding experimental patterns (a' - d'): P = 200 mW; δv ranging from -0.7 GHz (a') to 7.2 GHz (d'); T = 0.36 at +3.4 GHz.   Contour threshold, 13.6 W/cm^2, and contour interval, 5.67 W/cm^2 for (a', c', d'), while contour threshold, 34 W/cm^2 and contour interval, 11.3 W/cm^2 for (b').
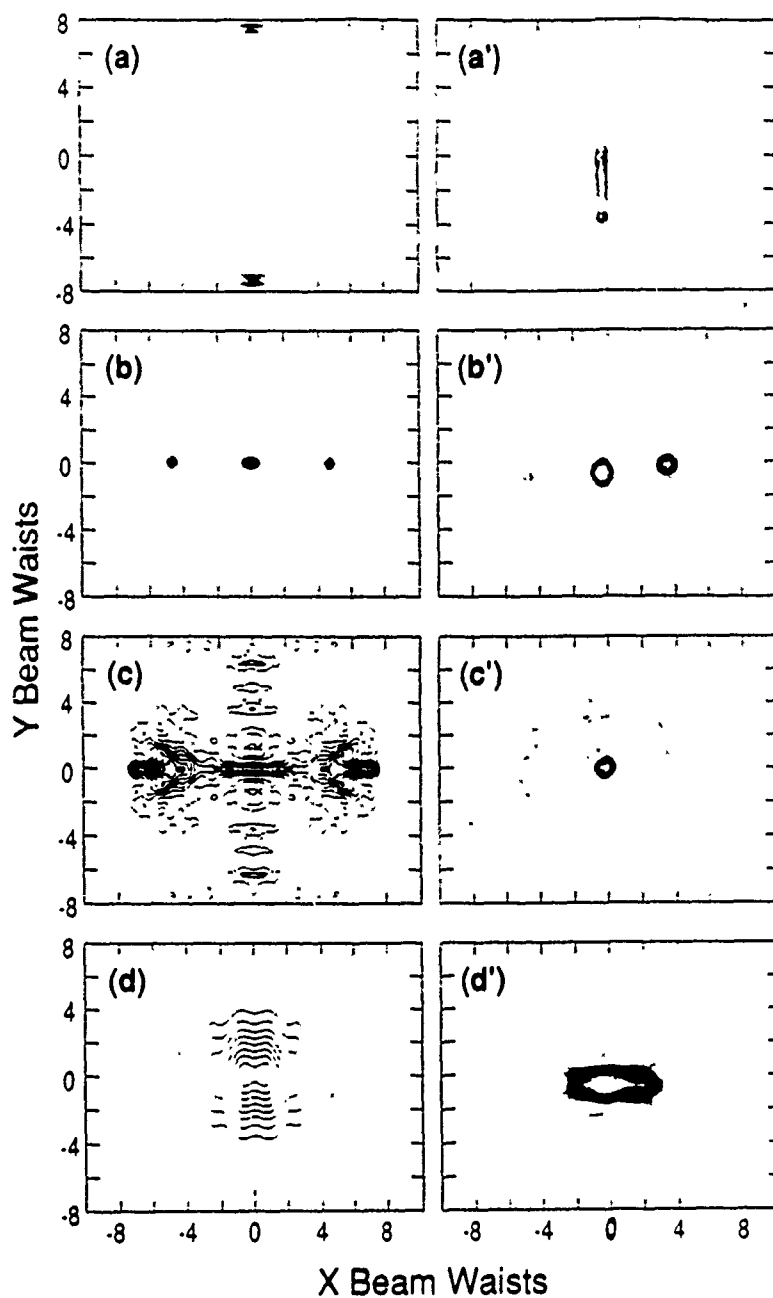
Fig. 10. Cell-exit profiles for a power bifurcation sequence with focus added to the input laser beam. Computational patterns (a - d): $\alpha_0 L = 24000$ cm^{-1}; $\Delta = +290$; 2X ranging from 200 (a) to 580 (e); $T_2 = 2T_1$; ku = 105. Corresponding experimental patterns (a' - d'): $\delta v = 2$ GHz; P ranging from 30 mW (a') to 220 mW (d'); $T = 0.0$ at +2.0 GHz and 0.36 at +3.4 GHz; contouring same as in Fig. 8. $R = -3.5$ cm and $w = 76.3$ μm for both the experimental and computational patterns.

3.5 New Frequencies

This spatial instability is accompanied by the generation of one or more new frequencies resulting in temporal instabilities as well. The new frequencies are explained as arising from the Raman-gain portion of the intense-field, Doppler-broadened sodium absorption/gain profile.[7,11,12,29] This inseparability of spatial and temporal instabilities arises from the fact that the saturation of the nonlinearity essential to avoiding catastrophic self focusing results in a field above the threshold for Raman gain. The spectrum of each of the strong filaments contains the input pump frequency and new Raman-gain frequencies, but the spatial pattern is determined primarily by light at the pump frequency if pump depletion is avoided. Significant pump depletion occurs for a small range (30 mW - 40 mW) of input pump power, such that the newly generated fields are comparable and even larger than the cell-exit pump field. At larger input powers, however, the pump intensity again dominates. Thus, one must be very careful in modeling the pattern formation using a single-frequency undepleted-pump model. Pump depletion was avoided for all of the data used here for comparisons with computations. The spectrum of a single filament sometimes consists of two regions; from their dependence upon the intensity and detuning, we believe this is the first observation of the double-peaked Raman gain predicted by Khitrova et al.[11,12]

3.6 Summary

We have observed spatial bifurcation sequences as interesting and complicated as temporal bifurcation sequences observed in other optical systems. They are explained as spatial instabilities seeded by intentionally introduced aberrations. In temporal instabilities, the ω gain curve determines which frequencies in the fluctuations will be amplified; selective feedback or an injected signal is used to encourage particular directions or frequencies. In spatial instabilities, the k gain curve determines which wave vectors in the fluctuations will be amplified; input-wavefront-phase encoding is used to accentuate particular wave vectors. Then, with fixed-phase encoding, complicated bifurcations result as a function of intensity or detuning. Relevant to all studies of beam propagation and filamentation in nonlinear atomic vapor systems is our evidence that new frequencies from Raman gain usually accompany these processes; they must either be included in the modeling or kept negligibly small in the experiments, as here.

REFERENCES

1. Y. Silberberg and I. Bar-Joseph, Phys. Rev. Lett. **48**, 1541 (1982).

2. I. Bar-Joseph and Y. Silberberg, Opt. Commun. **48**, 53 (1983).

3. Y. Silberberg and I. Bar-Joseph, J. Opt. Sci. Am. B **1**, 662 (1984).

4. I. Bar-Joseph and Y. Silberberg, Phys. Rev. A **36**, 1731 (1987).

5. Of course, several authors have recognized that self-oscillations can arise from the amplification of sidebands: S. L. McCall, Phys. Rev. A **9**, 1515 (1974); A. C. Tam, Phys. Rev. A **19**, 1971 (1979); S. T. Hendow and M. Sargent, III, Opt. Commun. **40**, 485 (1982); L. W. Hillman, R. W. Boyd, and C. R. Stroud, Jr., Opt. Lett. **7**, 426 (1982); W. J. Firth, E. M. Wright, and E. J. D. Cummins, in *Optical Bistability 2*, edited by C. M. Bowden, H. M. Gibbs, and S. L. McCall, (Plenum, New York, 1983), p. 111. This Raman gain is the origin of the self-pulsing predicted by R. Bonifacio and L. A. Lugiato, Lett. Nuovo Cimento **21**, 510 (1978), and seen by B. Segard and B. Macke, Phys. Rev. Lett. **60**, 412 (1988).

6. P. R. Berman, G. Khitrova, and J. F. Lam, in *Spectral Line Shapes*, edited by F. Rostas (de Gruyter, Berlin, 1985), Vol. 3, p. 337; G. Grynberg, E. Le Bihan, and M. Pinard, J. Phys. (Paris) **47**, 1321 (1986).

7. S. Haroche and F. Hartman, Phys. Rev. A **6**, 1280 (1972).

8. B. R. Mollow, Phys. Rev. A **5**, 2217 (1972).

9. F. Y. Wu, S. Ezekiel, M. Ducloy, and B. R. Mollow, Phys. Rev. Lett. **38**, 1077 (1977). For a full discussion, see M. D. Levenson, *Introduction to Nonlinear Laser Spectroscopy* (Academic, New York, 1982), Sect. 3.1.

10. R. W. Boyd, M. G. Raymer, P. Narum, and D. J. Harter, Phys. Rev. A **24**, 411 (1981).

11. G. Khitrova, Ph.D. dissertation, New York University, 1986, unpublished. Eqs. (4.1) - (4.6) on pp. 54 - 57 were used to generate Figs. 1 and 3(b); ν_R here is $2X/2\pi T_1$ there. Only a single two-level transition is assumed, but inclusion of both hyperfine components affects the gains very little for negative detuning.

12. G. Khitrova, P. Berman, and M. Sargent, III, J. Opt. Soc. Am. B **5**, 160 (1988).

13. Pump-probe measurements of the Doppler-broadened gain profile are reported in M. T. Gruneisen, K. R. MacDonald, and R. W. Boyd, J. Opt. Soc. Am. B **5**, 123 (1988).

14. S. G. Odulov, S. S. Slydsarenko, and M. S. Soskin, Kvantovaya Elektron. (Moscow) **11**, 869 (1984) (Sov. J. Quantum Electron. **14**, 589 [1984]).

15. D. Grandclement, G. Grynberg, and M. Pinard, Phys. Rev. Lett. **59**, 40, 44 (1987).

16. A pressure-induced extra resonance was observed in four-wave mixing by Y. Prior, A. R. Bogdan, M. Dagenais, and N. Bloembergen, Phys. Rev. Lett. **46**, 111 (1981). In contrast, this zero-pressure Rayleigh-gain lasing uses two-wave mixing.

17. H. Rajbenbach and J. P. Huignard, Opt. Lett. **10**, 137 (1985).

18. A. E. Kaplan and P. Meystre, Opt. Commun. **40**, 229 (1982).

19. A. E. Gaeta, R. W. Boyd, J. R. Ackerhalt, and P. ⁻ᵛ Milonni, Phys. Rev. Lett. **58**, 2431 (1987); A. E. Kaplan and C. T. Law, IE'   Quantum Electron. **21**, 1529 (1985).

20. M. Ducloy and D. Bloch, Phys. Rev. A **30**, 3107 (1984). for further discussion and experimental confirmation, see P. R. Berman, D. G. Steel, G. Khitrova, and J. Liu, Phys. Rev. A **38**, 252 (1988).

21. B. R. Mollow, Phys. Rev. A **7**, 1319 (1973).

22. Gain at $\nu_L \pm \nu_{RE}$ was reported in the stationary-atom limit by D. J. Harter, P. Narum, M. G. Raymer, and R. W. Boyd, Phys. Rev. Lett. **46**, 1192 (1981).

23. D. Grischkowsky, Phys. Rev. Lett. **24**, 866 (1970).

24. M. E. Crenshaw and C. D. Cantrell, Phys. Rev. A **39**, 126 (1989) and Opt. Lett. **13**, 386 (1988).

25. Y. Shevy and M. Rosenbluh, J. Opt. Soc. Am. B **5**, 116 (1988) and Opt. Lett. **4**, 257 (1987).

26. J. E. Bjorkholm and A. Ashkin, Phys. Rev. Lett. **32**, 129 (1974).

27. M. L. LeBerre, E. Ressayre, A. Tallet, and F. P. Mattar, J. Opt. Soc. Am. B **2**, 956 (1985).

28. D. J. Harter and R. W. Boyd, Phys. Rev. A **29**, 739 (1984); Opt. Lett. **7**, 491 (1982); IEEE J. Quantum Electron. **QE-16**, 1126 (1980). R. W. Boyd, M. G. Raymer, P. Narum, and D. J. Harter, Phys. Rev. A **24**, 411 (1981).

29. G. Khitrova, J. F. Valley, and H. M. Gibbs, Phys. Rev. Lett. **60**, 1126 (1988).

30. D. A. Holm, M. Sargent, III, and L. M. Hoffer, Phys. Rev. A **32**, 963 (1985).

31. J. F. Valley, Ph.D. dissertation, Optical Sciences Center, University of Arizona (1989).

32. G. Khitrova, Xu Jiajin and J. F. Valley, unpublished.

33. J. V. Moloney, M. R. Belic, and H. M. Gibbs, Opt. Commun. **41**, 379 (1982) and references therein.

34. Various approximations prevent exact quantitative agreement between the data and computations. The hyperfine structures of the $^2S_{1/2}$ ground state and $^2P_{3/2}$ excited state and optical pumping (which would require inclusion of transverse motion of the atoms in and out of the beam) were neglected. Instead the sodium was treated as a single Doppler-broadened two-level transition. Within that approximation, the values of the detuning and Rabi frequency in GHz are obtained by dividing the normalized values in the figure captions by 100. One finds that the computed separation between peaks or absorption exceeds that observed by 30% to 40%. The measured low-power off-resonance absorption at the pump wavelength was 15% and the computation value was 7% for the conditions of Fig. 1. The measured cone angles usually exceed the computed angles by 20%. We conclude, within the approximations of our model, that the quantitative agreement is remarkably good and that all of the qualitative features of the experimental data (dozens of recorded profiles and spectra in both 2-cm and 10-cm cells) also appear in the computations (about ten with uniform seed and ten with resonance-fluorescence seed).

35. J. Krasinski, D. J. Gauthier, M. S. Malcuit, and R. W. Boyd, Opt. Commun. **54**, 241 (1985).

36. A. C. Tam, Phys. Rev. A **19**, 1971 (1979).

37. E. A. Chauchard and Y. H. Meyer, Opt. Commun. **52**, 141 (1984).

38. Special Issue on "Transverse Effects in Nonlinear-Optical Systems," N. Abraham and W. Firth, eds., J. Opt. Soc. Am. B **7**, 948-1157 and 1264-1373 (1990).

39. Proceedings of "Nonlinear Dynamics in Optical Systems," June 4-8, 1990, Afton, OK (Optical Society of America).

40. This spatial instability is different from the far-field spots of G. Grynberg, Opt. Commun. **66**, 321 (1988) that require a standing wave.

41. A. J. Campillo, S. L. Shapiro, and B. R. Suydam, Appl. Phys. Lett. **23**, 628 (1973).

42. Section 2.6 of M. D. Levenson, *Introduction to Nonlinear Laser Spectroscopy* (Academic Press, New York, 1982). Our expressions in terms of plasma dispersion functions are given in Ref. 31.

43. J. F. Valley, G. Khitrova, H. M. Gibbs, J. W. Grantham, and Xu Jiajin, Phys. Rev. Lett. **64**, 2362 (1990).

44. Various approximations prevent exact quantitative correspondence between the experimental and computational detunings. Sodium is treated as a single Doppler-broadened, two-level transition, with a detuning usually corresponding to complete hyperfine optical pumping. We measure the unsaturated transmission at +3.4 GHz and from this value calculate the absorption value used in the computations.

45. Optical spot diagrams are a common output of commercial lens design programs.

NONLINEAR DYNAMICS AND CHAOS IN CAVITY QED

Pierre Meystre

SCIENTIFIC PERSONNEL

P. Meystre	S. Braunstein
T. A. B. Kennedy	C. Haggans
C. M. Savage	A. Guzman
R. Cheng	E. Schumacher
J. Slosser	M. Wilkens

PUBLICATIONS

1. C. M. Savage and D. F. Walls, "Squeezing by parametric oscillation and intracavity four-wave mixing," J. Opt. Soc. Am. B 4, 1514 (1987).

2. T. A. B. Kennedy and S. Swain, "Dressed atom approach to strong-field double resonance fluorescence with laser phase fluctuations," Phys. Rev. A 36, 1747 (1987).

3. T. A. B. Kennedy and D. F. Walls, "Squeezed quantum fluctuations and macroscopic quantum coherence," Phys. Rev. A 37, 152 (1988).

4. C. M. Savage, "Oscillations and quantized second harmonic generation," Phys. Rev. A 37, 158 (1988).

5. P. Meystre and E. M. Wright, "Measurments-induced dynamics of a micromaser," Phys. Rev. A 37, 2524 (1988).

6. C. M. Savage, "Stationary two-level atomic inversion in a quantized cavity field," Phys. Rev. Lett. 60, 1828 (1988).

7. C. M. Savage and H. Carmichael, "Single atom optical bistability," IEEE J. Quant. Electronics (August 1988).

8. J. Javanainen and P. Meystre, "Quantum mechanics," in the 1989 McGraw-Hill Yearbook of Science and Technology.

9. P. Meystre, "Generation and detection of sub-Poissonian fields in a micromaser," in *Squeezed and Non-Classical Light*, P. Tombesi, ed. (Plenum Press, New York, 1989), p. 115.

10. P. Meystre, G. Rempe, and H. Walther, "Very low temperature behavior of a micromaser," Opt. Lett. 13, 1078 (1988).

11. E. M. Wright and P. Meystre, "Collapse and revival in the micromaser Opt. Lett. 14, 177 (1989).

12. P. Meystre and J. J. Slosser, "Destruction of quantum coherence by finite quantum efficiency in a micromaser," Opt. Commun. 70, 103 (1989).

13. J. J. Slosser, P. Meystre, and S. L. Braunstein, "Harmonic oscillator driven by a quantum current," Phys. Rev. Lett. 63, 934 (1989).

14. A. M. Guzman, P. Meystre, and E. M. Wright, "Semiclassical theory of a micromaser," Phys. Rev. A 40, 2471 (1989).

15. P. Meystre, E. Schumacher, and S. Stenholm, "Atomic beam deflection in a quantum field," Opt. Commun. 73, 443 (1989).

16. P. Meystre and J. J. Slosser, "Measurements, dynamics and state preparation in a micromaser," in *Coherence and Quantum Optics VI*, J. H. Eberly, L. Mandel, and E. Wolf, eds. (Plenum, New York, 1990), p. 747.

17. J. J. Slosser and P. Meystre, "Tangent and cotangent states of the electromagnetic field," Phys. Rev. A 41, 3867 (1990).

18. P. Meystre, E. Schumacher, and E. M. Wright, "Quantum Pendellösung in atomic diffraction by a light grating," to be published in *Annalen der Physik*.

19. J. J. Slosser, P. Meystre, and E. M. Wright, "Generation of macroscopic superpositions in a micromaser," Opt. Lett. 4, 233 (1990).

20. E. M. Wright and P. Meystre, "Theory of an atomic interferometer in the Raman-Nath regime," Opt. Commun. 75, 338 (1990).

21. B. W. Shore, P. Meystre, and S. Stenholm, "Is a quantum standing wave composed of two traveling waves?" J. Opt. Soc. Am. B, in press.

22. P. Meystre, J. J. Slosser, and M. Wilkens, "Cat in a cold Niobium box," Opt. Commun. (1990)

23. P. Meystre, "Understanding laser light," Physics World 3(10), 22 (1990).

Conference papers

1. P. Meystre, T. A. B. Kennedy, and E. M. Wright, "The micromaser: from cavity QED to quantum chaos," Invited paper, Adriatico Research Conference on Vacuum in Nonrelativistic Matter-Radiation Systems, Trieste, Italy (1987).

2. P. Meystre, "Single atom quantum mechanics," Invited paper, 18th Winter Colloquium on Quantum Electronics, Snowbird (1988).

3. P. Meystre, "Nonclassical microwave radiation," Invited paper, NATO Advanced Study Workshop on *Squeezed and Nonclassical Light*, Cortina D'Ampezzo, Italy (1988).

4. E. M. Wright and P. Meystre, "Quantum reviavals in micromasers," OSA Annual Meeting, San Jose, CA (1988).

5. J. J. Slosser, T. A. B. Kennedy, and P. Meystre, "Decay of number state superpositions in micromasers," OSA Annual Meeting, San Jose, CA (1988).

6. S. L. Braunstein, P. Meystre, and J. J. Slosser, "New states of the harmonic oscillator," invited paper, 19th Winter Colloquium on Quantum Electronics, Snowbird (1989).

7. P. Meystre, "Measurements, dynamics, and state preparation in a micromaser," invited paper, Sixth Rochester Conference on Coherence and Quantum Optics, Rochester (1989).

8. "Cavity QED," invited lectures, International Summer School on Nonlinear Optics in Solids, Aalberg, Denmark (1989).

9. P. Meystre, "Cavity QED," invited tutorial, OSA Annual Meeting, Orlando, (1989).

10. J. J. Slosser and P. Meystre, "Cotangent states of the electromagnetic field," contributed paper, OSA Annual Meeting, Orlando (1989).

11. P. Meystre, "Atomic diffraction in quantized fields," invited paper, 20th Winter Colloquium on Quantum Electronics, Snowbird (1990).

12. P. Meystre, "Scattering of atoms in optical fields," invited paper, Matter-Wave Interferometry Workshop, Santa Fe (1990).

13. J. J. Slosser and P. Meystre, "Steady state macroscopic superpositions in a micromaser," contributed paper, International Quantum Electronics Conference, Anaheim (1990).

14. E. M. Wright, S. Glasgow, and P. Meystre, "Raman-Nath and Bragg scattering in atomic deflection," contributed paper, International Quantum Electronics Conference, Anaheim (1990).

15. P. Meystre, "A Heisenberg microscope in atom optics," invited paper, International Workshop on The Foundations of Quantum Mechanics, Santa Fe (1990).

RESEARCH SUMMARY

Cavity QED

Cavity quantum electrodynamics is the study of the interaction between few atoms and the (typically single-mode) fields that can be realized in high-Q microwave cavities. Our research addresses aspects of this problem that are relevant not only in traditional quantum optics (coherence, nonclassical fields) but simultaneously make contact with nonlinear dynamics and chaos. We obtained a number of novel and unexpected results that might have considerable impact in quantum electronics applications, while at the same time contribute to a deeper understanding of the transition between quantum mechanical and classical dynamics. In particular, we are now in a position to (1) help design lasers with significantly reduced intensity fluctuations, and (2) shed new light on the elusive problem of the correspondence between classical and quantum physics.

In a nutshell, the key question that we are attempting to answer is, *"under what conditions does a system become classical?"* Clearly, one has to understand this problem to generate, propagate, and detect nonclassical sources of light, but the relevance of this question goes far beyond this simple application.

There is no obvious answer to this question. Intuitively, one would expect that as a system becomes "large" its behavior becomes more classical. Thus, some measure of the *size* of the system should be important. For instance, one might expect a field containing a large number of photons to behave classically. Although this is usually the case, several known instances exist where this is not so (see, e.g., the Jaynes-Cummings problem). This is why this model, and the closely related micromaser, remain exceedingly important test cases for our ideas.

Of more direct relevance perhaps to this question is the role of quantum interferences. One of the most fundamental differences between the quantum and classical worlds is the possibility of interferences between probability amplitudes in the first case. This is translated mathematically by the fact that quantum systems can be in coherent superpositions of states (classical systems are always represented by mixtures). The question, then, is to try to understand why such coherent superpositions do not appear to survive at the macroscopic level. It turns out that dissipation, e.g., due to the unavoidable coupling of the system of the environment, kills such superpositions at a very fast rate. *Dissipation*, then, is another central concept in the quantum/classical correspondence and the study of the decay of coherences in "small" quantum optical systems should teach us a great deal about this aspect of the problem.

A major step was achieved with the discovery of a new class of states of a quantum harmonic oscillator. Specifically, we succeeded in showing that under certain circumstances a simple quantum harmonic oscillator driven by a stream of polarized two-level atoms evolves to unique pure states even if started as a mixed state. The pure states generated in this way are generalizations of the harmonic-oscillator coherent state, and we call them tangent and cotangent states.

It is well known that a quantum simple harmonic oscialltor (HO) at zero temperature, driven by a classical current and subject to dissipation, evolves toward a unique pure state, a coherent state. Dissipation ensures that the initial character of the HO's state is transient and is replaced by that state which balances the gain from the classical current with the losses. In hindsight, the fact that the photon statistics of single-mode lasers far above threshold are nearly Poissonian can be traced back to this property. In contrast, the new class of states were discovered when considering the

more complicated problem of an HO driven by a *quantum* current.

We have performed a number of numerical experiments showing the evolution of the harmonic oscillator mode to these new pure states. Results have demonstrated a large variety of possible steady states, some sub-Poissonian and some with the character of "macroscopic" quantum superpositions. We have also derived the mathematical form of these states from a general factorization argument, and used boundary conditions to select between tangent and cotangent states for given initial conditions. In addition, we have developed a simple graphic construction to determine general properties of the cotangent states. In particular, this construction permits one to readily predict under which conditions cotangent states acquire the character of *"macroscopic" superpositions*. To study the dynamic evolution of the driven oscillator, we have carried out an eigenvalue analysis of the quantum map describing the system. We have introduced a space of "super-vectors" that allow one to describe all physically meaningful density matrices, and numerically found the eignevectors with unit eigenvalues corresponding to steady states of the system. We have further demonstrated the possibility of "period-2" oscillations in the cavity mode dyanamics.

As already stated, the generation of macroscopic quantum superpositions is of considerable importance in the study of the interface between quantum physics and classical physics. While evidence for quantum tunneling has been established, the observation of quantum superpositions is problematic. A major problem is that macroscopic objects are not isolated, but are coupled to their environment, usually leading to rapid destruction of quantum coherences. However, we have found that it is possible for the macroscopic quantum superposition forms of the cotangent states to persist in steady state even for nonzero dissipation, provided the maser operates at very low temperature.

As the ratio between the atomic injection rate R and the harmonic oscillator damping rate γ ($N_{ex} = R/\gamma$) is increased, there is a distinct transition between two final states of completely different nature. For low N_{ex}, the field is nearly in the vacuum state. Above the transition region, however, the von Neumann entropy of the field decreases roughly as $1/N_{ex}$, and the field becomes very close to a cotangent state

$$|c\rangle = \sum_{n=0}^{N} s_n |n\rangle \ . \tag{1}$$

with

$$s_n = -i (a/b) \cot(\sqrt{n}\ \kappa\tau/2)\ s_{n-1} \quad . \tag{2}$$

Here κ is the atom-field dipole coupling constant, τ the atomic transit time through the field mode, and the sum (1) is truncated at the "trapping state" N defined by $\sqrt{N+1}\ \kappa\tau = q\pi$, q integer.

To determine more precisely the nature of the transition, we have studied the logarithm of the Q-function $Q(\alpha) = \langle\alpha|\rho|\alpha\rangle$ of the micromaser field density matrix. This is motivated by noting that, in equilibrium problems, the steady-state density matrix is of the form

$$\rho = \mathcal{N}\ \exp(-V/kT) \quad , \tag{3}$$

where $\mathcal{N}$ is a normalization constant, V is the potential, k is the Boltzmann constant, and T is the temperature. Of course, this expression is not valid for the open system at hand, yet, by analogy, we expect the logarithm of the density matrix to still yield some kind of an effective potential. The specific choice of the Q-function is motivated by the property that, in contrast to other distribution functions, this diagonal expansion of the density matrix on coherent states $Q(\alpha)$ is positive-definite, hence its logarithm is guaranteed to exist.

For a second-order-like phase transition, the effective potential $V = -\ln Q(\alpha)$ would develop its minima above threshold via a pitchfork bifurcation from its minimum below threshold. Our results show unambiguously that this is not the case here: rather, the transition to a macroscopic quantum superposition resembles a first-order phase transition and the system is akin to optically bistable systems. Indeed, for large N_{ex}, the Q-function resembles that of conventional dispersive bistability. There is, however, an essential difference between these two situations: conventional optical bistable systems are in a mixture, rather than a coherent superposition of two quantum states localized at the minima of the effective potential. In contrast, the present situation is characterized by a *coherent* superposition of two such states.

Our present investigations are directed toward detecting these macroscopic superpositions. An excellent test system is a micromaser as developed at the Max-Planck Institute for Quantum Optics in Germany. Simple-minded measurements on the state of the atoms as they exit the cavity are not adequate. Straightforward photon-counting measurements, assuming they can be performed at the wavelengths under consideration, would be just as unsatisfactory; any outcome would put the field in an eigenstate of the

photon number operator, and destroy its off-diagonal elements. Appropriate measurements must be sensitive to the high-order field correlation functions proportional to the off-diagonal elements, ρ_{nm}, and, hopefully, be back-action evading as well. Nonlinear atomic homodyne measurements might offer a way around this difficulty.

de Broglie Interferometry

In the last year of this JSOP program, we have initiated a new direction of research in de Broglie optics. In addition to cavity QED, the manipulation of atomic trajectories by light fields represents one of the most exciting recent developments in laser spectroscopy. Here, one exploits the fact that, every time an atom interchanges energy with a near-resonant radiation field, the momentum of the absorbed light must be compensated for by the mechanical motion of the atom. Phenomena such as atomic trapping and cooling, and state-selective atomic reflection by light fields, can be studied. Several types of atomic mirrors, lenses and gratings could be utilized. Indeed, all of the basic elements needed to perform "de Broglie optics" are envisioned. In addition to their potential applications, these mechanical manifestations of light-matter interactions comprise a fascinating area of fundamental research, combining the internal quantum structure of atomic particles with their translational degrees of freedom in an essential way.

In de Broglie optics, it is usually sufficient to describe the strong driving fields classically, while spontaneous emission can be treated as a stochastic process. In cavity QED, on the other hand, the quantum nature of the intracavity modes is essential to the research.

We have initiated a study that combines these two areas of research, investigating to what extent the quantum nature of light modifies its mechanical effects on atoms. Such questions are relevant, for example, in connection with state-selective reflection, where it is important to determine if atoms initially in a coherent superpostition of two states are left in a coherent superposition or in a mixture after reflection. A proper quantum mechanical treatment of the atom-field interaction if required to answer this question.

We have begun a detailed theoretical study of the diffraction of an atom by light in the semiclassical regime, as well as for quantum fields. Both the Raman-Nath and the Bragg regime of diffraction are considered. In addition, our approach permits a treatment of classical fluctuations and noise, and provides a least a partial explanation of the experimental results of Pritchard et al.

To apply our research we have initiated a detailed numerical modeling of an atomic

interferometer.   The interference of atoms in optical fields was first proposed by Dubetsky et al., who considered an interferometer consisting of two separated standing-wave fields.   Atomic deflection in the first beam arises from the optical Kapitza-Dirac effect, that is, from the scattering of atoms off the periodic structure provided by a standing-wave laser field.   The atomic beam then is recombined in a second standing wave, leading to atomic interferences downstream from the field.   An accurate description of the interferometer requires consideration of the combined effects of all scattering processes and of the transverse profiles of the atomic beam and standing waves.

Further work on atom optics has developed in several directions, and in particular, our work on atom scattering off quantized fields has helped shed new light on the quantum measurement process.

Both standing and traveling waves are routinely used as basis fields in creating a quantum theory of electrodynamics. The two different descriptions of fields give the same predictions of single-photon transition rates, such as spontaneous emission and photoionization.   However, in the quantum regime (of small photon numbers) atoms are scattered differently by a true standing wave than by a superposition of two counterpropagating waves of equal amplitudes and opposite directions.   No such difference occurs classically.

The system we considered consists of a collimated stream of atoms that travel across the standing wave pattern.   With passing time the field induces absorption and emission of energy.   The emission and absorption of radiation not only changes the atomic excitation energy, it alters the momentum of the atomic center of mass.   Atoms undergo two types of momentum change as they cross a resonant standing wave.   First, their transverse momentum spreads.   Second, if the atoms cross the field at an angle, they undergo Bragg scattering from the periodic structure provided by the wave. Classically, this behavior can be understood in terms of traveling waves: the atom catalyzes the transfer of momentum from one traveling wave to the other, thereby changing its own transverse momentum.   In the quantum regime, however, there is an essential difference between scattering by two running waves and scattering by a standing wave.   With running waves, we can know in principle which of the two waves has exchanged a unit of momentum with the atom.   In contrast, a standing wave is an inseparable quantum unit whose average momentum remains zero at all times. This unity is imposed by the fixed mirrors that establish the standing wave.   These act as infinite sinks of momentum.   The reasons for this difference are deeply rooted in the

foundations of field quantization. Quantum mechanics forbids one *even in principle* from determining, via a field measurement, from which traveling wave the atom picks up its momentum.

Mathematically, the difference between a single-mode standing wave and the equivalent pair of running waves manifests itself only in the coupling matrix elements of the atom-field equations of motion. These differences follow directly from the quantization procedure for the normal modes of the electromagnetic field. A choice of eigenmodes embodies a decision about the character of the state we create by the bosonic creation operator $a^\dagger$. Our choice determines the energy and momentum carried by the field increments, the photons. Different choices make energy and momentum conservation manifest themselves differently. Superficially, the change of basis states merely introduces a linear transformation of the creation operator. When the system is coupled to a set of atoms that can probe the structure of the modes, however, momentum conservation allows us to infer the physical boundary conditions of the electromagnetic field. The momentum increments acquired by the atoms must match those available from the field. Two independently imposed traveling waves offer a limited amount of momentum, whereas the mirrors that establish and maintain a stable standing-wave structure serve as inexhaustible momentum sources and sinks.

A similar interpretation is available in a semiclassical description of the field-atom interaction. If we consider properly the energy-momentum exchange we can selectively absorb one traveling wave component, for example, by Doppler-shifting the atomic transition into resonance with it. If the two waves are generated by reflection in a standing-wave cavity, however, the change of field amplitude will be distributed over both waves within a few cavity round-trip times. This re-establishes the standing-wave pattern. The atomic behavior, therefore, can in this case also be described as a scattering process from a rigid lattice.

ORIGIN AND APPLICATION OF
FOUR-WAVE MIXING IN SEMICONDUCTORS

S. W. Koch, N. Peyghambarian, and E. M. Wright

PUBLICATIONS

E. M. Wright, D. Richardson and S. W. Koch, "Bifurcations of Scattering Orders in Degenerate Four-Wave-Mixing," Opt. Lett. 14, 75 (1989).

B. P. McGinnis, E. M. W·ght, S. W. Koch, and N. Peyghambarian, "Observation of New Scattering Orders in Degenerate Four-Wave Mixing with Semiconductors," Phys. Rev. A 41, 523 (1990).

D. Richardson, E. M. Wright, and S. W. Koch," Raman-Nath Theory of Degenerate Four-Wave Mixing in Semiconductors," Phys. Rev. A 41, 1620 (1990).

B. P. McGinnis, E. M. Wright, S. W. Koch, and N. Peyghambarian, "Formation of Transverse Spatial Ring Structures in Increasing Absorption Optical Bistability," Opt. Lett. 15, 258 (1990).

B. P. McGinnis, E. M. Wright, S. W. Koch, and N. Peyghambarian, paper QFD3, "Transverse Effects in Increasing Absorption Optical Bistability," XVII International Conference on Quantum Electronics IQEC'90, Anaheim, CA, May 21 - 25, 1990.

D. Richardson, B. P. McGinnis, E. M. Wright, N. Peyghambarian, and S. W. Koch, "Raman-Nath theory of degenerate four-wave mixing in semiconductors II: Time-dependent analysis and comparison with pulsed experiments," Phys. Rev. A (submitted for publication).

SCIENTIFIC PERSONNEL

S. W. Koch   D. Richardson
N. Peyghambarian   B. P. McGinnis
E. M. Wright

OBJECTIVES

Our objective was to develop a theory for and to perform experiments in degenerate four-wave mixing (DFWM) in semiconductors. In particular, we wanted to develop a model for DFWM in semiconductors, taking into account gratings caused by absorption and by refractive index. We proposed to analyze the physical origin of the DFWM in semiconductors by comparing the measured diffraction efficiencies with calculated values. In addition, we planned to determine the relative efficiency of the absorption versus refractive index grating by comparing experimental results to theoretical calculations.

RESEARCH FINDINGS

Not only did we meet our objectives, we discovered unexpected bifurcation and spatial structure formation phenomena, and investigated these phenomena in some detail.

We developed a theory of degenerate four-wave mixing in the Raman-Nath approximation that includes transverse effects and excitation-dependent optical material properties. We used the Banyai-Koch plasma theory to compute the nonlinear absorption and refractive index changes of laser-excited semiconductors. In our first application of the DFWM theory we solved the rate equation for the transverse carrier-density grating profile in steady state for the case of bulk GaAs. The resulting spatial scattering spectra were used to determine the expected diffraction efficiency of the grating formed as a function of excitation frequency. Numerical results for the Raman-Nath scattering spectrum were obtained for room-temperature bulk GaAs. An example of the computed transmission and diffraction efficiency is shown in Fig. 1.

When we compared our results with predictions of the commonly-used small-signal theory, considerable discrepancies were revealed at high intensities—precisely the operational regime in which nonlinear optical effects become relevant and useful in device applications.

Applying our theory to the case of a semiconductor for which the absorption increases with increasing carrier density (e.g., through bandgap renormalization), we discovered that a bifurcation of the scattering orders may occur. We predicted that novel bifurcating scattering orders can appear above the threshold for increasing absorption bistability. These scattering orders undergo subharmonic bifurcation with increasing input intensity. Experiments have been performed using the increasing absorption in thin CdS platelets. We employed tunable-frequency pulses a few nanoseconds in duration from a nitrogen-laser-pumped dye laser system for the measurements. As shown in Fig. 2, we observed the predicted new scattering orders, caused by subharmonic bifurcation of the laser-induced grating. Theory and experiment are in good qualitative agreement.

Next we computed the DFWM output profile in semiconductors with increasing absorption, and predicted the occurrence of transverse ring structures. We performed experiments on a thin CdS sample, and observed those structures. We can fit the temporal and spatial responses from the semiconductor platelet to the calculated induced absorption spectrum by choosing a carrier lifetime of 2 ns. For the transverse dimensions of the laser beam used in our experiment, transverse carrier diffusion was found to have little effect.
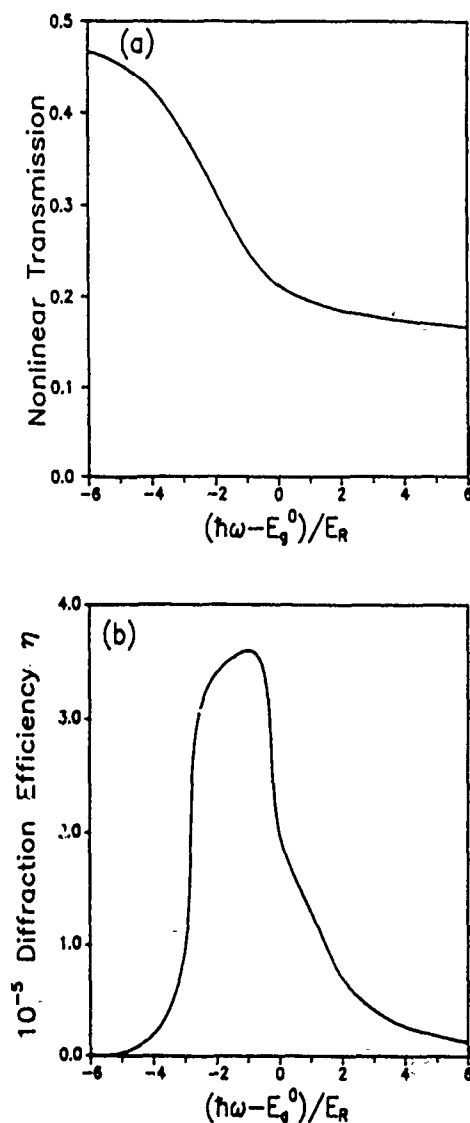
Figure   Computed transmission and diffraction efficiency versus detuning for bulk GaAs. The peuk diffraction efficiency occurs at a detuning of -1 E_R, where E_R is the exciton Rydberg energy (4.2 meV in bulk GaAs).

Finally, we extended our theoretical approach to DFWM to allow the analysis of pulsed DFWM experiments in laser-excited semiconductors.   An example of our experimental results for CdS is shown in Fig. 3, where we plot the DFWM diffraction efficiency spectra for a variety of pulse intensities.

To analyze these experimental results, we numerically solved the full time-dependent carrier-density grating equation, and computed the DFWM scattering spectra. To keep the analysis tractable, the timescale of the excitation pulses and the geometry of
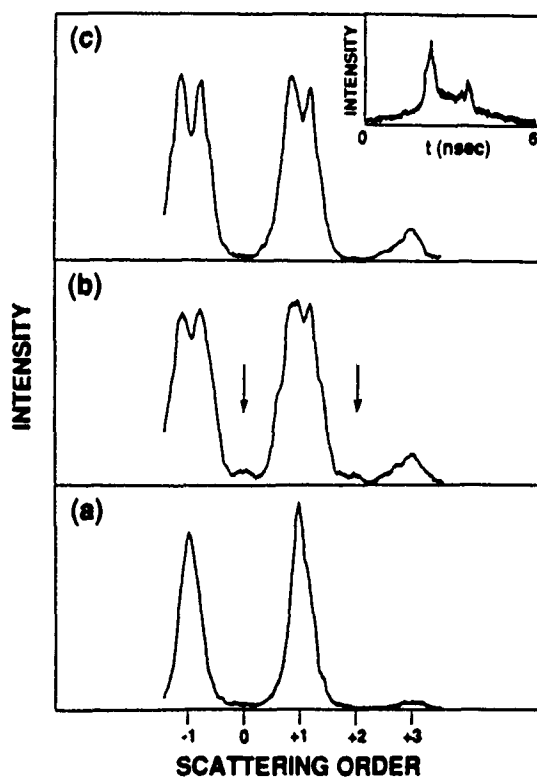
Figure 2. Central portion of the experimental scattering spectrum (far field) at (a) the beginning, (b) leading edge, and (c) peak of the laser pulse. The new scattering orders are marked by arrows.

the input beams are assumed to be such that the influence of diffusion on the transverse carrier-density profile can be neglected. An example of the results is shown in Fig. 4.

A comparison of Fig. 3 to Fig. 4 shows qualitative agreement between experiment and theory. The theory reproduces the dominant spectral features of the experiment with the observed relative magnitudes, while the predicted diffraction-efficiency peaks display the same broadening and red-shifting trends as those observed. The experimental behavior of the secondary peak at ≅481 nm is reproduced particularly well, with the peak height falling about a factor of four with each ten-fold increase in energy, in both the theoretical and observed curves. The main discrepancy between theory and experiment is in the absolute value of the diffraction efficiency, most likely the result of fitting the plasma theory predictions for $\alpha(\omega,N)$ and $\Delta n(\omega,N)$ to the experimental linear spectrum for one sample, while trying to match the predicted output scattering spectra with the experimental results from a different sample.
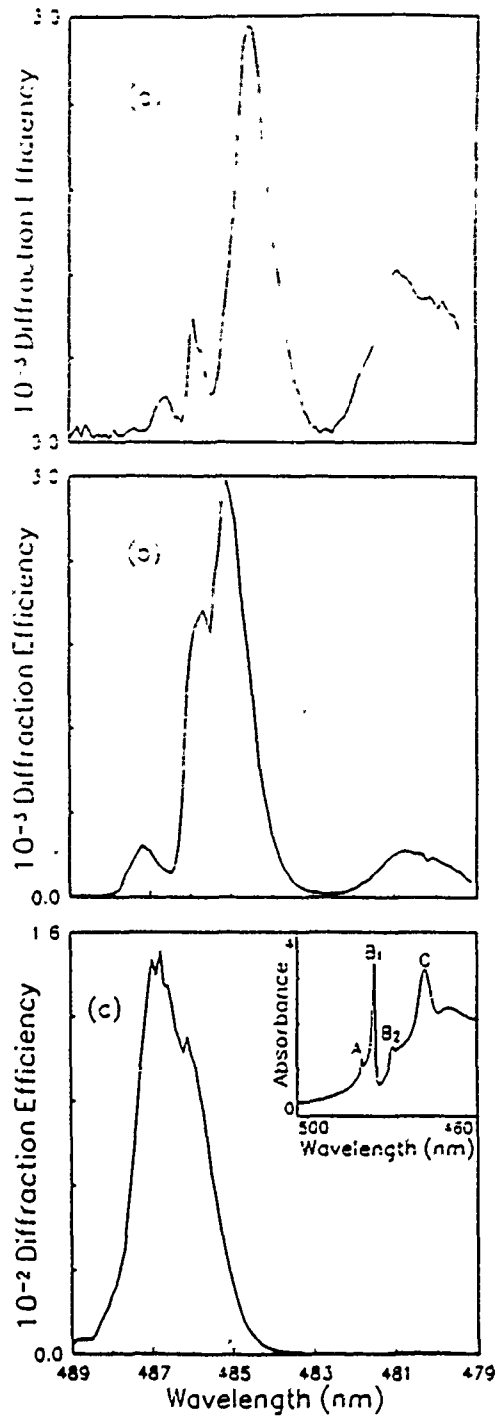
Figure 3. Experimental diffraction efficiency spectra for CdS. Sample thickness was 5 μm. Peak pulse energies were (a) 4 nJ, (b) 40 nJ, (c) 400 nJ. Inset to (c) shows the linear absorption spectrum for a sample of CdS less than 0.2 μm thick. Sample temperature for DFWM and absorption measurements was 30 K. Spot radius w_0 = 37.5 μm. Beam internal angle ≅ 0.5°.
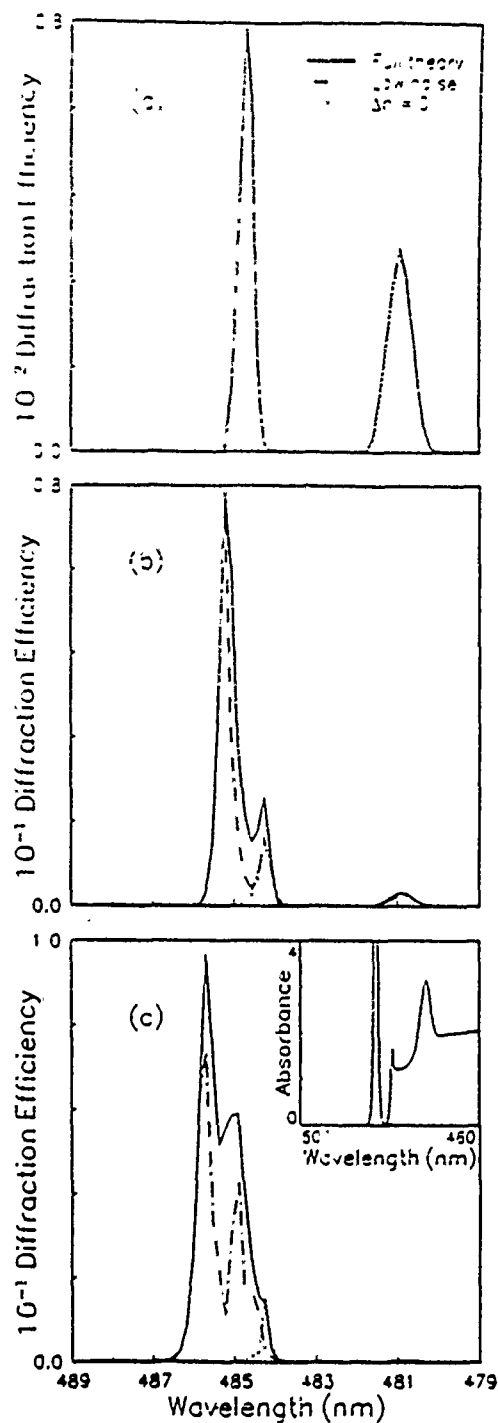
Figure 4. Predicted diffraction efficiency spectra (solid curves) given by the Raman-Nath theory, corresponding to the experimental curves of Fig. 3. The inset to (c) shows the linear absorption spectrum predicted by the plasma theory, with $\Gamma = 0.05$ and $\Gamma_1 = 0.0$ for the B exciton, and $\Gamma = 0.25$ for the C exciton. The A exciton was not modeled. The dashed curves give the corresponding results when Δn is arbitrarily set to zero throughout the calculations. The dash-dotted curves show the effect of a resolution-enhancement algorithm applied to the full numerical results. The pulse energies used in the simulations were (a) 0.08 nJ, (b) 0.8 nJ, and (c) 8.0 nJ.

In summary, we developed a theory of DFWM in the Raman-Nath regime that is valid beyond the small-signal regime, and thus has potential application to many DFWM experiments performed on highly-excited semiconductors. The theory accurately reproduces the qualitative features of experimental diffraction efficiency spectra for low-temperature CdS over a wide range of input-pulse energies. Analysis of the underlying material nonlinearities indicates that the observed red shift of the main diffraction efficiency feature is the result of excitonic-bleaching-related refractive-index changes and bandgap renormalization. Furthermore, in this project we predicted and observed bifurcation instabilities in DFWM, as well as the formation of spatial ring structures.

It is important to mention that our detailed theory-experiment comparisons clearly identify an intrinsic weakness of DFWM as a diagnostic tool for measuring semiconductor nonlinearities. This weakness lies in DFWM's reliance on the use of pump and probe beams at the same frequency. The nonlinearities under quasi-equilibrium conditions depend only on the density of generated carriers, which in turn is determined by the material absorption at the frequency of excitation. Hence, measuring the spectral dependence of the DFWM diffraction efficiency for constant intensity actually combines data for vastly different carrier densities. Furthermore, because the absorption at any given wavelength changes during the excitation, it is not a trivial task to accurately determine the excited carrier density and, hence, the expected absorption and refractive index changes. Comparisons between theory and experiment are possible only because the plasma theory provides a detailed model for the material nonlinearities, a model which has been tested independently using pump-probe experiments. From measured DFWM diffraction efficiencies in semiconductors alone, we do not consider it feasible to obtain reliable information on the semiconductor nonlinearities at high intensities. We believe pump-probe experiments with a spectrally narrow pump beam and a white-light probe are the superior technique for this purpose.

THEORY OF THE SEMICONDUCTOR LASER

M. Sargent III and S. W. Koch

PUBLICATIONS

Papers

M. Sargent III, Fenglei Zhou, and S.W. Koch, "Multiwave mixing in semiconductor media," Phys. Rev. A 38, 4673 (1988)

H. Haug and S.W. Koch, "Semiconductor laser theory with many-body effects," Phys. Rev. A 39, 1887 (1989).

C. Ell, H. Haug, and S.W. Koch, "Many-body effects in gain and refractive index spectra of bulk and quantum-well semiconductor lasers," Opt. Lett. 14, 356 (1989).

M. Lindberg, S. An, S.W. Koch, and M. Sargent III, "Strong-field modulation of semiconductor luminescence spectra," Phys. Rev. A 40, 4415 (1989).

F. Zhou, M. Sargent III, S.W. Koch, and W. Chow, "Population pulsations and sidemode generation in semiconductors," Phys Rev. A 41, 463 (1990).

W.W. Chow, S.W. Koch, and M. Sargent III, "The effects of electron-hole Coulomb interaction in semiconductor lasers," IEEE J. Quant. Electron. (June 1990).

A.E. Paul, M. Lindberg, S. An, M. Sargent III, and S.W. Koch, "Quantum theory of nondegenerate four-wave mixing in semiconductors," Phys. Rev. A 42, 1725 (1990).

W. Chow, S.W. Koch, M. Sargent III, and C. Ell, "Many-body effects on the linewidth enhancement factor in quantum-well lasers," Appl. Phys. Lett. accepted for publication.

M.H. Rose, M. Lindberg, W.W. Chow, S.W. Koch, and M. Sargent III, "Composite-cavity-mode approach to single-mode semiconductor laser feedback instabilities," Phys. Rev. A, submitted for publication.

Invited Presentations/Conference Proceedings

S.W. Koch, "Many-body theory of bulk and quantum-well semiconductor lasers," 5th New Zealand Symposium on Quantum Optics, Rotorua, New Zealand, Feb. 13 - 17, 1989. Published as: S.W. Koch, H. Haug, C. Ell, M. Lindberg, and M. Sargent III, "Many-body theory of the electron-hole plasma in bulk and quantum-well semiconductor lasers," *Quantum Optics V*, D. Walls and J.D. Harvey, eds. (Springer Verlag, Berlin, 1989); p. 235.

M. Sargent III, F. Zhou, S. An, M. Lindberg, S.W. Koch, "Theory of a semiconductor laser," *Quantum Optics V*, D. Walls and J.D. Harvey, eds. (Springer Verlag, Berlin, 1989), p. 246.

S.W. Koch, "Theory of optical nonlinearities in bulk and quantum-well semiconductor lasers," Paper JG4, Conference on Quantum Electronics and Laser Science QELS'89, Baltimore, April 24 - 28, 1989.

S.W. Koch, H. Haug, M. Sargent III, and N. Peyghambarian, "Optical nonlinearities in bulk and quantum-well semiconductors and semiconductor quantum dots," Fifth Interdisciplinary Laser Science Conference ILS-V, Stanford, CA, August 28 - 31, 1989. Published in: APS Bulletin 34, 1681 (1989).

M. Sargent III and S.W. Koch, "Multiwave mixing in semiconductor media," International Conference Lasers '89, New Orleans, Dec. 4 - 7, 1989.

M. Sargent III, S.W. Koch, and W.W. Chow, "Theory of a semiconductor laser," International Conference on Nonlinear Optical Materials and Devices for Photonic Switching, SPIE OE/LASE'90, Los Angeles, CA, Jan. 14 - 19, 1990. Published in: *Nonlinear Optical Materials and Devices for Photonic Switching*, Proc. SPIE 1216, 130, (1990).

S.W. Koch, "Optical nonlinearities in semiconductors," International Workshop on Space-Time Complexity in Nonlinear Optics, Tucson, AZ, March 12 - 16, 1990.

M. Sargent III, S.W. Koch, and W.W. Chow, "Theory of a single-mode semiconductor laser," International Workshop on Space-Time Complexity in Nonlinear Optics, Tucson, AZ, March 12 - 16, 1990.

S.W. Koch, "Many-body Coulomb effects in SCL media," Aspen Workshop on Physics of Semiconductor Lasers, Aspen, CO, May 28 - June 8, 1990

Contributed Presentations/Conference Proceedings

C. Ell, S.W. Koch, H. Haug, and M. Sargent III, "Semiconductor laser theory with many-body effects," Annual Meeting of the Optical Society of America, Santa Clara, CA, Oct. 31 - Nov. 4, 1988.

M. Lindberg, S. An, S.W. Koch, and M. Sargent III, "Pump field modulation of resonance fluorescence in semiconductors," Annual Meeting of the Optical Society of America, Santa Clara, CA, Oct. 31 - Nov. 4, 1988.

M. Sargent III and S.W. Koch, "Multiwave mixing in semiconductor media," Annual Meeting of the Optical Society of America, Santa Clara, CA, Oct. 31 - Nov. 4, 1988.

F. Zhou, M. Sargent III, and S.W. Koch, "Sidemode generation in semiconductor lasers due to population pulsations," 6th Rochester Conference on Coherence and Quantum Optics, Rochester, N.Y., June 26 - 28, 1989. Published in: Proceedings of the 6th Rochester Conference on Coherence and Quantum Optics.

A.E. Paul, M. Lindberg, S. An, M. Sargent III, and S.W. Koch, "Quantum theory of nondegenerate four-wave mixing in semiconductor media," 6th Rochester Conference on Coherence and Quantum Optics, Rochester, N.Y., June 26 - 28, 1989. Published in: Proceedings of the 6th Rochester Conference on Coherence and Quantum Optics.

K. Henneberger, H. Haug, W. Schäfer, R. Binder and S.W. Koch, "Spectral hole burning in active and passive semiconduc' 'rs," XVII International Conference on Quantum Electronics IQEC'90, Anaheim, CA, M..,' 21 - 25, 1990.

M. Sargent III, S.W. Koch, and W. W Chow, paper QThA1, "Onset of sidemode buildup in semiconductor lasers," XVII International Conference on Quantum Electronics IQEC'90, Anaheim, CA, May 21 - 25, 1990.

S.W. Koch, W.W. Chow, and M. Sargent III, paper QThA7, "Effects of electron-hole Coulomb interactions in semiconductor lasers," XVII International Conference on Quantum Electronics IQEC'90, Anaheim, CA, May 21 - 25, 1990.

SCIENTIFIC PERSONNEL

M. Sargent III
M. Rose
A. Paul

OBJECTIVES

Our objective was to derive a consistent set of quantum mechanical equations for the electron-hole system in semiconductors, including the many-body Coulomb effects and the contributions of electron-electron and hole-hole intraband scattering, and electron-hole scattering.

Assuming quasi-equilibrium within the electron-hole system, we proposed to calculate the steady-state properties of the semiconductor laser and the laser threshold. We planned to compute the steady-state gain spectrum and to couple our microscopic model of the semiconductor nonlinearities to the Maxwell equations for the laser fields, to predict these fields in a consistent manner. We proposed to study instabilities and sidemode build-up in bulk and quantum-well semiconductor lasers.

RESEARCH FINDINGS

Not only did we reach the goals of our project, we expanded our studies to investigate semiconductor laser luminescence, four-wave mixing in semiconductor laser media, and semiconductor lasers in a feedback cavity. In the first phase of our project we developed a consistent many-body description of the electron-hole plasma of a

semiconductor laser.   Our theory includes plasma screening, bandgap renormalization, broadening due to intraband scattering, and Coulomb enhancement effects.   We computed the room-temperature gain/absorption and refractive index spectra for the representative cases of three- and two-dimensional GaAs.   Our results show a pronounced expansion of the gain region for increasing plasma densities as a consequence of the increasing quasi-chemical potential and the decreasing renormalized semiconductor bandgap.   At the same time we show that the peak of the corresponding refractive index spectra shifts to higher energies, causing negative index changes in the gain regime.   An example of computed gain spectra for the case of a quantum-well laser medium is shown in Fig. 1.
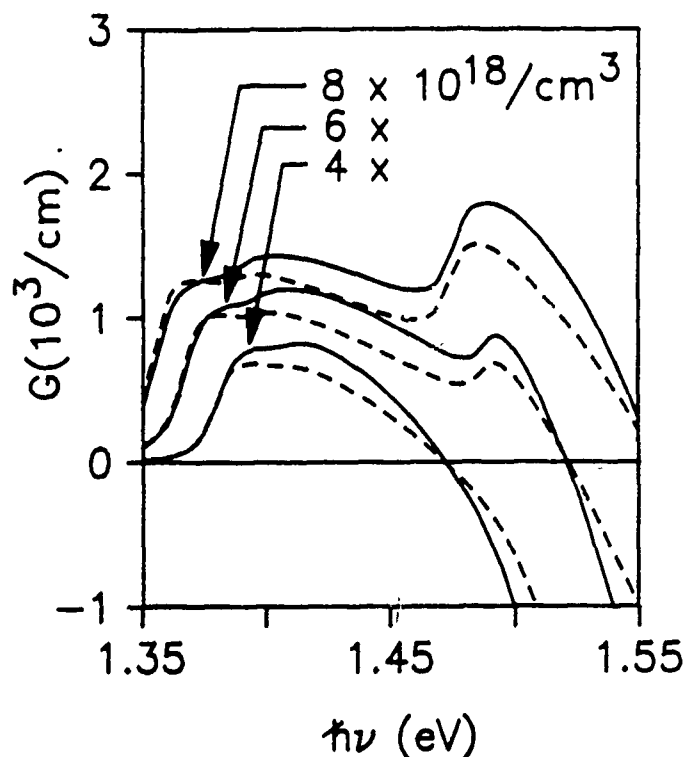

Fig. 1.   Computed gain spectra for an undoped, 10-nm GaAs quantum-well active layer with $Ga_{0.8}Al_{0.2}As$ barriers, at room temperature.   The dashed curves are calculated by neglecting Coulomb enhancement effects.

From our microscopic results for carrier density-dependent gain and refractive index spectra, we can compute the so-called linewidth enhancement factor, α.   This factor essentially is the ratio of the density-dependent refractive index changes to the corresponding gain changes.   For bulk semiconductor media, we find that the α factor is almost carrier-density independent.   For the case of quantum-well lasers, however, we

predict strong variations of the linewidth enhancement factor with laser parameters. As shown in Fig. 2, our calculations indicate that significantly reduced α values can be obtained for some values of threshold carrier density. These reduced α values give a narrowed fundamental (i.e., spontaneous-emission limited) laser spectrum, and the reduction of filamentation. Quantum-well lasers can be designed to take advantage of these substantial improvements with the proper combination of facet reflectivities, optical cavity dimensions and quantum-well structure.
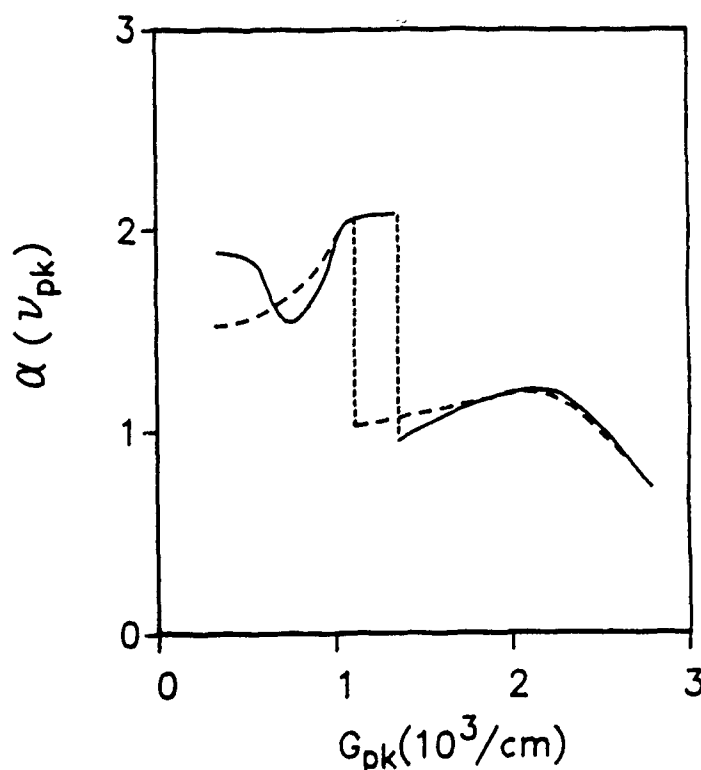

Fig. 2. Linewidth enhancement factor, α, at the peak gain frequency versus peak gain for a 10-nm quantum well with gain spectra shown in Fig. 1.

Using the microscopic description of the electron-hole plasma in semiconductor-laser media, we investigated the resonance fluorescence spectrum of a bulk semiconductor subject to an injection current and an arbitrarily intense electromagnetic wave. Although the fast carrier-carrier scattering heavily damps the electronic coherence, it nevertheless allows the medium to adiabatically follow the relatively slowly varying field fluctuations. As a consequence, the resonance fluorescence spectra reveal an asymmetric peak generated by pump scattering off carrier-density pulsations induced by the interference between the pump and a vacuum mode.

We also applied our many-body theory to investigate sidemode generation, from population pulsation, in semiconductor lasers. Using third-order perturbation expansions with respect to the field amplitude we can derive a set of coupled equations for the semiconductor polarization and the field modes. Below, we discuss propagation problems in semiconductor laser media and evaluate the theory for the example of nondegenerate four-wave mixing in an amplifier configuration. The dependence of the sidemode intensity on the length of the active medium, on the intermode beat frequency, and on the pump wave intensity is also discussed.

We developed a quantum theory for nondegenerate four-wave mixing and applied it to study a highly excited semiconductor resonator operating below or near laser threshold. We found that the total carrier-density pulsations allow coherent effects in semiconductors despite the rapid decay of the electron-hole correlations. We calculated the effects of a strong pump mode on the sidemode absorption spectrum and on the resonance flurescence. Our results show that these quantities are greatly modified in the spectral region around the pump, and enhance the four-wave-mixing spectra. Absorption and luminescence spectra exhibit asymmetric dips for sufficiently strong pumping. These features have their origin in the scattering of the pump field into the side modes by carrier density fluctuations.

A well-known problem with the application of semiconductor lasers is that they exhibit a variety of instabilities under external feedback conditions wherein a fraction of the emitted light is reflected back into the laser cavity. These instabilities depend strongly on system parameters, such as the amount of feedback, the operating point of the laser, and the ratio of the laser cavity length to the distance between the laser's output mirror and the feedback mirror. To create a well-defined model of a semiconductor laser under feedback conditions, we investigated such a laser in an external high-quality cavity, using a composite-resonator eigenmode description of two coupled resonators. In this case, the laser field in the presence of feedback is expanded in the modes of the total cavity (the laser cavity plus an additional mirror). We studied the laser threshold as a function of cavity parameters such as the ratio of the length of the laser cavity to the total cavity, or the reflectivity of the coupling mirror. As shown in Fig. 3, we found pronounced laser frequency hopping accompanied by threshold carrier density changes for changes in length on the order of a fraction of the light wavelength.
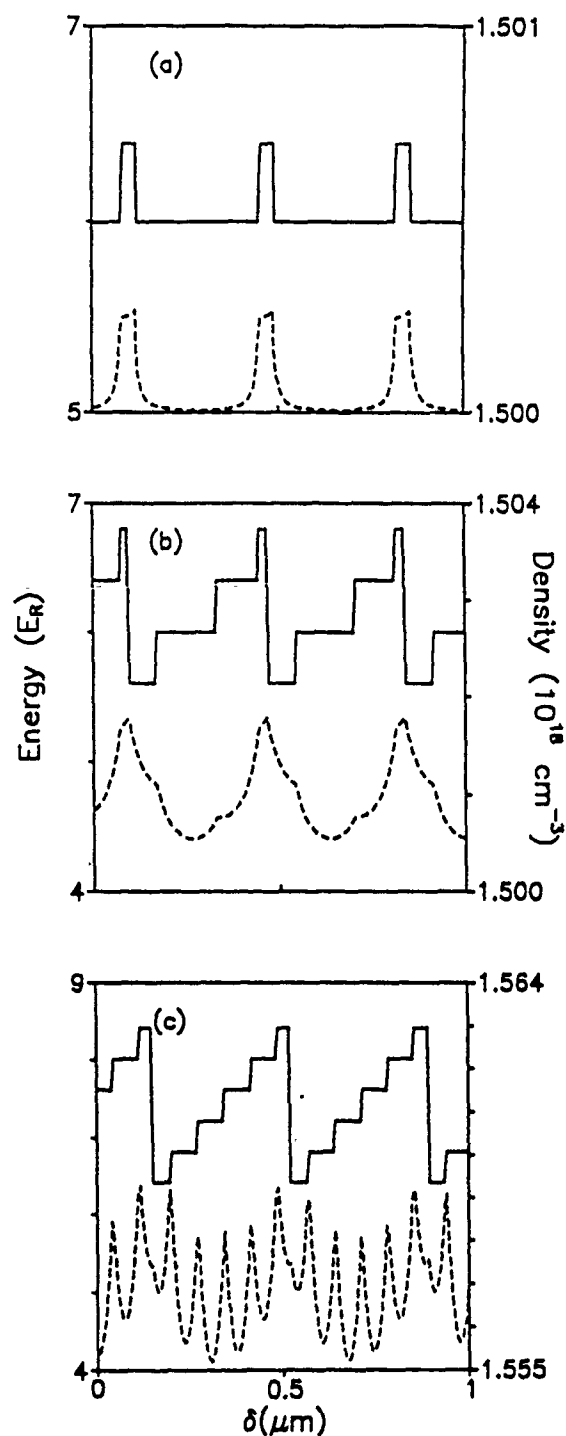
Fig. 3. Energy of the lasing mode (solid line) in units of E_R (4.2 meV for bulk GaAs) and threshold carrier density (dashed line) as a function of the variation in external cavity length, δ (µm). The transmission coefficients of the coupling mirror are: a) $T = 10^{-5}$; b) $T = 10^{-3}$; and c) $T = 0.1$.

In summary, over the past three years we gained a clearer understanding of the many-body and mode-interaction effects in semiconductor laser media. Our results show the fundamental limitations of bulk and quantum-well media, and indicate several possibilities for improving aspects of device performance. In the near future we plan to continue our research into semiconductor laser instabilities, spectral hole burning, and gain dynamics in bulk and quantum-well systems. We recently undertook investigations in the area of "gain engineering." We are exploring bandstructure modifications, for example, through strained layer growth in quantum-well systems, that can lead to lower-thr hold devices and reduced temperature sensitivity. Furthermore, we are studying the influence of many-body effects on ultrashort cavity surface-emitting laser diodes.

NONLINEAR THEORY OF PHASE CONJUGATE OPTICS

Ewan M. Wright

PUBLICATIONS

1. N.N. Akhmediev, D.R. Heatley, G.I. Stegeman, and E.M. Wright, "Pseudo-recurrence in two-dimensional modulation instability with a saturable self-focusing medium," Phys. Rev. Lett. **65**, 1423 (1990).

2. P. Varatharajah, A.C. Newell, J.V. Moloney and E.M. Wright, "Stationary nonlinear waves guided by thin films bounded by nonlinear diffusive media," submitted to J. Opt. Soc. B.

3. E.M. Wright, "Quantum theory of self-phase modulation," J. Opt. Soc. Am. B **7**, 1142 (1990).

SCIENTIFIC PERSONNEL

Ewan M. Wright
David R. Heatley
Glenn Soneneberg

RESEARCH FINDINGS

Objectives

The now standard theory of nonlinear optical phase conjugation considers the interaction of a weak probe beam incident at an angle with respect to two strong, and counterpropagating pump beams, within a nonlinear medium. This geometry produces a phase conjugate replica of the probe beam that travels in the reverse direction to the probe. In general, several other scattering orders, other than that responsible for phase conjugation, may be produced in this nonlinear interaction, but these invariably are ignored in theoretical treatments. If the angle of incidence is large enough, this model, referred to as the Bragg regime, is appropriate and yields reliable results. Multiple scattering orders appear when the angle of incidence is very small. This is referred to as the Raman-Nath regime. The objective of this project was to investigate the transition between these two extreme scattering regimes.

Progress

To achieve the proposed research a computer program was constructed that properly reproduced the known analytic results in the Bragg and Raman-Nath regimes.

The initial stage of this program already covered all previous analyses of the problem; however, many instabilities were encountered in the intermediate regime. The initial numerical problems were easily overcome, but the programs still displayed instability phenomena: these instabilities were intrinsic to the system of equations we were using and, therefore, to the physical process of optical phase conjugation. However, for large angles of incidence (and similarly for small angles of incidence) of the probe beam, phase-matching constraints usually prevail and these instabilities are not present. This explains why we were able to reproduce the previous analytic results.

To gain an understanding of these instability phenomena a simpler geometry was adopted in which only one pump beam was present and was copropagating with the probe. In this geometry our investigations showed that the instabilities were modulational instabilities,[1] which are well known from other fields of physics and nonlinear dynamics. Modulation instabilities belong to a class of periodic solutions of the nonlinear wave equation, and have been appplied in nonlinear fiber optics. In particular, it has been shown that many initial conditions can recur to the initial state to within a phase factor upon propagation. The interest in such periodic solutions is connected with the study of chaos in nonlinear propagation as they describe periodic orbits. In the presence of small perturbations the solution can shift from a given orbit to adjacent periodic ones whose periods are sensitive to the size of the displacement. Therefore, modulation instabilities can lead to both chaotic and turbulent effects in nonlinear propagation in the presence of a small perturbation. In the case of optical phase conjugation the two pump beams are responsible for the modulation instability and the weak signal beam acts as a perturbation. Our work has established the direct relationship between these instabilities and the phenomenon observed in the numerical simulations of optical phase conjugation in between the Bragg and Raman-Nath regimes. These results also could be related directly to observed instability phenomena in thin film nonlinear waveguides,[2] for which the instabilities could be controlled by varying the thickness of the thin film.

In the initial phase of the program only classical optical fields were considered. However, recent proposals for producing nonclassical light sources such as squeezed light have pointed to optical phase conjugation as a physical mechanism. For this purpose a quantum propagation theory has been developed which combines the ideas of quantum optics with the more traditional methods of classical propagation theory.[3]

POLISHING OF DIAMOND FILMS WITH ARGON AND OXYGEN ION BEAMS

B. Bovard, D. F. Grogan, T. Zhao, and H. A. Macleod

SCIENTIFIC PERSONNEL

B. Bovard
D. F. Grogan
H. A. Macleod
T. Zhao

RESEARCH FINDINGS

Objectives

Our objective is to develop the technique of ion beam polishing of diamond films deposited by microwave-assisted chemical vapor deposition (CVD) using a planarizing layer. As an intermediate goal, we have polished AT-cut quartz disks used in rate monitors. Using an argon ion beam and spin-coated photoresist as the planarizing layer, we successfully reduced the peak-to-valley (p-v) surface roughness in these disks from 5 μm to 0.2 μm. The etch rate of diamond films, under argon bombardment is minute, o for diamond films reactive oxygen ions constituted the beam. The planarizing o\ t, designed so that its etch rate would match that of the diamond film, was a mixture of photoresist and titanium-silica. With this combination, we reduced the diamond films' surface roughness from 6 μm to 217 nm peak-to-valley, and from 1 μm to 35 nm rms. This success opens the field of infrared optics to diamond films.

PROGRESS

Background

Diamond has many excellent optical properties, including an absorption edge in the ultraviolet (230 nm) and a high transparency throughout the visible and most of the infrared region. For some time, attempts have been made to produce optically smooth surfaces on diamond films deposited by CVD. Unfortunately, the crystallites produced in diamond films range in size from submicron to several microns, depending on the growth process. Furthermore, the higher the quality and the growth rate of the film, the rougher its surface tends to be. As a result, diamond films exhibit significant surface roughness and optical scatter, hence, they are not yet easily used as optical materials. It is necessary to polish diamond films to permit their use in optical applications.

Conventional polishing methods, such as mechanical and chemical polishing, may be difficult, because diamond is both the hardest material known and is chemically inert. Moreover, deamond films are too thin (typically on the order of tens of microns) for these methods, and sometimes not flat enough because of high internal stress. In 1965, A. B. Meinel et al. predicted that ion beam polishing would be useful to figure optical surfaces to great accuracy.[1] Since then, many techniques to modify the surface condition of optical materials by ion bombardment have been developed. Among them is ion-beam planarizing. A liquid is spin-coated onto the surface to be polished. Upon baking, it hardens to form a smooth, flat, homogeneous planarizing film. The smoothness of the new surface depends on the overcoat characterisitics, the topography of the substrate, and the spinning and baking processes.[2] The key to this method is that the beam's ions impinge on the new surface at an angle such that the overcoat and substrate have the same etch rates.[3] Once all of the overcoat is removed by the ion beam, a new surface is obtained of about the same smoothness as the overcoat. Because diamond films were not readily available, and prohibitively costly, we used AT-cut quartz wafers of the same order of surface roughness as that of diamond films to develop the technique. An argon ion beam, and photoresist as the planarizing film, proved satisfactory for ion-beam planarizing of AT-cut quartz. We then applied the technique to diamond films. Because diamond has a very low etch rate under argon ion bombardment, the polishing process had to be modified. Reactive ion beam planarizing with oxgen, rather than argon, was used; the overcoat consisted photoresist and titanium-silica, which has a lower etch rate than that of pure photoresist. We obtained an optical surface of diamond with this technique.

Experimental

The experiments described below were carried out in an Edwards Box Coater (base pressure $<5 \times 10^{-6}$ torr). The ion beam is produced by a 3-cm hot cathode Kaufman ion source. The sample is mounted in an aluminum holder, which rotates around its own axis at a speed of 16 cycles/min. The distance between substrate center and ion-gun grid is 13 cm. Two Faraday cups were used to calibrate and monitor the ion flux at the substrate. The working pressures were 2.2×10^{-4} and 1.7×10^{-4} torr for argon and oxygen, respectively.

Roughness measurements were taken with a 2-dimensional Wyko profilometer, using a 660 μm spot size. We emphasize that the roughness values would be different if we had used a three-dimensional profilometer and/or a different spot size.

Quartz wafer polishing

AT-cut quartz wafers, designed for depostion-rate monitoring, were mounted with adhesive on a 2.5 cm × 2.5 cm glass plate. Photoresist diluted with thinner was applied to the quartz with a spinning speed of 3500 cycles/min for 30 seconds. The coated quartz was baked at 160°C for 30 min. This procedure was repeated until an acceptable surface was produced. Figure 1 shows the quartz and photoresist etch rates versus incidence angle. At 60° both materials have the same rate of 570 Å/min under 500 eV argon ion bombardment. The coated quartz was ion polished until all of the overcoat was removed. The ion current density was 1.39 mA/cm².

Diamond film polishing using Ar⁺

The microwave-assisted CVD diamond film samples were produced by Crystallume Corp. To determine the etch rate as a function of incident angle for a beam of 500-eV argon ions, the diamond films were partly masked with a thin glass plate, and polished at an incident angle of 60° for 90 min. Because carbon has a very low rate under argon ion bombardment, and because the diamond surface was extremely rough, accurate rate data were not obtained. However, when we increased the ion beam energy to 1000 eV, we measured a removal rate of 111 Å/min. We noted this value was comparable to the etch rate of graphite, 133 Å/min under the same parameters. Unfortunately, the graphite curve failed to intersect that of the overcoat at any angle. The use of a simple photoresist overcoat, therefore, was impossible.

Diamond film polishing by reactive ion (oxygen) beam planarizing

Because single crystal diamond has a much higher yield in an oxygen ion beam than in one of argon, reactive ion beam polishing was selected. This selection required that the removal rate of the overcoat be reduced. This was achieved by recognizing that titanium has a low etch rate in the presence of oxygen. Figure 2 shows the dependence of the etch rate on the angle of ion incidence on diamond and on an overcoat consisting of a mixture of photoresist and titanium-silica. By varying the index of titanium-silica and the relative amounts of photoresist and titanium-silica, an angle of common etch rate was found.

Figure 3 shows the triangular crystallites typical of the diamond texture. The diamond films were coated with the photoresist/titanium-silica overcoat 4 to 7 times, depending on the initial surface condition. The coated sample was baked at 140°C for
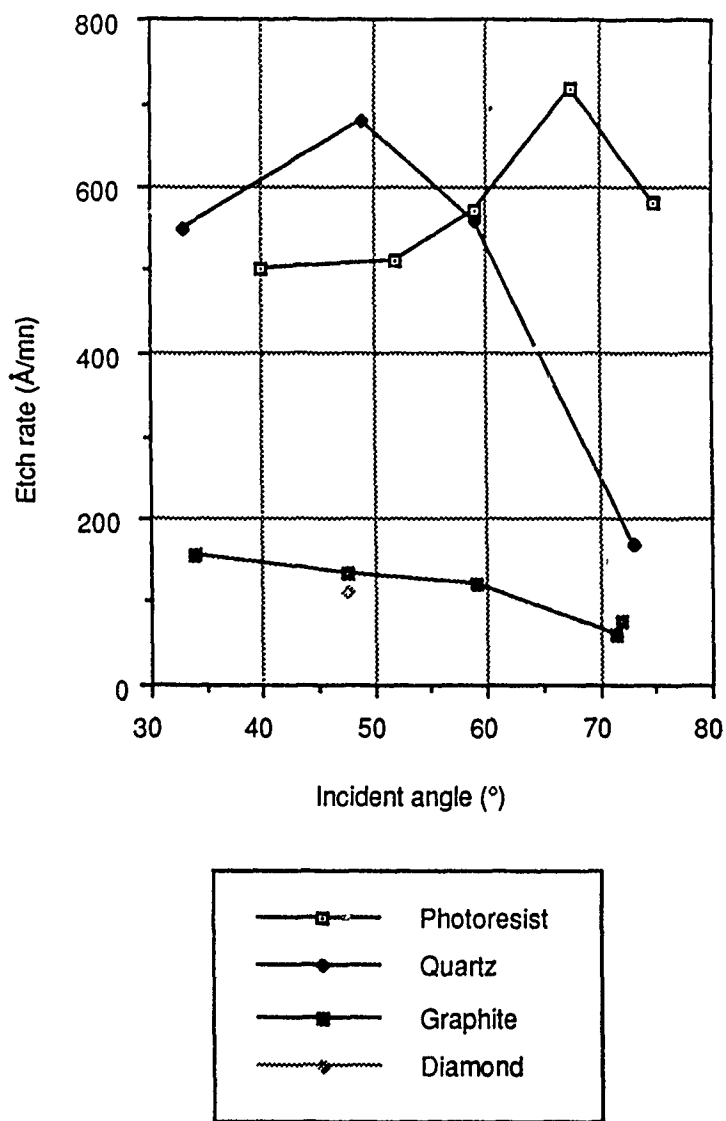
Figure 1. Etch rate for Ar⁺ ion bombardment. Ion energy: 500 eV for quartz and photoresist and 1000 eV for graphite and diamond (ion current density: 1.39 mA/cm²).

30 minutes between coatings. We found the limit for overcoat smoothness after coating was about 30 nm rms, and 150 nm p-v, depending mainly on the initial topography of the diamond surface. The ion current density was 0.2 mA/cm². Figures 5 through 7 show the evolution of the surface during the polishing process.
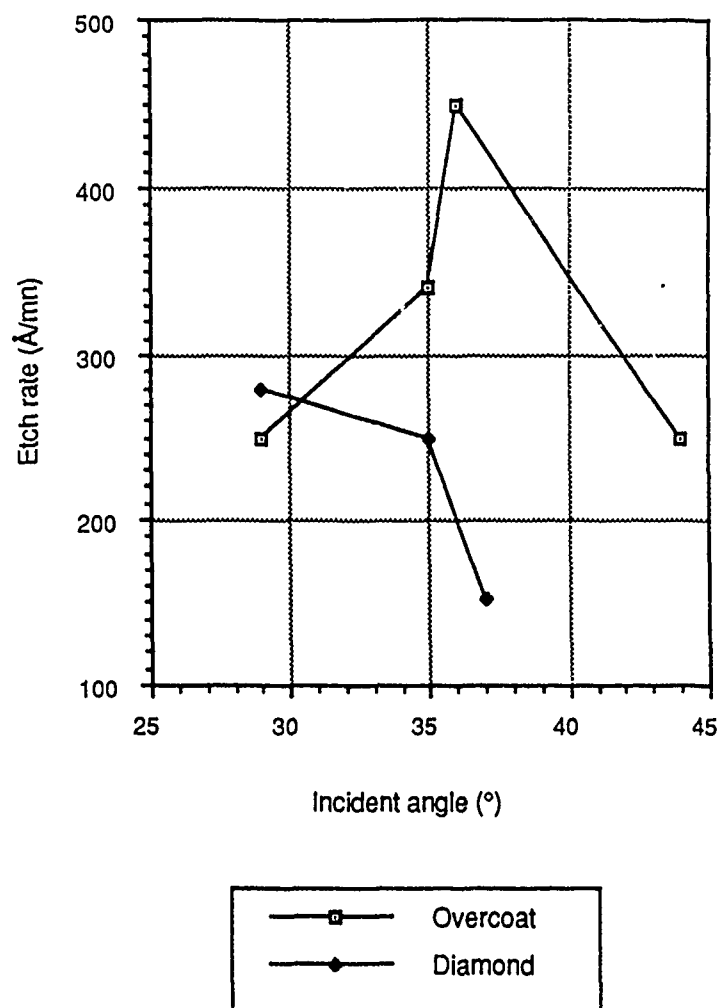
Figure 2. Comparison of the etch rates of the planarizing layer and of the diamond film subjected to 500-eV oxygen ion bombardment.

Results

Quartz wafer polishing

For the quartz samples p-v roughness before polishing was measured to be 2 μm, with a Dektak stylus profilometer. Under scanning electron microscopy, we found the value to be 5 μm. One reason for the discrepancy may be that the stylus is too thick to reach the bottom of the valleys, causing it to underestimate the roughness. After polishing, a smooth surface, with nearly straight interference fringes under the interferometer, was obtained. The rms and p-v values are 35.2 nm and 216.7 nm, respectively.

Figure 3.   Original diamond film surface (×1000).

Diamond film polishing using Ar⁺

No progress was made on improving the surface of diamond films through argon-ion polishing because a planarizing film could not be produced with an etch rate equal to that of diamond.   After ion bombardment, we detected no modification of the surface.

Diamond film polishing by reactive ion (oxygen) beam planarizing

Because of the beam size limitation, only a region 1 cm in diameter in the center of our 2.5 cm × 2.5 cm sample was polished.   In this area the surface roughness of the sample was reduced from 1 μm (rms) and 6 μm (p-v), to 35 nm (rms) and 217 nm (p-v). The diamond phase was preserved, as shown by Raman spectroscopy.   An investigation of surface contamination using x-ray photoelectron spectroscopy showed that no contamination was present.
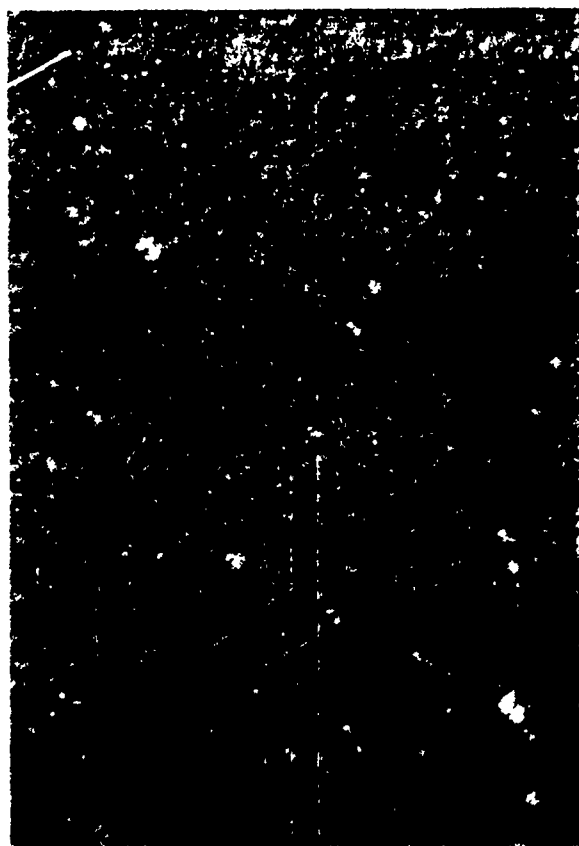
Figure 4.   Diamond film planarized with photoresist/titanium-silica (×200).

Conclusion and Future Work

Using reactive ion (oxygen) beam polishing, with the aid of a photoresist/titanium-silica planarizing film, we obtained an optically smooth surface in microwave-assisted diamond films deposited by CVD.   The rms roughness is 35 nm and the p-v roughness is 217 nm.   In developing the process we used AT-cut quartz samples using argon ion polishing, with pure photoresist as the overcoat, we obtained nearly the same surface condition.   This indicates that the final polish depends mainly on the planarizing film and its limitations.   Further work in progress focuses on smoother surfaces; larger polished areas using a 12-cm hot-cathode ion gun installed in a 760 Balzers coating plant; and characterization of the polished diamond films.   We are engaged in the development of polishing techniques that can be applied to free-standing films grown by
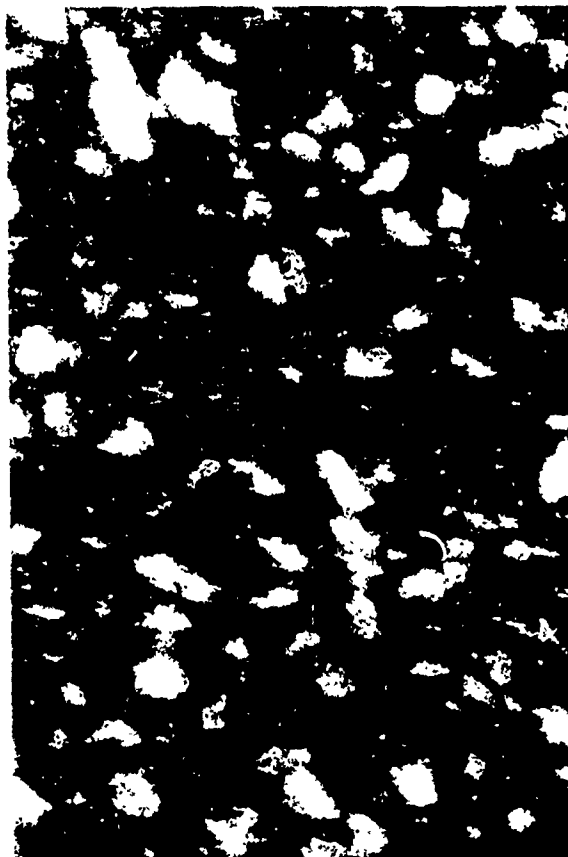
Figure 5. Planarized diamond film after polishing for 120 minutes with a 500 eV oxygen ion beam (×1000). The white regions are diamond surfaces and the darker regions correspond to the planarizing layer.

a flame process at the Naval Research Laboratory, and to 2-in.-diameter samples grown on silicon by Texas Instrument. This process is in competition with the hot-iron polishing process for samples on a substrate. Ion polishing has several advantages: it is a low temperature process (below 100°C); it is a noncontact method; and it does not leave any contaminants (shown by XPS measurements).[6]

The ability to improve surface condition of diamond films opens the possibility of measuring the optical constants of these films in the infrared, as well as infrared applications for which diamond is so promising.

We presented this work at the SPIE conference in San Diego (July 1990).[4] Further progress will be presented at the Annual Meeting of the Optical Society of America.[5]
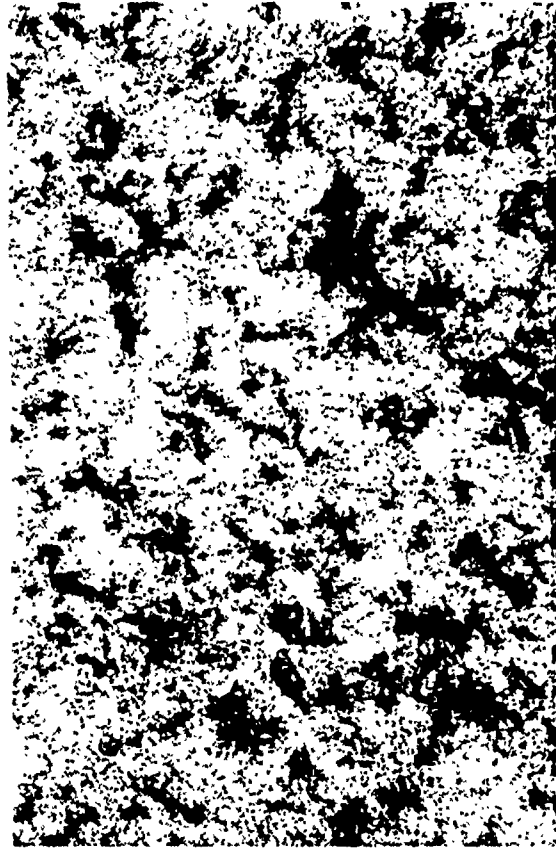
Figure 6. Planarized diamond film after polishing for 200 minutes with a 500 eV oxygen ion beam (×1000). A large amount of diamond is now at the surface with only a small amount of the planarizing layer remaining.

We plan to present a paper at the conference organized by the Society of Tribologists and Lubrication Engineers, to be held in 1991 in Montreal (Canada).

Acknowledgments

This work was also funded by S Cubed, a Division of Maxwell Laboratories. We greatly appreciate the kind support of the Wyko Corporation for their help in conducting surface measurements.

Figure 7.   Diamond film surface with overcoat removed (×1000) after 240 minutes of ion polishing.

REFERENCES

1.   A. B. Meinel, S. Bashkin, and D. A. Loomis, "Controlled figuring of surfaces by energetic ionic beams," Appl. Opt. 4, 1674 (1965).

2.   H. Gokan, M. Mukainaru, and N. Endo, "Uniform polymer coating technique for an etch-back planarization process using low molecular weight polymers." J. Electrochem. Soc. 135, 1019-1021 (1988).

3.   L. F. Johnson, K. A. Ingersoll, and D. Kahng, "Planarization of patterned surfaces by ion beam erosion," Appl. Phys. Lett. 40, 636-638 (1982).

4.   T. Zhao, D. F. Grogan, B. G. Bovard, and H. A. Macleod, "Diamond film polishing with argon and oxygen ion beams," Proc SPIE 1325 1990.

5. D. F. Grogan, T. Zhao, B. G. Bovard, and H. A. Macleod, "Ion beam polishing of diamond films using a planarizing technique," to be presented at the Annual Meeting of the Optical Society of America, Boston, 1990.

6. D. F. Grogan, "Ion beam polishing of diamond films," PhD Dissertation, University of Arizona, 1990.

CHEMICAL VAPOR DEPOSITION OF DIAMOND AND DIAMOND-LIKE FILMS

M. R. Jacobson, B. Bovard, and H. A. Macleod

SCIENTIFIC PERSONNEL

M. R. Jacobson	C. J. Craigie
B. Bovard	D. F. Grogan
H. A. Macleod	T. Zhao

RESEARCH FINDINGS

Objectives

Our objectives were

- to deposit diamond films with smooth surfaces to minimize or eliminate surface scattering.
- to perform this depostion ultimately at substrate temperatures low enough (<400°C) to insure the survival of most optical materials.
- to inhibit graphite formation.
- to increase deposition rates.

Progress

We used what limited funding remained after January 1990 to

- continue to develop plasma-enhanced chemical-vapor deposition (PECVD) techniques.
- complete the construction of a cold-wall chemical-vapor deposition (CVD) system with the capabilities of plasma, hot-filament, radio-frequency (RF), and laser-assisted deposition.
- characterize the coatings produced.

PECVD deposition

We continued to perform hot-filament chemical vapor deposition (CVD)[7] in the CVD-1000 reactor from Ion & Plasma Equipment. In the January 1990 report we summarized our results for thirty coating runs, including the process parameters used. We made one major change to our process parameters this spring. We boosted the substrate temperature from 400°C to greater than 800°C, using a custom-built heater from Tayco Engineering. (See Table 1.) This heater consists of a flat disk of high-temperature alloy, under which is brazed a spiral electrical resistance heater. A K-

thermocouple is attached to the disk for monitoring temperature. The heater is rated at 1100°C in air or vacuum. The actual deposition temperature, T_d, at various points on the substrate, is higher because of radiative heating by the hot filament. The filament also functions to generate activated hydrocarbon radicals.

After raising the substrate temperature we observed a change in the appearance of these films in scanning electron microscopy (SEM) micrographs. (See Figs. 1 and 2.) Runs 32 and 33 appeared especially promising, with fine, sharp crystallinity. These samples also exhibited equilateral triangles and other shapes indicating possible nucleation of diamond crystallites. We did not, however, observe the important Raman line at $\Delta\lambda$ = 1332 cm^{-1}. A micrograph and Raman spectra for sample 32-C appear in Fig. 3. We must presume, therefore, that these structures are some type of graphitic or related growth; we are fairly certain the Raman spectrometer is correct, in that bulk diamond surfaces have been readily detected. For confirmation we sent the sample to Dr. Wilson Smart of Crystallume. He initially identified the micrograph as that of diamond during a visit to our laboratory. His micro-Raman system, however, confirmed that no diamond crystallites were present. We continued to operate the CVD-1000 system through March, 1990, but a number of concerns led us to abandon our effort with the system and to use our limited time and funding to complete a second CVD system. Our concerns included

- a lack of significant diamond nucleation and growth.
- substrate orientation, observation, and heating limitations associated with the design of the CVD-1000 chamber. The chamber was not originally intended for the conventional range of diamond deposition parameters.
- the inability to operate the system under very soft vacuum (-20 < P < 100 torr).
- restrictions on the system's operating mode, such as single-process-cycle limitations to 99 minutes or less, arising from its highly automated control system.

Multiply-Assisted Cold-Wall CVD System

The second CVD system, built around a 250-kHz RF source and a quartz tube system, was designed to be more versatile and to permit us to interchange methods of radical species generation. The new system is depicted in Fig. 4. The chamber consists of a quartz tube 1 meter in length and 9 cm in diameter, with flat end flanges that mate with two end caps. At the exhaust end, the mating flage accommodates a 5-cm pumping line to a Roots blower-roughing pump package that brings the system to a base pressure, P_b, of a few millitorr. Beyond the flange, a servo-operated valve, controlled by
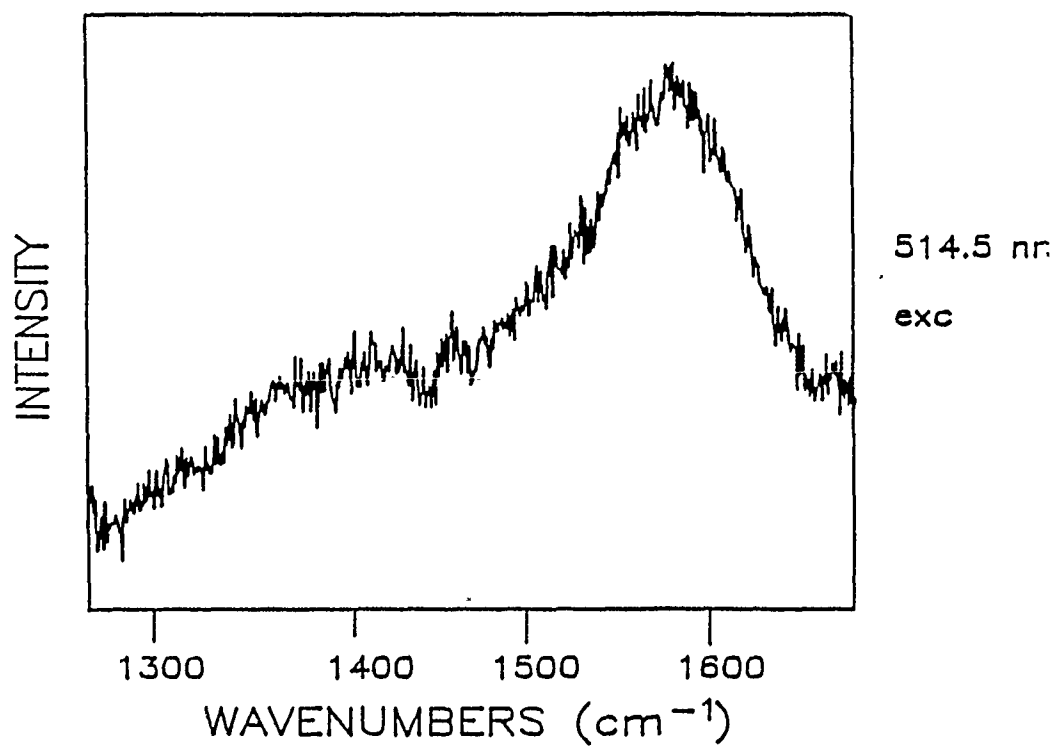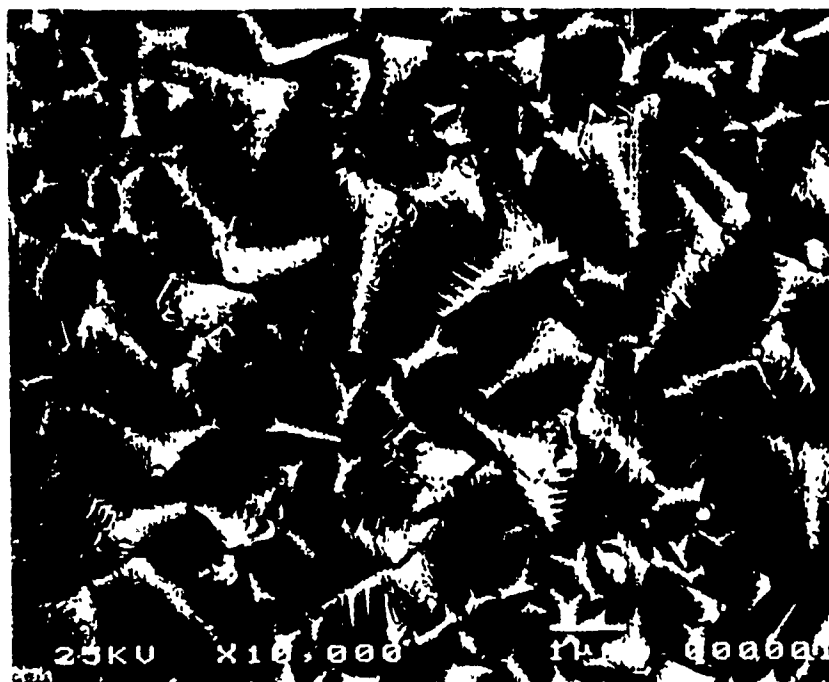
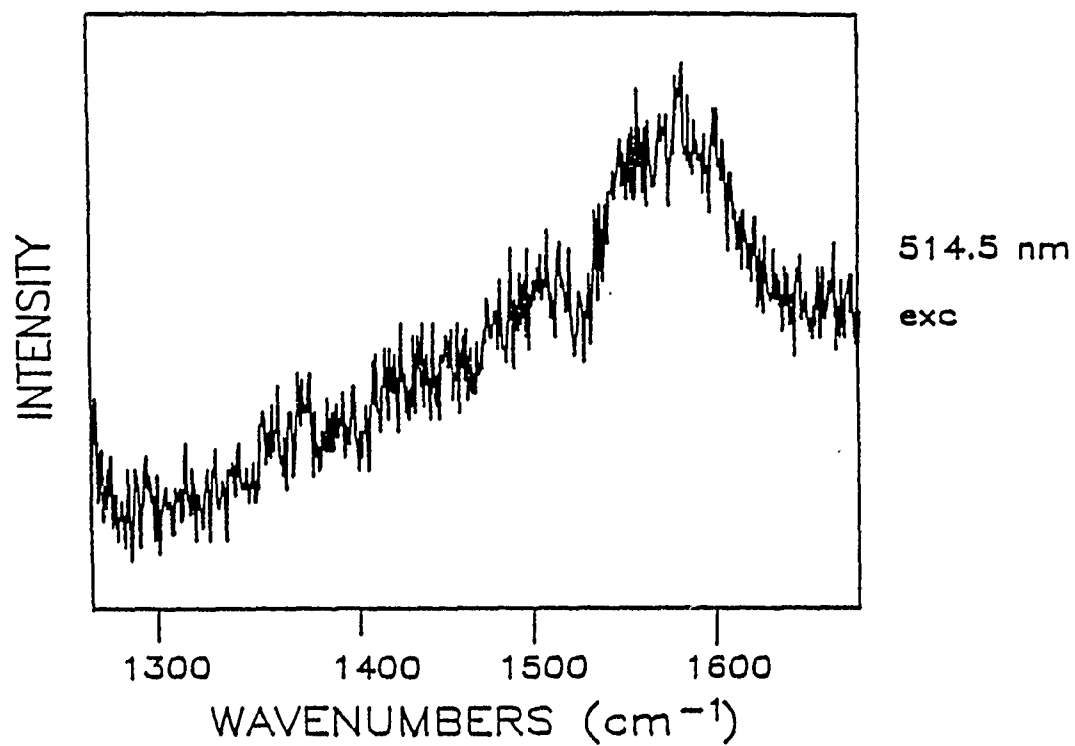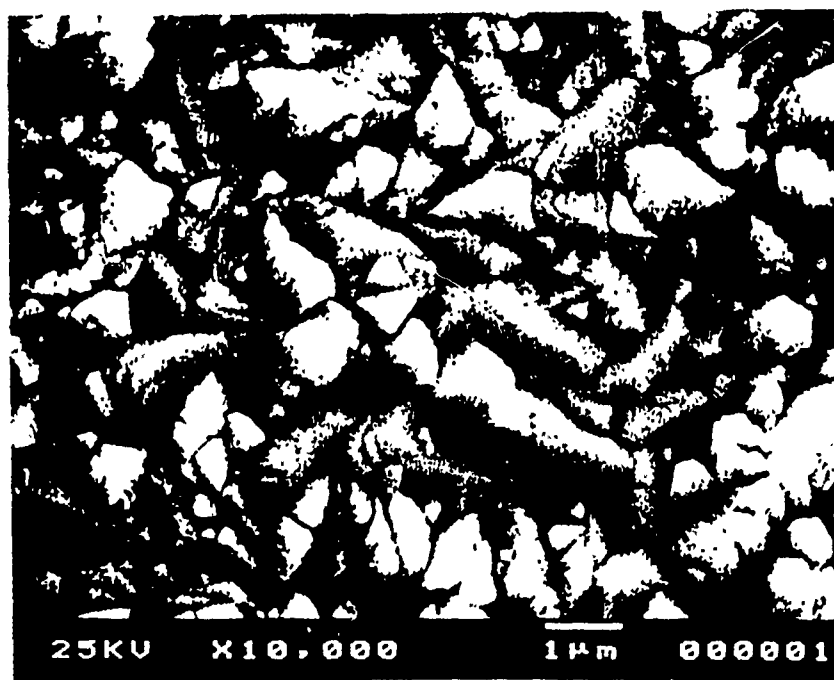Figure 1. *Micrograph and raman spectrum for sample 32E.*

Figure 2.   Micrograph and raman spectrum for sample 33H.

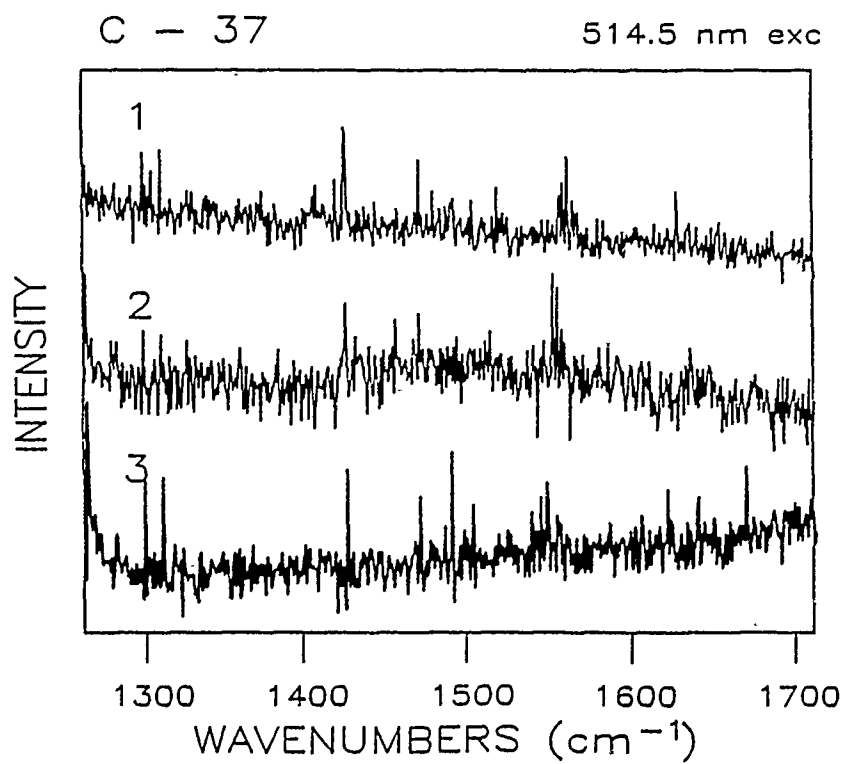C — 37   514.5 nm exc

Figure 3.   Micrograph and raman spectrum for sample 37C.

a capacitance manometer, maintains system pressure well above P_b, in the 10 to 100 torr range favored for diamond film deposition. The flange at the opposite end carries feedthroughs for electrical power, cooling water, thermocouple leads, reactant gases, and laser radiation. The system is capable of several types of substrate heating. Higher deposition temperatures and increased vapor activation promote increased reactivity.
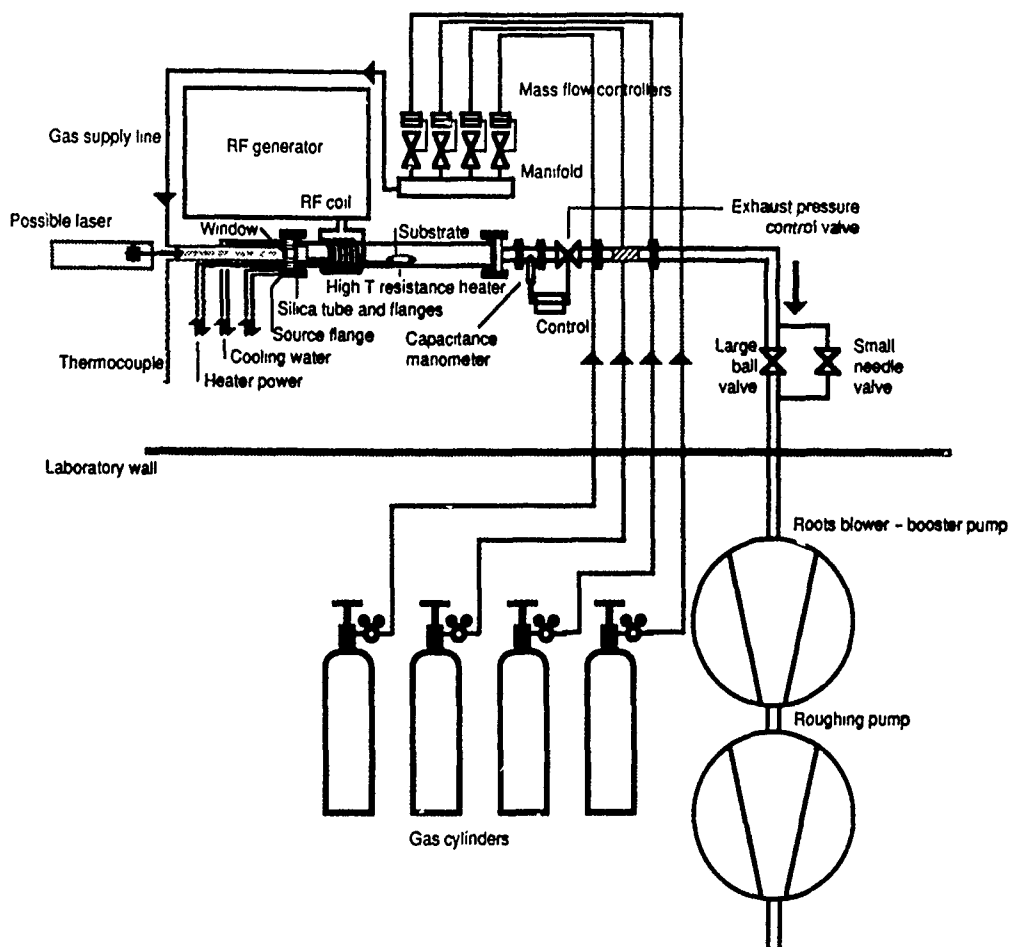

Figure 4. Multiply-assisted quartz tube CVD system.

By late March, the system was leak tested. We conducted several coating runs to test vacuum integrity, heater operation, and other parameters. The pressure in the tube was determined to be too low. To raise the system pressure, we installed a shunt line with a precision needle valve on the main vacuum line. By directing the flow through this small line, we could reduce the effective pumping speed and raise the process pressure. We controlled system pressure through a servo-controlled valve between the bypass and the process tube.

We began operating the system in April. Higher pressures were readily obtained, and higher deposition temperatures were obtained with use of the RF plasma. These two changes brought us much closer to conventional parameters for deposition of diamond films. For the first nine runs, a series of non-uniform, relatively dark films were obtained. Films from runs P-4, P-5, and P-7 yielded no Raman signatures. (See Figure 5 and Table 1.) Run P-8 yielded the most interesting film, with dark spots surrounded by brighter areas revealed by interference microscopy. The brighter areas resemble areas found in continuous diamond films. No Raman spectrum was obtained for this film.
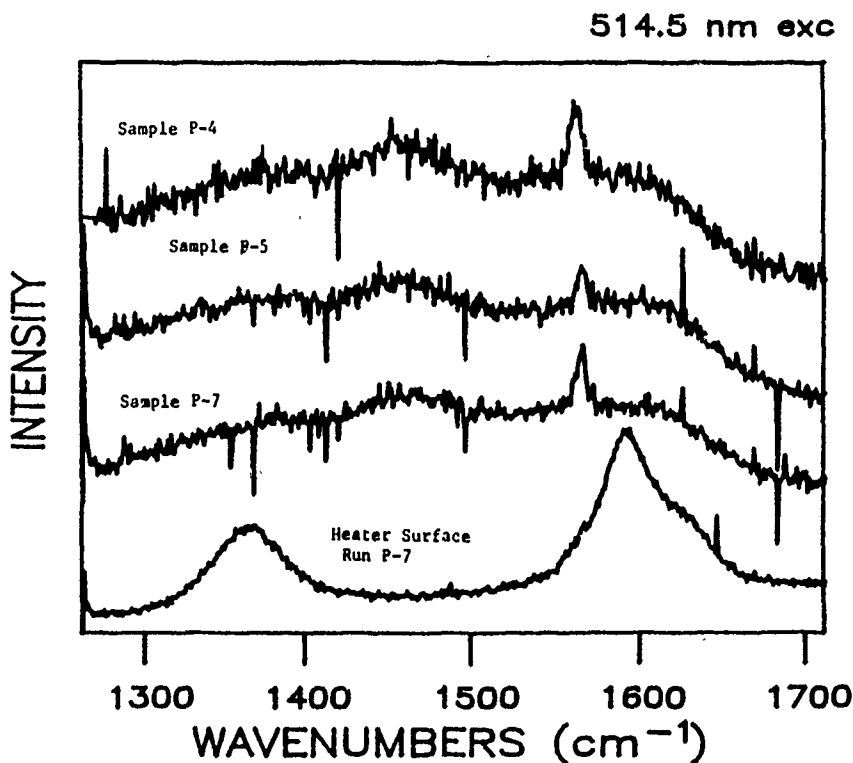
514.5 nm exc

Figure 5. *Raman spectra for samples P-4, P-5, and P-7.*

Our resources for conducting experiments with the new system were essentially exhausted by early May, and we abandoned all work at that time. Cameron Craigie continues his work on diamond as a Visiting Scientist at the Naval Research Lab in Washington, D.C. through fall 1990 under the supervision of Dr. Keith Snail.

Table 1. Coating runs for JSOP diamond project, 12/89 through 5/90.

CVD-1000 SYSTEM

#	Dates	Pressure mTorr	Temp.* °C	CH_4/H_2 SCCM	Filament AC V	Time min	COMMENTS
							* Actual temperatures are higher due to hot filament. CH_4/H_2 ratio = 0.5%
31	12/5/89	? 300	400	8	30	55	Rapid burnout of filament.
32	12/29/89	500	600-650	8	30	61	Filament close to touching substrate. These films looked the most like diamond. micrographs appear as Figure x and y. However, the Raman spectra showed nothing
33	1/3/90	300	650-815	8	30	96	Less crystalline appearance than previously. No Raman signature
34	2/12/90	>500	800-840	18	30	115	Thermocouple failures at first, repaired and retried that day
35	2/15/90	300	800-840	38	30	138	Rounder crystallikes. No Raman signature.
36	2/18/90	700	700-800	18	30	72	No Raman signature
37	2/20/90	500	740-840	18	30	110	No Raman signature.
38	2/24/90	700	760-780	38	30	45	Increase flow rate. No Raman signature.
39	2/28/90	700	720-812	38	30	95	No Raman signature.
40	3/3/90	700	730	38	30	18	No Raman signature.
41	3/3/90	500-700	732-750		30	-	Filament failed immediately
41A	3/5/90	>700	785-820	29	30	>240	Filament failure overnight
42	3/6/90	500-700	698-845	22	30	555	Longest run without filament failure
43	3/7/90	500		22	30	-	Immediate filament short
44	3/25/90			14			Failure due to closed outside valve.

HOMEBUILT QUARTZ SYSTEM

#	Dates	Pressure mTorr	Temp.* °C	CH_4/H_2 SCCM	Plate A	Time min	COMMENTS
							* Actual temperatures are higher due to hot filament. CH_4/H_2 ratio = 0.5%
P-1/P-2							Test runs
P-3	4/15/90	5,000	794-857	52	-	144	No diamond, black spots, 32 nm thick.
P-4	4/20/90	15,000	835-900	20	.47	280	No Raman signature.
P-5	4/23/90	15,000	800-913	20	46	285	No Raman signature
P-6	4/25/90	15,000	943-1000	20	?.46	230	Cover slip mask melted
P-7	4/30/90	17,000	37-900	20	.46	220	One substrate melted. No Raman signature for substrate or heater surface
P-8	5/3/90	15,000	780-900	20	46	740	Some crystals resembling those in continuous films
P-9	5/10/90	15,000	307-811	20	45	203	No diamond, plasma OK

Characterization

Characterization of the coatings was limited to

- spectrophotometry, performed in the Optical Sciences Center Optical Measurement Laboratory.
- scanning electron microscopy, performed in the OSC Characterization Facility.
- Raman spectroscopy, performed through the UA Chemistry Department in the laboratory of Prof. Jean Pemberton.

The SEM data were critical for observing the crystalline microstrucuture, and the Raman data were essential for a positive identification of diamond. The prohibitive costs of SEM and the frequent inaccessibility and inoperability of the Raman spectroscopy equipment made analysis difficult.

Summary

Results for fhe coating project are inconclusive. Efforts with the commercial CVD system were unsuccesful, as we were unable to modify it for use in diamond coating processes. Our resources allowed us to work less than a month with the quartz tube system design specifically for diamond coating processes. We hope to build on our experience with the quartz tube system to establish a diamond coating facility with other funding. In future efforts, we will be more careful to arrange for adequate characterization, in particular for Raman spectroscopy.

REFERENCES

1. A. Feldman and S. Holly, eds, *Diamond Optics*, Proc. SPIE 969, (1988).

2. A. Feldman and S. Holly, eds, *Diamond Optics II*, Proc. SPIE 1146, (1988).

3. *Diamond and Diamond-Like Materials Synthesis* (Materials Research Society, Reno, 1988).

4. Office of Naval Research, Annual Diamond Technology Initiative Symposia, Durham (1986), Arlington (1988).

5. B. V. Spitsyn, L. L. Bouilov, and B. V. Derjaguin, "Vapor growth of diamond on diamond and other surfaces," J. Cryst. Growth, 52, 219 (1981).

6. S. Matsumoto, Y. Sato, M. Tsutsumi, and N. Setaka, "Growth of diamond particles from methane-hydrogen gas," J. Mat. Sci 17, 3106-3112 (1982).

7. A. Feldman, "Diamond, a potentially new optical coating material," in *Laser Induced Damage in Optical Materials* (NIST, to be published, 1989).